Establishing optogenetic tools in the auditory system of the *Mongolian Gerbil*

Stefan Keplinger

Dissertation der Fakultät für Biologie

der Ludwig-Maximilians-Universität

München

Vorgelegt von Stefan Florian Keplinger

aus Linz, Österreich

München, den 17.02.2016

Diese Dissertation wurde angefertigt

unter der Leitung von *PD Dr. Lars Kunz*

im Bereich der *Systems Neurobiology*

an der Ludwig-Maximilians-Universität

Tag der Abgabe: 17.02.2016

Tag der mündlichen Prüfung: 18.07.2016

Erstgutachter: PD Dr. Lars Kunz

Zweitgutachter: Prof. Dr. Benedikt Grothe

"Figure out for yourself what you want to be really good at, know that you'll never really satisfy yourself that you've made it, and accept that that's okay."

Robert A. Heinlein

Abstract

The *Mongolian Gerbil* (*Meriones unguiculatus*) serves as a popular and widely used model organism for the human auditory system. Its hearing range largely overlaps with that of human's and even extends below 1 kHz, frequencies very important for human hearing. Like humans, gerbils can localize sounds based on their interaural time difference (ITD) or interaural level difference (ILD) and also show perceptual suppression of the spatial source of reverberations (precedence effect).

The auditory circuitries underlying the computation of ITDs and ILDs are very well described in the gerbil, although the exact mechanisms for the extraction of ITDs are still under debate. The contribution of the medial nucleus of the trapezoid body (*MNTB*) in tuning neurons sensitive to ITDs is still unclear.

Similarly, the precedence effect is well known and thought to greatly facilitate listening in reverberant environments, yet the neural substrate of the precedence effect is still elusive. A circuitry that might subserve the precedence effect is hypothesized to be formed by the dorsal nucleus of the lateral lemniscus (*DNLL*) and the inferior colliculus (*IC*).

However, a precise and reversible manipulation of the *DNLL-IC* circuitry or the ITD circuitry has not been possible due to the lack of technical means.

With the advent of optogenetics, tools are becoming available that would allow to specifically activate and silence nuclei within both circuitries. Yet, transgenic lines or genetic tools are neither disposable nor established for the *Mongolian Gerbil.* Hence, in order to express optogenetic tools in the *gerbil* auditory brainstem and midbrain, a reliable and neuron specific gene delivery system needs to be established as a major prerequisite. Only when this important first step is taken, the actual optogenetical tools can be applied and tested.

In this study, the first hurdle of gene delivery into the *Mongolian Gerbil* was successfully cleared by using recombinant adeno-associated viruses (r*AAV*) as vectors. Via the stereotactic injection of *rAAVs* into the *DNLL*, *IC* and *MNTB,* not only reliable and efficient transduction of neurons was achieved but also neuronal specific expression of transgenes was attained. As a second accomplishment, the channelrhodopsin mutant *CatCH* as well as the halorhodopsin *NpHR3.0* were characterized in acute brain slices by performing whole cell patch-clamp recordings of transduced neurons. As a final step and proof of principle experiment, sound evoked neural responses in the *DNLL* and *IC* were successfully manipulated with light *in vivo,* as could be demonstrated by single cell extracellular recordings from anaesthetized animals.

In sum, this study successfully adapted and established gene delivery and optogenetic tools in the auditory system of the *Mongolian Gerbil.* This represents a fully functional and highly versatile toolbox that not only paves the way to further elucidate the ITD as well as the *DNLL-IC* circuitry but is also applicable to other questions.

Table of Contents

1. Introduction

Sound is always present in any elastic medium above 0°K when there is any movement (Blackstock, 2000). For animals it represents a tremendous advantage for survival to detect movement, e.g. when escaping a predator. Then it is essential to reliably identify the direction of the sound (=sound localization), e.g. the prey escaping directly into the direction of the approaching predator makes usually its last error. Furthermore, the process of sound localization needs to be fast due to the fast modulations (in amplitude and frequency) of sound itself and the possible emergence of additional sound sources that might intermit or conflict with the original sound (Meffin and Grothe, 2009). As positive side effects another channel for interindividual communication is open and active spatial orientation in darkness is possible. However, a reliable sound localization is a demanding task because a multitude of sounds from various locations can be present at the same time. To isolate and focus on the relevant sounds filtering of the auditory cues is necessary. The circuitries in the mammalian auditory system underlying these filtering processes are still not completely understood.

1.1. Acoustical basis for auditory cues

In order to understand the sensory processing of sound, one has to understand the stimulus first. Our auditory system extracts information already present in the sound stimulus (e.g. notches) or derives information by comparing the sounds on the left and right ear.

In the following, the focus will lie on airborne sounds, whereas sound transmitted by solid (e.g. bone conduction) or liquid media (e.g. water) will not be discussed in detail for the sake of brevity. Airborne sound is generated by displacement of gas particles. Neighboring gas particles exert push- and pull forces on each other and thereby spreading the displacement usually in a spherical manner with 343m/s at 20°C. Several dimensions exist to describe sound in the form of a mechanical wave (Figure 1A). The level of displacement from the equilibrium (=atmospheric pressure) is called amplitude and due to the push- and pull forces can be described and measured as pressure in *Pascal* (1 *Pa*=1N/m^2). In reference to human absolute hearing thresholds, sound amplitude is usually measured on a logarithmic scale in sound pressure level (*SPL*) *SPL dB* ($1 dB\ SPL = 20 * \log\left(\frac{22.44 \mu Pa}{p0}\right)$). For historical reasons 20µPa at 1kHz =p_0 was determined as 0 dB SPL, which actually is slightly lower than the human hear threshold (Suzuki and Takeshima, 2004). The duration of a positive and negative displacement around the equilibrium is called period and measured in (milli)seconds. The number of periods per second is called frequency and is measured in *Hertz* (1*Hz*=1 period/second). The acoustical phase describes the
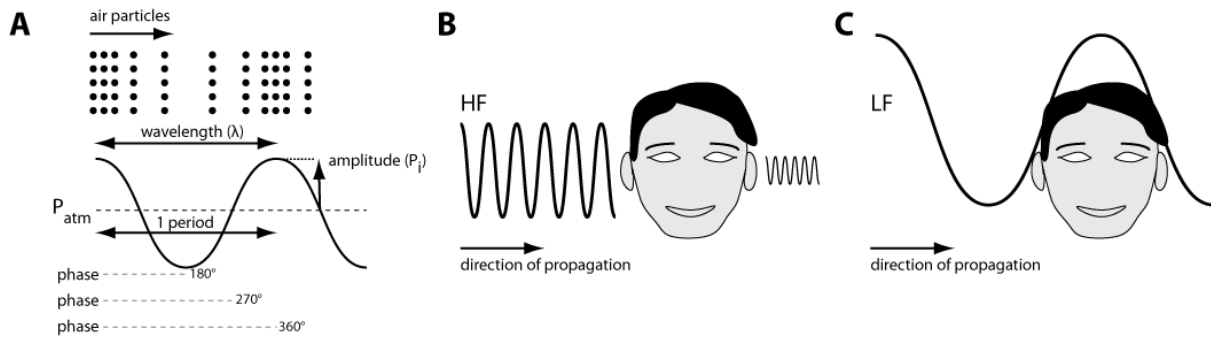
Figure 1: Physical definitions and characteristics of airborne sound

A. Sound can be understood as pressure wave exerted by air particles that are compressed and most dense at the pressure maximum and decompressed and most spread at the pressure minimum. Black dots represent the allocation of air particles during a pressure wave i.e. sound. The definitions to describe a sound wave are amplitude of the pressure wave (p_i), the wavelength (λ) describing the length of the wave from peak to peak, the period describing the duration of the wave from peak to peak and the phase of the wave describing the position on the wave. P_{atm} indicates the atmospheric pressure as the pressure baseline or equilibrium. **B**. A cylindrical sound wave of high frequency (HF) with a small wavelength relative to the head will be reflected and only partly transmitted through the head. Therefore only a fraction of the original sound amplitude is reaching the distant ear. **C**. A cylindrical low frequency (LF) sound wave with half its wavelength bigger than the head is not attenuated. The only difference is the earlier arrival time or earlier phase of the sound at the closer ear compared to the distant ear.

position on the sound wave in degree (360°=1 period, 180°=0.5 period, etc.). Since sound propagates at 343m/s in air, the dimension used to describe the length of a single period is called wavelength (λ) and measured in *Meter (m).* The range of frequencies in a sound is called the spectrum and is also described in *Hz*.

The characteristics of sound, which are relevant to hearing can all be described by these dimensions or parameters. By interaction of the sound wave with the environmental world one or more dimensions are changed. Diffraction, reflection and absorption are the most frequent processes which change the characteristics of a sound. Reflection of a sound happens when the acoustical obstacle is at least within the physical size of half the sound's wavelength and has a high acoustical impedance. The acoustical impedance can be understood as the resistance to sound transmission. A high difference in acoustic impedance between two media causes reflection of a sound at the interphase between the media. The reflected air particles loose kinetic energy on impact thereby decreasing sound amplitude. Sound is reflected according to the law of reflection. If the acoustic obstacle has a low acoustic impedance sounds can be transmitted or completely absorbed by the obstacle. As a matter of fact as the wavelengths for high frequencies get shorter, the number of obstacles that are in effective range to reflect, transmit or absorb sound increases (Figure 1B). Sounds with half the wavelengths bigger than the physical size of an obstacle are neither affected by reflection nor by absorption (Figure 1C). These acoustic principles already allow for three important observations:

1. High frequencies with half the wavelengths shorter than interaural axis (e.g. >857Hz for 20cm head width; (see (Algazi et al., 2001; Blauert, 1997b) for detailed data) will start to be more and more diffracted, reflected and partial absorbed by the head. This results in attenuation of the sound amplitude between the ear facing the sound source and the distant ear in a frequency dependent manner (Thompson, 1882). This disparity is called interaural level difference (ILD) or interaural intensity difference (IID).

2. Frequencies with half the wavelengths longer than the interaural axis (<857Hz for 20cm head width) are not diffracted and simply pass the head without any attenuation. The only disparity that arises by comparing the sound at the ears are the different arrival times. The sound impinges first on the ear facing the sound source and second at the distant ear. This is also applies for higher frequencies though. The difference in arrival times is called interaural time difference (ITD) or a similar used expression accounting for the frequency is interaural phase difference (IPD (cycle)=frequency*ITD).

3. Sound can be reflected and reach the ears indirectly. The sum of all sound reflections are called reverberations. Especially for point sources which emit sounds in all directions the number of the reflections from the environment is highest. When reflected from high impedance obstacles sound is spectrally equal to the direct sound. Additionally, reverberations can even surpass the direct sound in amplitude, because sound amplitude decays with distance from the source (approx. ~1/distance (r)) and reflections sum up. The distance where both the amplitudes of the direct sound and of the reverberations, are equal is called the critical distance (Sabine, 1922), beyond the critical distance reverberations are louder. Thus frequency content and sound amplitude are an ambiguous cue for sound localization in reverberant environments. Yet, within and beyond the critical distance the arrival times at the ears between direct sound and its reverberations are different at all distances. These temporal disparities can be exploited for sound localization of the direct sound.

The first two fundamental observations were combined more than 100 years ago and led to the formulation of the famous *Duplex theory* by Lord Rayleigh (Rayleigh, 1907). Therein a corner frequency between the two cues (ITD or ILD) of ~1.5kHz for dominating the localization percept in human listeners was established. Both binaural cues are relevant for determining the position of sound sources in the horizontal plane. For the elevation of sound sources mammals can rely on monaural cues. Impinging sound is diffracted by the body, head and pinna which cause notches (e.g. "pinna notch" at ~10kHz for human) at certain frequencies depending on the elevation of the sound source. These spectral changes are the so called head-related transfer functions (HRTFs). If these monaural cues are not implicit

enough e.g. human listeners can simply tilt their head to vertically align the interaural axis accordingly and use binaural cues.

1.1.1. Interaural level differences (ILDs)

As mentioned in the chapter above sound level differences between the ears can be used to infer the position of a sound source. The ILD cue is usually dominant for localizing higher frequencies, except in the near field where ILDs can also be used for low frequencies (Shinn-Cunningham et al., 2000). Sounds from distances within 1m (=near field for humans) generate high ILDs also for low frequencies due to the head's shadowing effect, whereas ITDs hardly change (Brungart and Rabinowitz, 1999). The range of possible ILDs is limited by the extent of the head's shadowing effect. The head's shadowing effect depends on its size and shape relative to the sound's wavelength (Harper et al., 2014). Smaller heads attenuate higher frequencies and bigger heads attenuated already lower frequencies (Grothe et al., 2010; Sabin et al., 2005). For a human head, ILDs start around 857 Hz and become more pronounced with increasing frequency (Figure 2A). The amount of frequency dependent sound level attenuation by the head is systematically explored by measuring HRTFs for an array of directions and frequencies and is available from databases (Algazi et al., 2001) and for many species (Maki and Furukawa, 2005a; Sterbing et al., 2002; Young et al., 1996) . Another limit for the upper range of possibly perceived ILDs is the frequency sensitivity of the hearing system. Higher
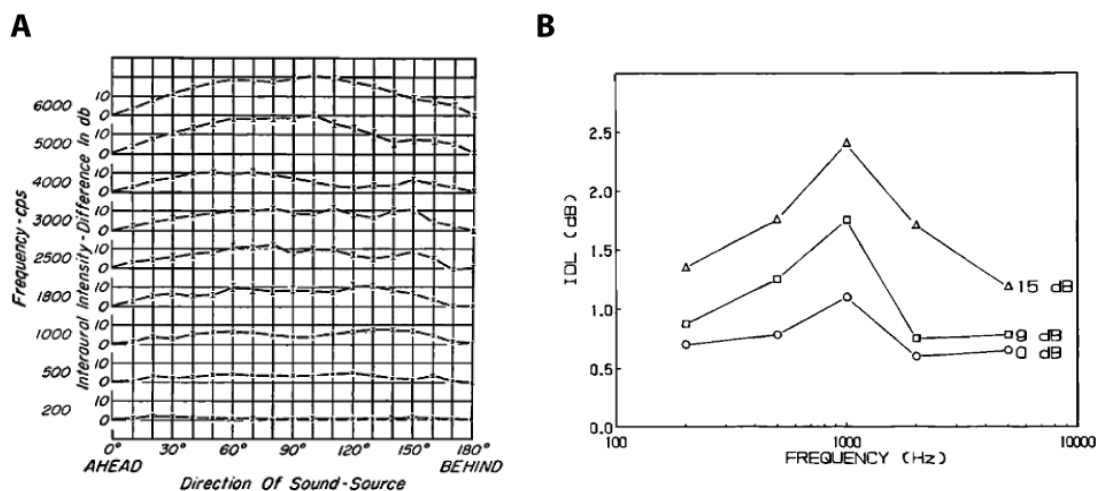
Figure 2: ILDs increase with frequency and ILD thresholds are similar to level JNDs.

A. Measured values of ILDs plotted against azimuth angle for tones from 200-6000 Hz. The ILDs increase with frequency and are highest at 90°. Adapted from Feddersen et al., 1957. **B.** Average thresholds of ILDs over frequency for three human listeners. Highest sensitivity for changes at the midline (=0 ILD). Adapted from Yost et al., 1987. (All figures were adapted with permission).

frequencies might be attenuated more resulting in a higher ILDs between the ears (Feddersen et al., 1957), yet if the cochlea is not sensitive to these frequencies the ILDs cannot be extracted. Hence, an animal's lower border of the ILD range is given by its head size and just noticeable difference (JND) thresholds in amplitude (Mills, 1960), around 1-0.5dB, and the upper border of the ILD range is given by highest possible perceived frequency. For instance, from psychophysical experiments with human listeners it is known that the degree of acuity to distinguish also small ILDs stays nearly constant with sound frequency >1kHz (Yost and Dye, 1988) and matches the overall sensitivity for sound amplitude changes per se, which is a threshold of 0.5-1dB SPL (Grantham, 1995; Grothe et al., 2010; Mills, 1960) (Figure 2B).

In sound localization tasks using ILD cues human listeners tend to bias more lateral sound positions towards their anterior midline but get better in localizing and make lesser errors at their auditory midline (Carlile et al., 1999; Carlile et al., 1997). Interestingly, human listeners can also increase their sensitivity for ILDs of a certain position or adapt to higher varieties of perceived ILDs (Dahmen et al., 2010; Dean et al., 2005; Phillips and Hall, 2005). This ability to adapt the ILD sensitivity to a certain position is of great benefit e.g. in order to ease attendance to a speaker in the noisy environment of a party, a phenomenon hence termed "cocktail party effect" (Hawley et al., 2004).

1.1.2. Interaural time differences (ITDs)
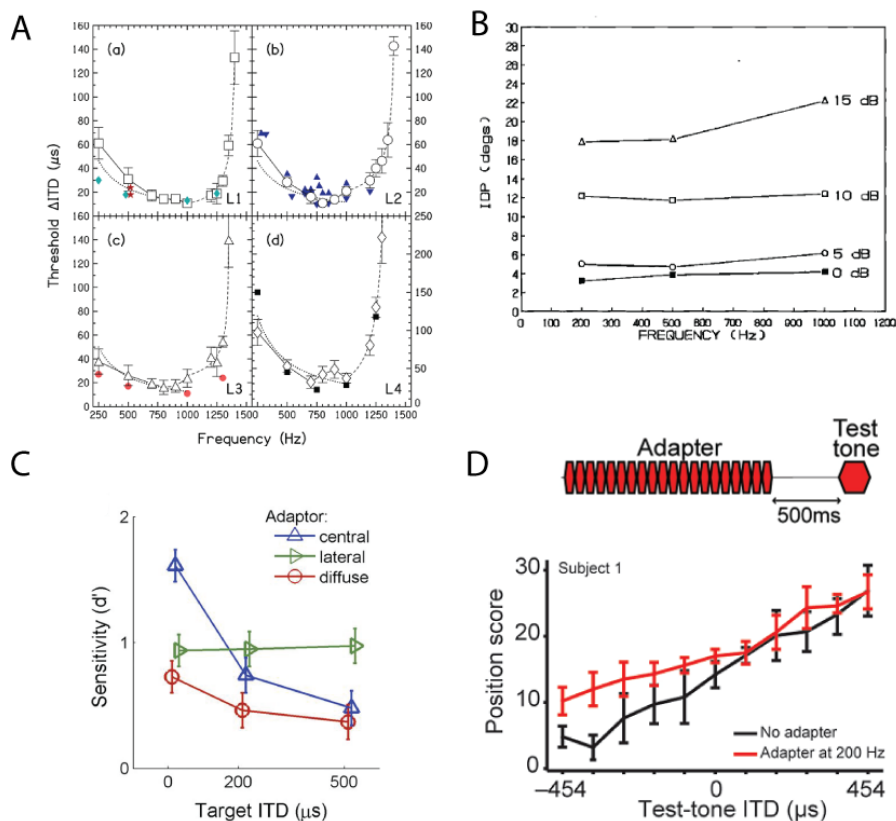
Figure 3: ITD sensitivity is highest at the midline and declines with frequency.

A. Frequency dependence of individual ITD thresholds from four subjects (a-d). Performance deteriorates quickly above 1.2kHz and is highest at 850-1000Hz. Adapted from Brughera et al., 2013. **B**. Shown is the average IPD thresholds from 2 listeners. Three frequencies were tested and 4 different ILDs (0, 5, 10, 15 dB SPL) were superimposed on the IPDs. Listeners are most sensitive for IPDs at the acoustical ILD midline (=0dB SPL). Adapted from Yost et al., 1988. **C.** With training ITD sensitivity can be increased for the adapted azimuth. Human listeners were presented with three different noise adapter ITDs for central, lateral or diffuse azimuth. Sensitivity (d') for target ITDs was increased when adapter and target ITD were around the same position. Adapted from Maier et al., 2012 **D**. The ITD sensitivity can be increased around an 200Hz adapter at -625µs ITD. This shift in sensitivity is reflected in the overestimation of ITDs or azimuth near the adapter by human listeners. Adapted from Stange et al., 2013. (All figures were adapted with permission).

According to the Duplex theory, ITD cues are used for frequencies below 1.5kHz. This holds true for the fine structure of sound but ITD cues can still be used for higher frequencies because time-locking occurs also to the sound envelope at higher sound frequencies. Thereby the sound envelope timings are preserved and ITDs can be extracted (Griffin et al., 2005; Yost et al., 1971). Similar to ILDs the possible range of ITDs is also a physical dependence on the size of the head but for the upper border (there are exceptions though where ITDs can be longer e.g. for reflected sounds or artificially generated with headphones, etc.). The lower border of ITDs can in principle be indefinitely short. The longest possible "natural" ITD is given by the interaural distance, around 600-750µs, (van der Heijden and Trahiotis, 1999) and the lowest perceived ITDs (Brughera et al., 2013; Klumpp and Eady, 1956;

McFadden and Pasanen, 1976) can be around 10µs in human listeners (Figure 3A). The head size poses a restraint for the range of ITDs in small animals (e.g. for the *Mongolian Gerbil* a maximum of 50µs for its 2cm interaural axis is possible to code for ITDs). ITDs are the dominating cue for localizing low frequency sounds when conflicted with ILDs (Wightman and Kistler, 1992). The acuity for ITD changes is mediocre for very lateral positions (=longer ITDs) and highest at the anterior midline (=0µs ITD) where the JNDs are smallest and the sensitivity highest (Domnitz and Colburn, 1977; Maier et al., 2012; Yost and Dye, 1988) (Figure 3B). Interestingly, sensitivity for a certain ITD (=target) can be increased when listeners are trained with a sound (=adapter) having an ITD close to the target ITD before (Maier et al., 2012) (Figure 3C). The target sound and the adapter sound also have to be spectrally similar otherwise this sensitivity increase does not affect the target sound (Figure 3D) (Stange et al., 2013). This adaption in sensitivity to a certain ITD or certain position also might subserve listening to a single speaker in a multi-speaker environment, e.g. like observed with the cocktail party effect (Hawley et al., 2004).

The ITD sensitivity as JNDs for human listeners also varies with frequency (Brughera et al., 2013). Yet interaural time differences do not depend on frequency, since sound of any frequency is delayed by the interaural axis to the distant ear. Therefore, ITDs are independent of frequency and explicit. This in contrast to interaural phase differences (IPD), which can be ambiguous at more than 180° phase difference. Also IPDs for a sound source at a defined angle would vary a lot with frequency but the according ITD would stay constant. From a psychophysical perspective the performance in localization tasks for IPDs in human listeners therefore should be high for frequencies below <850Hz, best around 850Hz (sound wave has 180° phase difference between the ears) and then deteriorate due to the phase ambiguity of higher frequencies. In listening tasks any prevalence of ITD vs. IPD could neither be completely confirmed nor completely disproved (Dolan et al., 1981; Yost and Hafter, 1987; Zhang and Hartmann, 2006). Whatever the better representative of the physiological signal is, a requirement for extraction is that the fine structure of the sound is preserved with high fidelity.

1.1.3. First wave front, reverberations and precedence
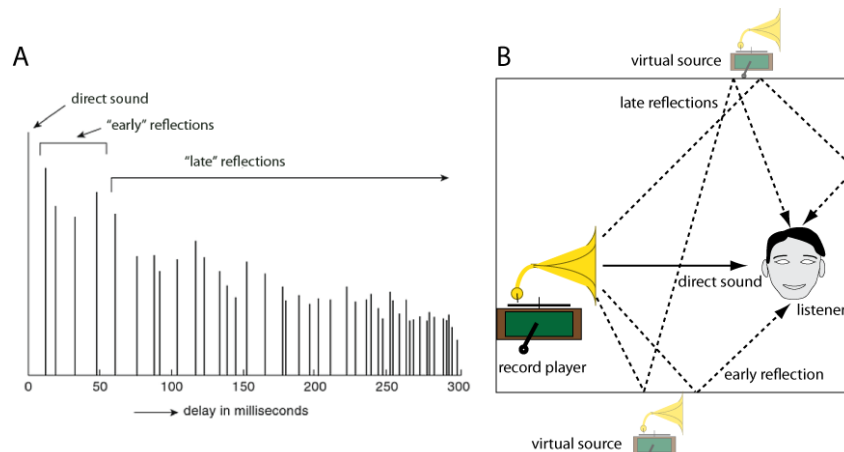
Figure 4: Reflections are numerous and categorized by their time of arrival

A. Typical impulse response of a room. The time and amplitude of reflections relative to the direct sound are displayed. A single reflection is lower in amplitude but the integral of early and late reflections (=reverberations) can be higher in amplitude than the direct sound. Adapted from Kuttruff H., Room Acoustics. 2000 (with permission). **B**. Distracting acoustical environment in an echoic room when listening to a record player. Reflections arriving after the echo threshold can be localized and be perceived as virtual sound sources, e.g. at the ceiling or floor. These virtual sound sources are conflicting with the actual sound source.

In contrast to ILDs and ITDs mentioned above, the extent of reverberations is not influenced by the head but depends on the environment. Usually the extent of reflections is greatest indoors, where floor, walls and ceiling are high impedance obstacles and therefore reflective for sound. On one hand room acoustics have some specialties in comparison to the free field - e.g. also for low frequency sounds ILDs can be experienced (Blauert, 1997a) - on the other hand the same principles as in the free field apply. Reverberations are commonly categorized into early (<80ms after the original sound) and late reflections (>80ms) depending on their delay relative to the direct sound (Kuttruff, 2009) (Figure 4A). Single late reflections can be perceived as separate sounds and can also be localized separately (according to their ILD and ITD). These are called echoes and can perturb speech intelligibility and attendance greatly (Bradley et al., 2003; Shinn-Cunningham et al., 2005). When echoes are perceived, they can act as time delayed virtual sound sources, eventually intermitting and distracting the perception of the direct sound (Figure 4B). The time delay relative to the direct sound necessary for a reflection to be perceived as a second sound event is called echo threshold and is therefore a subjective measure that can be tested individually in listening tasks. Commonly, listeners are presented with a leading (=direct sound) and lagging sound (=reflections) with varying delay. The lead-lag delay, where mostly two sounds are perceived instead of only one is determined as the individual's echo threshold. At delays shorter than the echo threshold only a single, fused sound event is perceived. This perceptual illusion is therefore called *fusion*. With longer lead-lag delays this illusion disappears and two

separate sounds are perceived (Freyman et al., 1991). Echo thresholds are not static but can "build up" and depend on listeners' expectations and experience - i.e. the listeners can learn the acoustics of a room, etc. (Clifton et al., 1994) - the spatial separation of the sound source and its reflection in the horizontal plane (Dent et al., 2009) and the complexity of the sound (for review see (Blauert, 1997a; Litovsky et al., 1999) and (Litovsky et al., 2010)). From these data it follows that also early reflections can be perceived as separate sounds since the echo thresholds for simple sounds can be as low as <3-5ms (=the usual delay for early reflections from the floor and ceiling in a normal room). When studied in paradigms of leading and lagging sounds with delays shorter than the echo thresholds, listeners started to localize the sound source slightly towards the lagging sound. This perceptual phenomenon is called *localization dominance,* since the leading sound dominates the localization percept (Zurek, 1980). For very short lead-lag delays (<1ms) or when both sounds were coincident, the source was even perceived as coming from the middle position between the two. This effect is called *summing localization* and is exploited in sound engineering for stereophony to create virtual or "phantom" sound sources (Blauert, 1997a).

However, reflections pose a challenge for the listener because they can exist as a multitude of copies of the direct sound, can outlast direct sound, be louder and are conflicting with the position of the original sound source. In fact this "sensory rivalry" (Hafter and Buell, 1990) is solved by employing a temporal gating mechanism by weighing only the spatial localization of the first wave front (=direct sound). This behavior is known as the "law of the first wave front" or precedence and when in effect, results in the correct localization of a sound source in reverberant environment. It was first observed by Cremer L. (Cremer, 1948) and subsequently described by Wallach H. et al. (Wallach et al., 1949). In their studies, human listeners could determine the location of a sound source in the presence of reflections or lagging sounds with the very same spectral content. The precedence effect was also observed by Haas (Haas, 1951) in respect to speech intelligibility, reporting that early reflections were actually helpful for understanding a speaker because they could increase the amplitude of the direct sound. Late reflections in contrast had a very distracting influence on speech intelligibility. Under certain conditions the precedence effect also ceases to work, e.g. if the spectral content of the leading and lagging sounds differs or if leading and lagging speaker are simply switched (Clifton, 1987). Then precedence "breaks down" and after a few seconds precedence builds up again under these new conditions (*Clifton* effect). Yet the term "break down" is actually not correct, since switching leading and lagging speaker again and thereby reinstating the original listening condition also reinstates the precedence effect without the need for another "build-up" period. A popular acoustical illusion exploiting precedence (i.a.) in listeners is the *Franssen effect* (Hartmann and Rakerd, 1989). In short, listeners are sitting outside the critical distance and are presented tones over a leading and lagging loudspeaker. The tones over the lagging loudspeaker are not only delayed but the lagging speaker is actually

silent in the beginning. Slowly the amplitude on the lagging speaker is increased to provide no onset of the sound. In parallel the amplitude of the leading speaker is successively lowered. When the leading speaker is already completely silent and the tones only played over the lagging speaker, listeners don't notice that the tones are now only coming from the lagging speaker. Instead listeners will always localize the tones to the leading but now silent speaker.

1.2. Neural basis for sound localization in mammals

1.2.1. Sound transduction: from the outer ear to the *Organ of Corti*
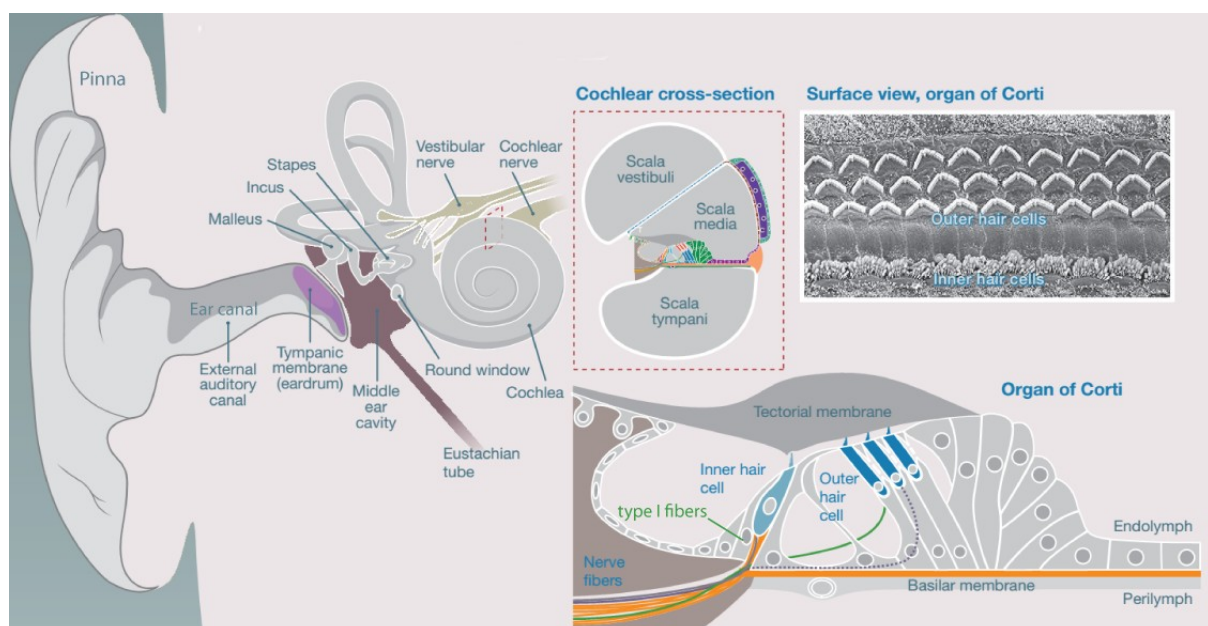
Figure 5: The three stations in sound transduction - the outer, middle and inner ear.

The outer ear: sound impinges first on the *pinna* and ear canal, depicted on the left.

The middle ear: the sound moves the *tympanic membrane* (violet), the entrance to the middle ear with. The three ossicles - *malleus*, *incus* and *stapes* - transfer the vibrations of the tympanic membrane to the *cochlea*.

The inner ear: the pressure wave passes through *scala vestibuli* and *tympani* and exits the *cochlea* via the round window. The pressure difference between these both scalae elicit a displacement traveling wave in the basiliar membrane (orange) starting at the base of the *cochlea*. The *Organ of Corti* sits on top of the basiliar membrane in the scala media and is the place of sound transduction. Outer hair cells (OHC in dark blue) amplify the displacement of the basiliar membrane. The inner hair cells (IHC in light blue) are the mechanotransducers and translate the displacement of the basiliar membrane into receptor potentials. Note, that unlike depicted here, there is no evidence that IHCs are connected to the tectorial membrane. Adapted from Hudspeth, 2013 (with permission).

The conversion of a sound stimulus into a change in membrane potential of an inner hair cell is called sound transduction. The inner hair cells are the actual sensitive receivers for sound and the place of sound transduction. The inner hair cells are part

of the *Organ of Corti*, which resides within the fluid filled *cochlea*, a bony and spiral shaped structure in the inner ear (Figure 5). Thus, any sound must first be transmitted through this fluid (perilymph) in order to stimulate the inner hair cells. Normally, when airborne sound impinges on a fluid surface, the sound is reflected because fluids have a high acoustical impedance. Only by virtue of the outer and middle ear, the sound is matched to the impedance of the endo- and perilymph in the *cochlea*. The outer ear consists of the prominent *pinna*, which funnels the sound waves into the ear canal, the ear canal itself and the attached muscles. More specific, the geometry of the *pinna* and ear canal act as an quarter wave resonator or impedance transformer similar to a pipe organ with one closed end (=tympanum) (Hudspeth, 1989; Stinson and Lawton, 1989). Sound waves with a wavelength $<\frac{1}{4}$ of the ear canal's length (~25-30mm in humans) and its harmonics are reflected at the open end of the ear canal causing standing waves. These resonances sum with the impinging sound producing the same frequency but with 90° phase shift and higher amplitude at affected frequencies. The amplitude gain for these frequencies (centered at ~3.4 kHz) is in the range of +20dB SPL (Wiener and Ross, 1946) and represents one reason for the highest sound amplitude sensitivity in the range from 2-5kHz in human listeners (Robinson and Dadson, 1956). The outer ear ends at the *tympanum*, which is the beginning of the middle ear.

The middle ear is comprised of the *tympanum*, the three ossicles - the *malleus* attached to the *tympanum*, the *incus* and the *stapes* - inside the *tympanic cavity*. For pressure equalization *the tympanic cavity* is connected via the *eustachian tube* to the nasal cavity. Sound passing through the ear canal displaces the *tympanum* causing it to vibrate according to sound frequency. The vibrating *tympanic* membrane in turn transmits these vibrations onto the three ossicles, that act like an acoustic lever with a frequency depended pressure amplitude gain, transforming the pressure from the large *tympanum* onto the 14fold smaller oval window. The amplitude gain by the acoustical lever is called middle-ear pressure gain and in humans is highest between 1 (+23.5dB SPL) and 3 kHz (Aibara et al., 2001) and another reason for the highest sound amplitude sensitivity in that range in human listeners.

The oval window is the membranous entry to the inner ear. The inner ear resides in the otic capsule and comprises the *semicircular canals*, the *cochlea* and the *vestibule*. The *stapes* transmits the vibrations onto the oval window, a fenestration in the *vestibule* and the base of the *scala vestibuli*. The *scala vestibuli* is one of three fluid filled, spiral shaped ducts in the cochlea. It passes into the *scala tympani* at *helicotrema*, the apex of the *cochlea*. The *scala tympani* terminates at the round window, the second membranous fenestration in the *vestibule*. Due to the elastic membranes sealing both windows, the pressure wave that entered through the oval window can escape the *cochlea* through the round window. Yet, the actual functionality of the *cochlea* lies in the third duct in the middle between the *scala vestibuli* and *tympani*, the *scala media*. The *scala media* is filled with potassium rich endolymph and separated by the *Reissner's membrane* from the *scala vestibuli* and

by the *basiliar membrane* from the *scala tympani*. The basiliar membrane is elastic, most stiff and thinnest at the base and widest and most loose at the apex. Therefore vibrations from the oval window cause nearly instant pressure differences between *scalae vestibuli* and *tympani*, which in turn cause a slow traveling wave starting at the base and displacing the basiliar membrane maximally at its according eigenmodes of high frequency at the base and low frequency at the apex (Von Békésy and Wever, 1960). This arrangement or topography of eigenmodes along the basiliar membrane is the basis for the so called tonotopy, the transformation of a sound into its fundamental frequencies according to the position on the basiliar membrane. Another consequence of this tonotopy is that high frequencies are stimulated earlier due to their position near the cochlea base, whereas the displacing traveling wave reaches the lower frequencies at the apex later (Kimberley et al., 1993). This delay between high and low frequencies is called cochlea traveling wave delay. The tonotopic arrangement also results in fuzziness for frequency separation: when two tones are close enough together, they cannot be distinguished anymore. This is defined as the "critical band" and is due to the finite sharpness of the deflection, i.e. the deflection is spread on the basiliar membrane.

The *organ of corti* resides right on top of the basiliar membrane and consists of three parallel rows of *outer hair cells* (*OHC*), one row of *inner hair cells* (*IHC*) and their supporting cells. Both hair cell types have stereocilia at their apical side. The longest stereocilium of the *OHC* is connected to the *tectorial membrane*. The ~12,000 *OHCs* (in humans) act as non-linear mechanical amplifiers (up to a gain of +40dB SPL for small sound amplitudes) through enhancing the displacement of the basiliar membrane. They do this by active deflection of their stereocilia with the help of myosin-1c and elongation of their cell bodies via their cytoskeletal *prestin*. The active amplification by OHCs can work up to frequencies of 100kHz in some mammals, though it is not known which molecular motors are capable of sustaining such quick movements. Only *OHCs* at the site of the basiliar membrane's stimulated eigenmode get active.

The stereocilia of the ~4500 IHCs are an essential part of the actual mechano-transducers. Shearing forces due to basiliar membrane oscillations lead to deflection of the stereocilia. It is thought, that deflection into the direction of the longest stereocilium causes attached tip links to pull open non-specific cation channels. The mechanical opening of the still unknown non-specific cation channels (Kwan et al., 2006) is followed by mechanical closing when stereocilia move in the opposite direction which causes hyperpolarization. Due to the high potassium concentration in the endolymph and therefore high electrochemical gradient, channel opening (<50µs) (Fettiplace and Kim, 2014) causes rapid influx of potassium (and also other cations) and within milliseconds a receptor potential causes voltage gated calcium channels to open. Subsequent calcium influx leads to the release of glutamate at the basal side, a synaptic structure specialized for fast and precise transmission by graded receptor potentials, called ribbon synapse (Glowatzki et al., 2008; Moser et

al., 2006). The myelinated afferents, called type I auditory nerve fibres (*ANF*), connect 1:1 with *IHCs*, but single *IHCs* are innervated multiple times by the afferents. Since only one *IHC* is innervated by one *ANF* fibre, frequency channels cannot mix and the tonotopy is further maintained on the level of the *ANF*. Cell somata of the *ANF* are embedded in the cochlea and comprise the spiral ganglion. The *ANF* projects from the *IHCs* to the *cochlear nucleus* (*CN*). The type I auditory nerve fibres convert the sound stimulus into action potentials (AP) by firing only at a certain phase of the sound stimulus up to a frequency of 3.5 kHz in cats (the upper limit is species dependent) (Johnson, 1980). This phenomenon is called "phase locking". This specialization preserves the temporal information also for postsynaptic stations e.g. for extraction of ITDs even for pure tones. The sound amplitude is rate coded and amplitude modulations are coded by time locking to the modulation frequency in the sound envelope (Joris et al., 2004). As pointed out, the upper limit for phase locking is to some degree species dependent (e.g. 3.5kHz upper limit in the guniea pig and even higher in cat) and determined by the IHCs, that act as a low pass filter and half wave rectifier (Palmer and Russell, 1986) .

1.2.2. The neural circuits for the computation of ILDs and ITDs
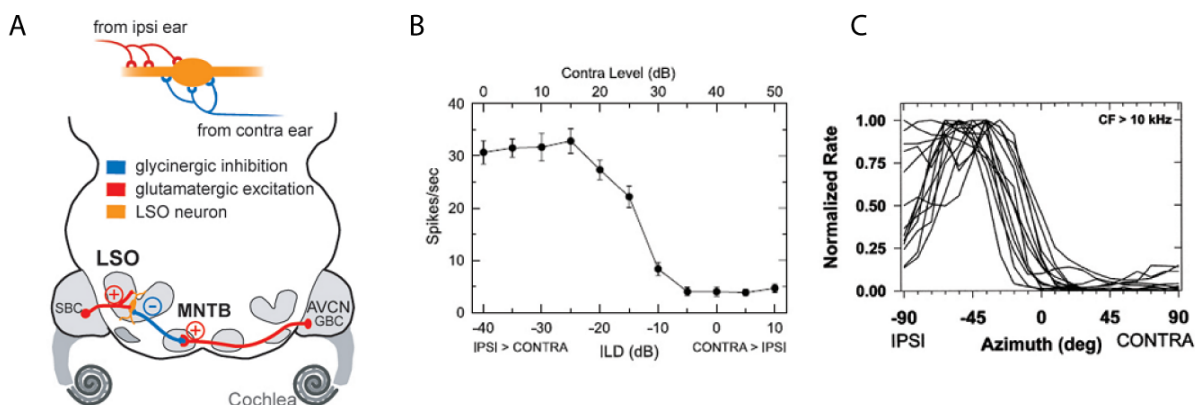
Figure 6: The LSO circuitry and ILD functions

A. A LSO neuron gets excitatory (red) input from the ipsilateral ear and inhibitory input (blue) from the contralateral ear. The LSO circuit is depicted underneath: SBCs from the AVCN provide glutamatergic input to the ipsilateral LSO. From the contralateral AVCN, GBCs project to the ipsilateral *MNTB*, where a sign conversion happens and excitation input is turned into inhibitory output to the LSO. Thereby the LSO gets inhibition from the contralateral ear. **B**. A typical ILD function of a LSO neuron, with increasing spike rates for higher ipsilateral sound amplitude and lower spike rates for higher contralateral sound amplitude. **C**. Pooled HRTF functions from several LSO neurons in the cat. Most LSO neurons have their highest dynamic range at the midline. Adapted from Grothe and Pecka, 2014 (with permission).

Spherical bushy cells (*SBC*) in the *anteroventral cochlear nucleus* (*AVCN*) receive excitation from the auditory nerve through one to four endbulbs of Held (Xu-

Friedman and Regehr, 2005) but also get inhibitory input in order to sharpen their temporal, spectral and sound amplitude related response (Kopp-Scheinpflug et al., 2002). *SBCs* ipsilaterally synapse onto *lateral superior olive* (*LSO*) and the *medial superior olive* (*MSO*) but its axons also cross the midline to innervate the contralateral *MSO* to provide glutamatergic excitation. *Globular bushy cells* (*GBC*) integrate excitation from five to ~40 inputs from the auditory nerve (Spirou et al., 2005), thereby lowering jitter and preserving temporal precision. Their axons project ipsilaterally onto the lateral nucleus of the trapezoid body (*LNTB*) and contralaterally to the medial nucleus of the trapezoid body (*MNTB*). These axons exhibit large diameters, thick myelin sheaths (Ford et al., 2015) and an especially precise synapse with extremely short synaptic delay, called the calyx of held (Englitz et al., 2009). In general, *SBCs* and *GBCs* enhance synchronization and lower jitter compared to the auditory nerve (Joris et al., 1994). The *MNTB* provides fast glycinergic inhibition to the ipsilateral *LSO* and ipsilateral *MSO*. The *LNTB* also synapses onto the ipsilateral *MSO* and provides glycinergic inhibition. The *MSO* and *LSO* are the first binaural stations in the brainstem and also the place of ITD and ILD extraction, respectively (Figure 6A & Figure 7A).

The *LSO* computes ILDs by subtracting the contralateral input, coming via the glycinergic *MNTB*, from the excitation received from ipsilateral *SBC* inputs (Moore and Caspary, 1983). The balance of inhibitory and excitatory inputs results in typical ILD functions of LSO neurons (Figure 6B). When a sound is louder at the ispilateral side (+ILD), excitation will outbalance contralateral inhibition and produce higher spiking rates. And vice versa, when a contralateral sound is louder (-ILD), inhibition surpasses ipsilateral excitation and thereby lowers the firing rate or even silences the *LSO* neurons. Commonly, in most LSO neurons the slope of the ILD function is steepest around or close to 0dB SPL ILD (Park et al., 1997; Tollin and Yin, 2002), which is reflected in results from psychophysical studies with highest ILD thresholds at the midline (Figure 6C). *LSO* neurons are sensitive to a range of ILDs and are usually saturating around +30dB SPL ILD and completely inhibited around -10dB SPL. Furthermore, the ILD function can be attenuated by release of GABA depending on recent stimulus history (Magnusson et al., 2008). This ILD function gain control mechanism is thought to underlie the increase in sensitivity for certain ILDs when trained with an adapter ILD as observed in psychophysical studies. Since the contralateral, inhibitory input has an additional synapse (calyx of held) compared to the ipsilateral, the timing of the inhibition relative to the excitation is crucial. Although precisely timed inputs are not required for the computation of an ILD, especially for ongoing activity, the timing becomes important for computing ILDs at the onsets of sounds. As a matter of fact, inhibition from the contralateral ear can even suppress the first spikes when the contralateral ear is stimulated at higher intensity than the ipsilateral (Tollin, 2003). For ILDs favoring the ipsilateral ear, excitation usually precedes inhibition by hundreds of microseconds. If the loudness on the inhibitory ear is increased, the latency of inhibition decreases and inhibition also becomes more efficient in suppressing action potential generation in the LSO.

This mechanism is thought to underlie the so called "time-intensity trading", a process that balances the strength and timing of the inputs and resolves ambiguity when an ITD is favoring another ear than the ILD (Grothe et al., 2010).
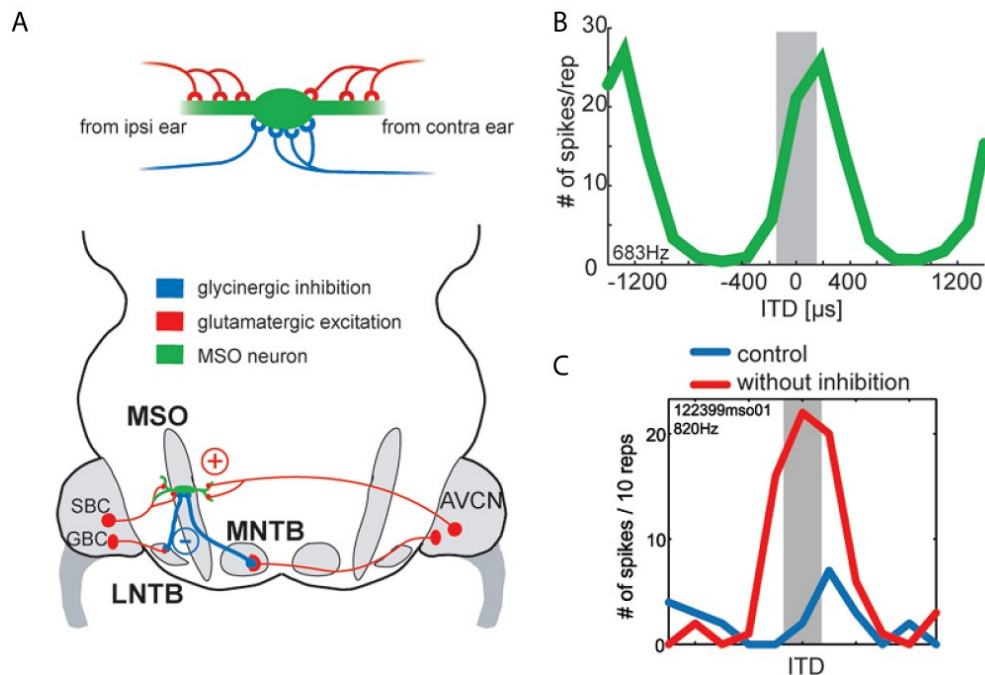
Figure 7: The MSO circuitry and ITD functions

A. The MSO neuron gets excitatory inputs from both ears, each clusters on the dendrite facing towards the projection. Inhibition from both ears clusters on the soma. The MSO circuitry is depicted below. SBCs from both ears provide binaural excitation to the MSO. The GBCs from the ipsilateral ear provides excitation to the LNTB, which in turn provides inhibitory output to the MSO. Via the calyx of held GBCs from the contralateral ear excite the *MNTB*, which inhibits the MSO in turn. **B**. A typical ITD function of a gerbil MSO neuron. ITDs favoring the contralateral ear lead to higher firing rates and the slope of the function is around midline. **C**. Blocking all glycinergic inhibition increases spike rates and shifts the ITD function towards the midline, becoming an "EE" coincidence detection neuron. Adapted from Grothe and Pecka et al., 2014 (with permission).

The *MSO* is the physiological basis for the extraction of ITDs. The *MSO* computes ITDs by performing coincidence detection of the two excitatory inputs, whereby the two inhibitory inputs set the timeframe for a successful coincidence of excitation, leading to a spike (Grothe and Pecka, 2014). Even the longest natural ITDs for a human listener (around 600-750µs) are just within the reach of e.g. the action potential duration (around 600µs) of a fast-spiking interneuron (Mallet et al., 2005). Therefore, it has long been puzzling how neurons can resolve such short durations, even down to tens of microseconds (Klumpp and Eady, 1956). The first proposed mechanisms for a neuronal coincidence detector was based on a theoretical model by Lloyd Jeffress (Jeffress, 1948). The so called Jeffress model employs a place code, where each cell would fire only at a distinct ITD. So for every ITD there would be a corresponding cell. The different arrival times of sound at the ears would be compensated by the differential length of the binaural excitatory inputs, so called

delay lines. The cell would fire at highest rates, when both excitatory inputs arrive at the same time. Indeed, this mechanism is actually employed by barn owls to extract ITDs (Carr and Konishi, 1990) and also other birds (Joseph and Hyson, 1993). However, in mammals no proof of delay lines was found. Intriguingly, physiological evidence points towards a different mechanism; ITD functions recorded from *MSO* cells in mammals commonly favor contralateral leading sound (+ITD) and peak outside of their physiological relevant ITD range (Goldberg and Brown, 1969) (Figure 7B). This means that the peak firing rate does not encode absolute position because the ITD resulting in the peak firing rate corresponds to a distance larger than the head width (McAlpine et al., 2001). Similar to ILD functions, the slope - and therefore the band with the highest dynamic range - of ITD functions in most *MSO* neurons is close to the midline (=0 ITD). Compelling evidence points towards precisely timed glycinergic inhibition setting the ITD shift or ITD tuning, since blocking inhibition shifts the ITD function and increases the firing rate (Pecka et al., 2008) (Figure 7C). Additionally, the physiology of *MSO* cells is adapted for fast integration by having short membrane time constants due to low input resistance set by large conductances at rest (e.g. K_{LVA}) (Khurana et al., 2011) and at hyperpolarisation (I_h) (Baumann et al., 2013). Thus excitation and inhibition have to interact on a short timeframe. Phase locked inhibition from the *MNTB* can even outrun contralateral excitation (Roberts et al., 2013) and co-modulate the ITD tuning together with inhibition from the *LNTB* (Myoga et al., 2014). Yet, the exact contribution of *LNTB* and *MNTB* in tuning the timeframe for excitation to result in an AP is still not clear. In sum, the data for coincidence detection in the *MSO* point towards inhibition setting the individual delay and a two-channel (hemispheric) code, where the readout of the relative activity of both *MSOs* encode the relative azimuth (Figure 8B), not necessarily in the form of a simple population code (Goodman et al., 2013) but with certainty not in the form of a place code.
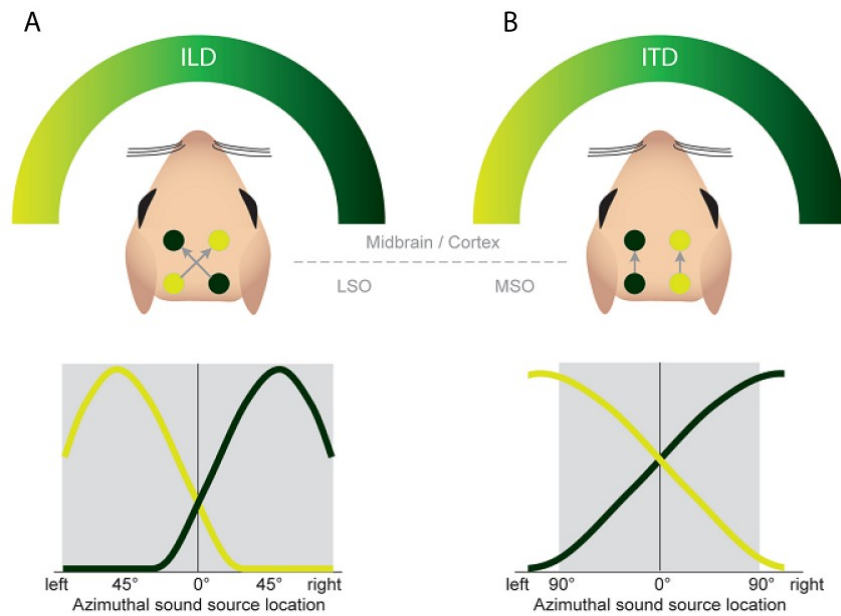
Figure 8: A two-channel, hemispheric code for ILDs and ITDs.

A. ILD functions in one hemispheric LSO are mirror-images of the ILD functions in the other hemisphere. On the path to the cortex, projections cross the midline. The relative activity in one hemisphere in relation to the other indicates azimuthal position. **B**. Also the ITD functions in one hemispheric MSO are mirrored in the MSO of the other hemisphere. Projections to the cortex do not cross the midline and therefore match the ILD output on the level of the cortex. Again the relative activity of both MSOs indicate sound source position in the horizontal plane. Adapted from Grothe and Pecka., 2014 (with permission).

1.3. The DNLL: a neural substrate for a precedence-like effect
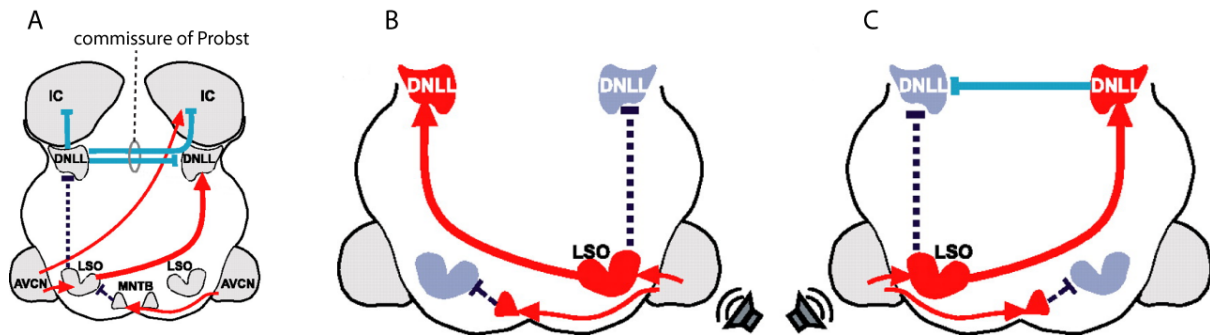
Figure 9: The *DNLL* circuitry and persistent inhibition

A. The LSO provides glycinergic inhibition (dashed grey) to the ipsilateral *DNLL* and glutamatergic excitation (red) to the contralateral *DNLL*. Glutamatergic excitation also projects from the AVCN to the contralateral *IC*. The *DNLL* provides GABAergic inhibition (blue) to the contralteral *DNLL* via the commissure of Probst and to the ipsilateral and contralateral *IC*. **B**. Stimulation paradigm without persistent inhibition. A sound on the right excites the right LSO, which inhibits the right *DNLL* and excites the left *DNLL*. **C**. Stimulation paradigm including persistent inhibition. A sound on the left excites the left LSO, which inhibits the left *DNLL* and excites the right *DNLL*. Additionally the right *DNLL* provides now GABAergic, persistent inhibition (blue) to the left *DNLL*, outlasting the glycinergic inhibition (dashed grey) from the left LSO. Adapted from Pecka et al., 2007 (with permission).

In the previous chapter the adaptations for precise and fast temporal integration of inputs were mentioned, that are a prerequisite for realtime extraction of ITDs and also to a lesser degree for ILDs. The mechanisms underlying the precedence effect on the other hand have to adapt to different time scales (>3ms), because these have to distinguish between the direct sound and its reflections. Physiological correlates of the precedence effect have been attributed to a suppression of neural responses to lagging sounds initially triggered by a leading sound (Litovsky et al., 2010). Suppressive effects following a leading sound have been observed on several stages in the auditory system, from the cochlea (Bianchi et al., 2013) up to the auditory cortex (Carlile et al., 1999; Litovsky et al., 2010). Whereas peripheral stages in the auditory pathway like the cochlea are rather unlikely to be the physiological substrates of the precedence effect (Brown et al., 2015a), more central processes exhibit precedence-like effects shaped by synaptic inhibition (Brown et al., 2015b).

One station, where strong suppression can be observed, is the *dorsal nucleus of lateral lemniscus* (*DNLL*). The *DNLL* is a GABAergic nucleus dorsally to the *superior olivary complex* (*SOC*) (Shneiderman et al., 1988). It gets its excitatory input from the contralateral *LSO*, the *VCN* and from the ipsilateral *MSO*. Glycinergic inhibitory input is provided by the ipsilateral LSO (Burger and Pollak, 2001; Kelly et al., 1998; Pollak et al., 2003). Via *the commissure of Probst* the *DNLL* synapses

GABAergically onto the contralateral *DNLL* and additionally sends GABAergic projections to both hemispheres of the *inferior colliculus* (*IC*) (Figure 9A) (Faingold et al., 1993; Glendenning et al., 1981; Ito et al., 1996; Oliver and Shneiderman, 1989; Pecka et al., 2007). *DNLL* neurons inherit the response properties of their respective *SOC* inputs: binaural excitable neurons (EE) are usually ITD sensitive and are innervated by the ipsilateral *MSO* (Seidl and Grothe, 2005). When inputs come from the *LSO*, neurons are contralaterally excited and ipsilaterally inhibited (EI) reflecting ILD functions (Pecka et al., 2007). Those EI neurons are not only inheriting the contralateral *LSO's* ILD function but are also glycinergically inhibited by the ipsilateral *LSO* (Figure 9B). *DNLL* neurons also improve the signal to noise ratio of their tuning functions by decreasing either jitter in action potential firing or by increasing the dynamic range with higher firing rates, for low frequency and high frequency neurons, respectively (Pecka et al., 2010). However, a crucial point for implication of the *DNLL* in the precedence effect is its impact on the spatial selectivity of *IC* neurons to sounds (Burger and Pollak, 2001; Pecka et al., 2007). The innervations from the *DNLL* help to generate so called "de novo ILD" sensitive cells (EI cells) in the *IC* by providing inhibition. Thereby *IC* neurons receive excitation either from the contralateral *CN* or from the contralateral *LSO*, whereas the inhibition in both cases is provided by the contralateral *DNLL*. This means that *IC* neurons can also be rendered spatial selective i.e. ILD sensitive via the *DNLL*. An additional key feature making the *DNLL* a candidate player in the precedence effect is the reciprocal GABAergic inhibition via the *commissure of Probst*. Stimulus evoked GABA release at the *DNLL-DNLL* synapse induces inhibitory chloride currents in the contralateral *DNLL*. These inhibitory post-synaptic currents (IPSCs) outlast the auditory stimulus duration up to tens of milliseconds (Yang and Pollak, 1994) and therefore suppress responses in the contralateral *DNLL*. This long lasting inhibition is called persistent inhibition (PI) (Figure 9C). Now, if an initial sound induces PI in the contralatral *DNLL*, in the following the suppressed *DNLL* temporarily fails to shape de-novo ILDs in *IC* neurons during the period of PI. Consequently, neurons in the *IC* can now respond to a greater spatial variety of lagging sounds due to the temporal relief from the *DNLL* inhibition (Burger and Pollak, 2001). *In vitro* and *in vivo* evidence pinpoint the underlying mechanism for this long lasting PI to asynchronous release and spillover, leading to synaptic saturation (Ammer et al., 2015a). By blocking excitatory transmission *in vivo* at the contralateral *DNLL*, PI can be abolished (Burger and Pollak, 2001), because the *DNLL* cannot be excited anymore. When PI is in effect, the contrallateral *DNLL* is unresponsive to lagging sounds. Blocking excitation in the contralateral *DNLL* mimics PI and as mentioned before, thereby the ipsilateral *IC* is relieved from the contralateral *DNLL*'s GABAergic inhibition. The ipsilateral *IC* is now responding to lagging sounds that would be suppressed without a previous leading sound.

Electrical stimulation at the *commissure of Probst* also suppressed action potentials even within a spike train in *DNLL* neurons, whereas blocking GABA$_A$ receptors during electrical stimulation of the *commissure of Probst* restored firing in *in vitro*

experiments (Pecka et al., 2007). *In vivo* extracellular recordings showed that acoustic stimulation with increasing ILDs favoring the ipsilateral ear also led to an increased duration of PI in the *DNLL*. Modeling the responses to a lead and lagging binaural sound at the level of the *IC* including PI from the *DNLL* also confirmed that the *IC* not only responds to the leading sound with an ILD favoring the contralateral ear but a portion of *IC* cells also respond to the lagging sound with an ILD favoring the ipsilateral ear. This is due to the mentioned relief from *DNLL* inhibition by PI, which is thought to suspend the de-novo ILD sensitivity in the *IC*. The model also predicted that without PI, the *IC* only responds to the sound with an ILD favoring the contralateral ear. Therefore PI generates an additional response to a lagging sound from various regions in space at the level of the *IC*. This additional response can be thought of as a tag for higher brain areas to categorize the lagging sound as an echo (Pecka et al., 2007).

Other studies also provide strong evidence for the general importance of the *DNLL* in sound localization: Transecting the *commissure of Probst* in rats resulted in deteriorated performance in sound localization tasks (Ito et al., 1996). Unilateral and bilateral lesions in the *DNLL* of rats also worsened their localization acuity for sounds in the horizontal plane (Kelly et al., 1996). The *DNLL* shapes the tuning functions of IC neurons by providing *GABAergic* inhibition (Faingold et al., 1993; Faingold et al., 1991). All the mentioned, accumulated evidence implies that the *DNLL* very likely could be the physiological substrate for the precedence effect or at least is a key player in it. An experiment to conclusively confirm the *DNLL*'s contribution in the phenomenon precedence is still lacking though.

1.4. Optogenetics
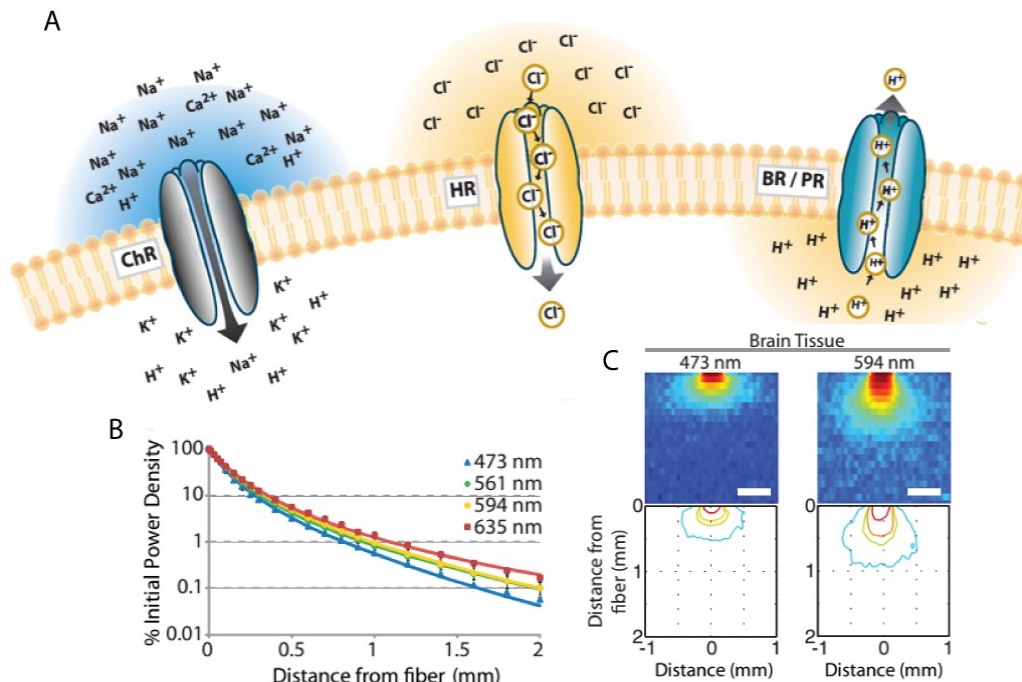
Figure 10: Rhodopsins variants and light propagation in brain tissue

A. Channelrhodopsins (ChR in grey) are light gated cation channels, halorhodopsins (HR in yellow) are light driven chloride pumps and bacteriorhodopsins (BR in blue) are light driven proton pumps, e.g. "ArchT". **B**. Losses in light transmission for several wavelengths in nervous tissue. **C**. Light propagation at the end of a 200µm optical fiber in brain tissue. Isocontour lines indicating 50% (red), 10% (orange), 5% (yellow) and 1% (light blue) from initial light power . Adapted from Yizhar et al. 2011 (with permission).

In order to understand the brain and to decipher neural circuits, the involved neurons have to be manipulated in a controlled and systematical fashion.

The concept of optogenetic follows the idea that a stimulus, that is a priori intrinsically not meaningful or were no sensitivity exists to, can be used to influence the activity of neurons. An issue with electrical stimulation is that it is directly instructive to all neurons to fire and therefore non-specific to neuronal cell types. Furthermore, the effect of a stimulation electrode can only by focused by decreasing current and voltage and is only excitatory. Drugs on the other hand are operating on a very slow timescale, are sometimes not reversible and also sometimes unspecific. Francis Crick formulated the basic idea in an article in 1979 (Crick, 1979), that light would be an appropriate stimulus due to the fact, that besides photoreceptor cells neurons are unresponsive to light, light can be easily focused to a region of interest and it is operating on the fastest possible timescale. With the advent of optogenetics another very powerful method was introduced into neurosciences. Optogenetics utilizes the delivery of genes encoding for light-gated ion channels or pumps to

confer light sensitivity to previously light insensitive target neurons for directly controlling their synaptic activity and output. The "genetical" part arises from the fact that neurons are usually not responsive to light, hence light sensitivity needs to be introduced first, which is achieved by genetic engineering. Proteins, *rhodopsins*, exhibiting light sensitivity have been described already early: in 1971 *bacteriorhodopsin (Oesterhelt and Stoeckenius, 1971)*, *halorhodopsin* in 1977 (Pettei et al., 1977) and only in 2002 *channelrhodopsin 1 and 2 (Nagel et al., 2002; Nagel et al., 2003)* (Figure 10A). In their paper Nagel et al. already suggest the possible use of *channelrhodopsins* (ChR) for rendering neurons or other cells light responsive. At the same time, genetic tools have become more advanced to enable expression of bacterial transgenes in neurons. In the pioneering study of Boyden et al., action potentials were elicited with light pulses in rat *hippocampal* neurons expressing *channelrhodopsin* 2 (Boyden et al., 2005). This was the first application of the optogenetical concept and the proof of principle. Only months later another study reported the successful manipulation of behavior with light in nematodes (Nagel et al., 2005). Further studies also revealed that *all-trans-retinal* does not have to be supplied but is already present in neurons. Furthermore, subsequent studies employing other *opsin* proteins also achieved different effects (Deisseroth et al., 2006; Fenno et al., 2011; Yizhar et al.; Zhang et al., 2010).

1.4.1. Excitatory action of C*hannelrhodopsins*
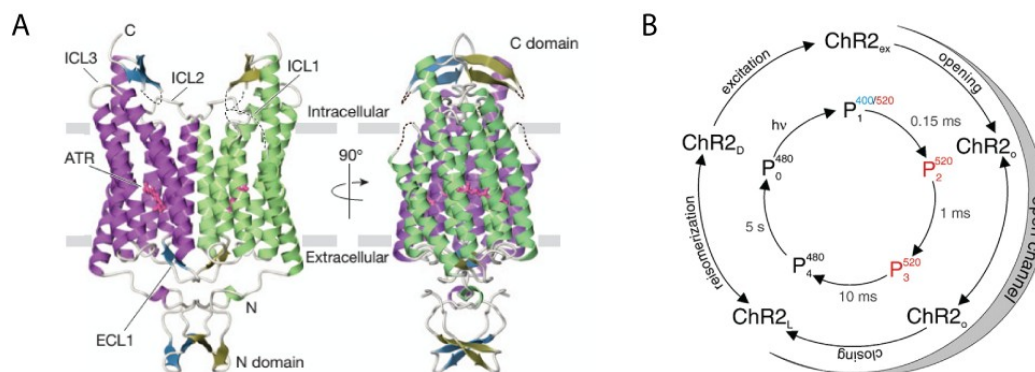
Figure 11: The crystal structure and photocycle of channelrhodopsin 2

A. Molecules of ChR2 (green and mangenta) form dimers in the plasma membrane (grey bars). The N-terminus and one extracellular loop (ECL1) face the extracellular side, the C-terminus and three intracellular loops (ICL) face the cytoplasmatic side. The seven transmembrane domains (TM) are formed by α-helices and all-trans-retinal is covalently bound to TM7. The watery pore is formed by four TMs (1, 2, 3 and 7). Adapted from Kato et al., 2012 (with permission). **B.** The photocycle of ChR2 starts with the dark adapted ground state (ChR2$_D$) and its spectral corresponding P480 (P$_0$) state. When stimulated with blue light an excited state (ChR2$_{ex}$) is characterized by its spectral intermediate P400 (P$_1$), which leads to the photointermediate P520 (P$_2$ and P$_3$) and an open state of the channel (ChR2$_O$). The channel closes and the light adapted rhodopsin (ChR2$_L$) relaxes (P$_4$) and returns to its ground state. Adapted from Bamann et al., 2007 (with permission).

The *channerhodopsins* are seven transmembrane domain (TM) proteins and belong to the type I *opsins*, that comprises the bacterial *opsins*. In contrast to type II *opsins*, encompassing the animal *opsins* like ciliary or rhabdomeric *opsins* used in vision which are G-protein coupled receptors (GPCR). *ChR2* is a non-specific cation channel isolated from the green algae *chlamydomonas reinhardtii*. It is expressed in its eye spot and used to guide phototaxis. *ChR2* is found as dimers in the plasma membrane (Figure 11A). Nearly all available channelrhodospins are mutations or chimeras of *ChR2*, therefore the structure and function of *ChR2* are well studied. TM1,2,3 and 7 make up the watery pore conducting mono- and divalent cations (Na$^+$, K$^+$, H$^+$ and Ca^{2+}). *ChR2* has a small conductance of <1 pS and its reversal potential is around 0mV at physiological conditions. The photosensitivity is conferred by all-trans-retinal, covalently bound to K257 (=lysine) at TM7 (Kato et al., 2012). When the bound all-trans-retinal is energized with photons around the absorption maximum at 470nm, it is photoisomerized to 11-cis-retinal. This conformational change induces an opening of the channel (photocurrent τ$_{on}$ ~1.21ms). In absence of light the photocycle of retinal leads to a delayed or "uncoupled" closure of the channel's pore (photocurrent τ$_{off}$ ~13.5ms) (Nagel et al., 2003). Returning of the closed, light adapted ChR2 to the ground state takes at least 5s (Figure 11B)

(Bamann et al., 2008). The peak photo current is approximately 5 times higher than the "steady state" current (though these measurements of steady state photocurrents are not the real equilibrium current but usually only indicative of the last milliseconds of a photocurrent to 1 s long light pulse), indicating high desensitization. In sum, all these characteristics make ChR2 directly light gated. By mutating amino acids (AA) or fusion and exchange of protein domains certain characteristics can be enhanced or diminished. By optimizing the bacterial codons for expression in mammalian cells, the widely used mutant human ChR2 (hChR2) (Zhang et al., 2006) was the basis for further molecular engineering (see Yizhar et al., 2011 for review). Exchanging certain AAs (H134R) lead to higher photocurrents and lower desensitization at the expense of slower kinetics (Lin et al., 2009; Nagel et al., 2005). Another set of mutations is based on the E123T/A mutation (=ChETAs) that eliminates the dependence of channel closure on membrane voltage, thereby speeding up the τ_{off} to ~4-4.5ms (Gunaydin et al., 2010) but again at the expense of a smaller photocurrent compared to the wildtype. Paired with the mutation T159C, the photocurrent increases but also channel closing slows down (Berndt et al., 2011). Another mutation L132C (Kleinlogel et al., 2011) focuses on increased photocurrent by shifting the balance of the pore's ion selectivity filter to Ca^{2+}. This point mutant L132C called "*CatCH*" (for calcium translocating channelrhodopsin) is described as light gated, "membrane bound calcium source" and exhibits 3-4 fold increase in photocurrent compared to wildtype ChR2, a small shift in absorption maximum (474nm), >10 fold increase in light sensitivity and with τ_{off} 16ms still faster kinetics than hChR2 (H134R). Another approach led to the ChR1 and ChR2 chimeras, called "ChIEF" and "ChEF" that exhibit very little photocurrent desensitization and fast kinetics, with ChIEF having the faster τ_{off} (12ms vs. 25ms) but at the expense of a lower photocurrent (Lin et al., 2009). By mining genes of photoactive microorganisms other channelrhodopsins have entered the optogenetic toolbox. The opsins were nicknamed "Crimson" and "Chronos", the first having an absorption maximum at 590nm but very slow kinetics and the latter having the fastest off kinetics to date (τ_{on} is slower with 2.3ms than wildtype ChR2 but very fast τ_{off} 3.6ms) and its absorption maximum at ~490nm (Klapoetke et al., 2014). Both have 3-4 fold higher photocurrents when stimulated at their excitation wavelength than wildtype ChR2. All mentioned channelrhodopsins have been tested *in vitro* and *in vivo* and managed to elicit spikes in light stimulation experiments. Parameters for efficient light stimulation have to be quantified though for each case individually.

A phenomenon that can be seen with all channelrhodopsins is the depolarization block upon long light pulses or high frequency trains and high light intensities. Usually the block becomes more prominent when photocurrents are bigger. In nearly all optogenetic studies with ChR2 or variants, this block can be observed though it is not always reported or mentioned. As the name indicates, light stimulation ceases to be effective because neurons fail to repolarize, subsequently stop to depolarize and maybe build up a plateau potential. The mechanism leading to the depolarization block is not completely understood but is most likely caused by the high cation

currents and prolonged membrane depolarization (Bianchi et al., 2012). The extent of the depolarization block differs between neuronal cell types and is thought to be lowest in fast spiking neurons and also for low input resistance (Herman et al., 2014). In their study Herman et al. actually proposed to use this epiphenomenon to silence neurons by driving them into the depolarization block (Herman et al., 2014). However, short light pulses are recommendable to avoid the depolarization block, but no rule of the thumb exists. Therefore, in this regard light stimulations parameters also have to be tested for each cell type individually.

Light delivery into the intact brain poses a challenge due to the refractive nature of the nervous tissue (lipid bilayers and cytoplasm have a different refractory index, as well as blood in the vasculature, etc.). This physical properties result in diffraction and absorbance of light when passing through these different phases. Light intensities of longer wave lengths are less attenuated than short wavelengths. Shorter wavelengths are scattered and absorbed more often because the sizes of more particles (atoms and molecules) are in the range of the wavelength. Light intensity shows roughly $1/r^2$ (r=distance) attenuation in brain tissue, yet through high scattering in the brain the actual term is more complex (Vo-Dinh, 2014). To quantify intensity losses, light propagation in sections of acute brain tissue with various thicknesses was measured, highlighting the importance of spatial vicinity between light source and target channelrhodopsins (Figure 10B&C). Even with the most efficient channelrhodopsin variants (requiring ~0.01mW / mm^2, for spurious firing though) the distance e.g. from the lambda suture to the *MNTB* (>8mm) is too long for a 100mW laser to elicit spikes in the *MNTB*. Therefore neurons expressing channelrhodopsins can only be precisely controlled with light when close to the light source or at a distance that is saturated with light. Usually fibre optics are used to bring light source and channelrhodopsins expressed in the brain closer together. Most *in vivo* studies use multimode optical fibres with diameters from 100-200μm and insert the bare fibre sometimes coupled with electrodes (="optrodes") or insert the fibre through an implanted cannula (Dufour and De Koninck, 2015).

1.4.2. Inhibitory action of Channelrhodopsins

A major advantage of optogenetic tools in comparison to electrical stimulation is the possibility to silence neurons. Until recently, all rhodopsins discovered to hyperpolarize the cell are light driven pumps, pumping either positive charge (protons) out of or negative charge (chloride) into the cell. The genes for the proton pump "ArchT" were isolated from *Halorubrum sodomense*, an archeal halobacterium (Han et al., 2011). The protein expresses well in mammalian neurons, efficiently traffics to the plasma membrane and enables suppression of spiking *in vitro* and in

vivo. Peak absorption occurs at 566nm and its photo current rise time (15-85%) takes ~10 ms and has a fall time of ~22ms. Average photocurrents reach around 600pA. pH levels in the cytoplasm do not change upon light stimulation of ArchT, but no data exists for the extracellular milieu. Another class of light drive pumps was isolated from *Natronomonas pharaonis*, also an archeal halobacterium (Han and Boyden, 2007; Zhang et al., 2007). This pump called *Natronomonas pharaonis halorhodopsin* (*NpHR*) hyperpolarizes the cell by pumping chloride into the cytoplasm and has an absorption maximum at 590nm. Yet the protein only partially traffics to the plasma membrane, forms cytotoxic aggregates in the cytoplasma and endoplasmatic reticulum (ER) and therefore only small photocurrents (~70-100pA) can be elicited. Photocurrent rundown by retinal depletion can be counteracted with brief flashes of blue light (470nm). By adding the trafficking signal from a vertebrate inward rectifier potassium channel to the C-terminus of *NpHR* (*NpHR2.0*), aggregates in the ER can be abolished but membrane trafficking is still incomplete (Gradinaru et al., 2008). By adding the trafficking signal from Kir2.1 to the C-terminus of *NpHR* or to the linker of the fluorescence tag, *NpHR* aggregates can be avoided and trafficking to the membrane greatly improves (*NpHR3.0*) (Gradinaru et al., 2010). *NpHR3.0* has a 20 fold increase in light sensitivity compared to *NpHR*, fast kinetics with a τ_{off} of ~4.2ms and increased average photocurrent of ~750pA. Even single spikes in a spike train (<50Hz) can be suppressed with sufficient precision. As side effect of prolonged and continuous photostimulation with *NpHR3.0*, a change in chloride concentrations can occur and thereby the receptor reversal potential of $GABA_A$ receptors can be affected (Raimondo et al., 2012). A disadvantage of all these ion pumps is the transport of only a single charge per photocycle, which requires constant illumination and favorably at near saturating light intensities. Due to precise structural data (Gaiko and Dempski, 2013; Kato et al., 2012) and increasing knowledge of ChR2 action, a conversion of ChR2 to a light gated chloride conductance is achieved by building on the ChR2-T159C mutant and mutating to E90 to R (Wietek et al., 2014). Nonetheless the photocurrents of this mutant nicknamed "ChloC" are rather small and depend largely on the transmembrane potential, i.e. the electrochemical gradient (naturally, more positive potentials lead to higher anionic inward photocurrents; higher external chloride concentration lead to higher chloride influx). Thus pairing ChloC with step function mutations that delay the closure of the channel increase the integrated photocurrent greatly. The advantage of this step function ChloC or "slow ChloC" opsin is the higher light sensitivity when compared to *halorhodopsin* or ArchT; already dim levels of $0.001mW/mm^2$ elicit already photocurrents that might suppress spiking. This means also neurons further away from the light source or fibre tip can be effectively suppressed. The disadvantage is the very imprecise closure of ChloC with a τ_{off} of ~11 s, increasing interstimulus intervals greatly.

1.5. Genetransfer with recombinant *Adeno-Associated Virus* (*rAAV*) vectors

Humans are the primary host of *AAVs* and *AAV2* is the most frequent serotype with >80% seropositivity in the population (Calcedo et al., 2009). No pathologies are known for *AAVs* and up to date more than 12 naturally occurring subtypes are described, all displaying a slightly different tropisms or preferences for certain cell types. Therefore some serotypes are preferable over others when a certain cell type has to be targeted (Aschauer et al., 2013a; Burger et al., 2004; Zincarelli et al., 2008). *AAVs* are *dependoviruses* belonging to the family of *Parvoviridae*. They can infect dividing and non-dividing cells, but like all dependoviruses require a helpervirus for the replication of its genome, which is usually the *Adenovirus (or Herpesvirus)*. Therefore they were named *adeno-associated virus (Atchison et al., 1965)*. Its genome is organized on a single stranded (ss) and 4.7 kilobases long DNA molecule. The genome encodes two genes, the rep and the cap gene (Figure 12A). The *rep* gene consists of four overlapping genes from two RNAs (with increasing size: *rep40*, *rep52*, *rep68*, *rep78*) and are required for replication and packaging. Due a motif acting as a *rep* binding site, wild type *AAV* can integrate into this specific site (*AAVS1*) on the chromosome 19 with a frequency of 70% (Dutheil et al., 2000). The *cap* gene codes for three structural proteins (VP1, VP2, and VP3), which make up the icosahedral capsid in an estimated 1:1:10 stoichiometric composition (Halder et al., 2015). The capsid is about 20nm in diameter and assembled from 60 VP proteins in total (Berns and Giraud, 1996; Linden and Berns, 2000). The *rep* and *cap* genes are flanked by the two inverted terminal repeats (ITR), which are each 145 bases long and due to their palindromic sequence can form a hairpin structure. This hairpin structure is essential as a replication origin and also for the packaging of the virus DNA into the capsid. By deleting a resolution site in one terminal ITR, a mutant *AAV* can be created that yields a self-complementary (sc) or double stranded (ds) *AAV* genome (*ds/scAAV*). This mutant resolves the *AAV's* dependence on the hosts replication machinery to create a double stranded genome intermediate and therefore circumvents one of the bottle necks in *AAV* transduction, speeding up expression and transduction efficiency (McCarty, 2008). This comes at the expenses of only half the available genome size (~2.5kb). When genomes larger than 4.7kb are packaged into the *AAV* capsid, the packaging efficiency goes down and genomes bigger than 5.2kb are not packaged (Wu et al., 2009). To utilize the *AAV* as a vector for gene delivery, the genome is replaced with transgenes, except for the ITRs which have to be provided in cis in order for the transgene to be packaged into the capsid and replicated in the host (Figure 12A). An *AAV* modified in this way is called recombinant *AAV* (*rAAV*) and has a packaging capacity up to 5.2kb excluding both ITRs (Hermonat and Muzyczka, 1984). In order to produce *rAAVs* the rep and cap genes have to be provided in trans as helper plasmids. This ensures that *rAAVs*
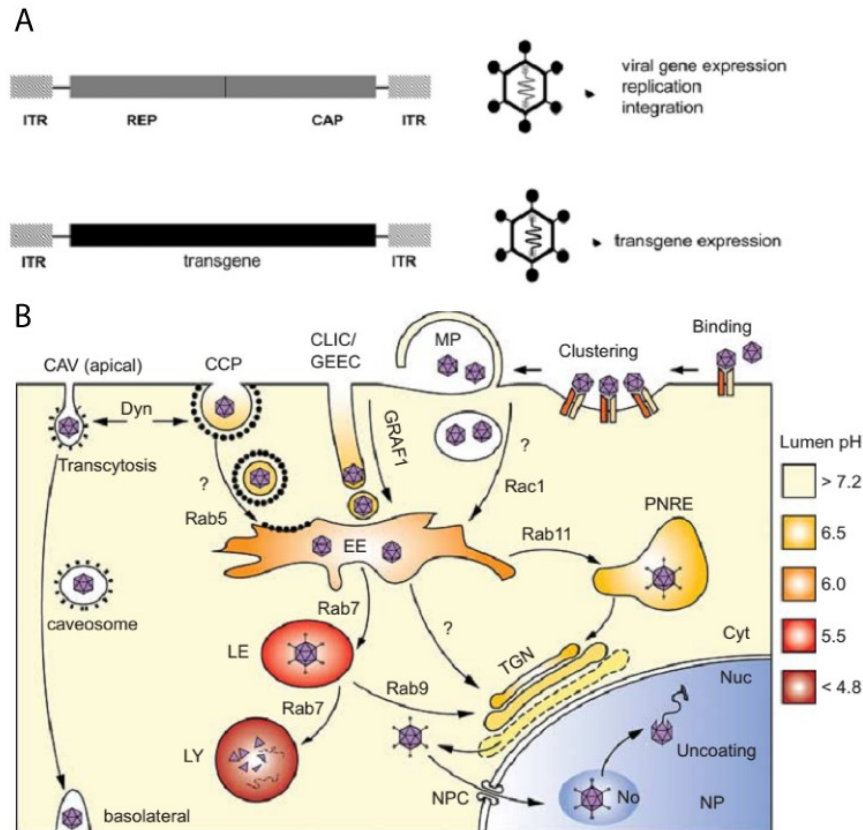
Figure 12: *AAV* genome and transduction of host cells

A. The genome of the wildtype *AAV* contains the rep and cap genes flanked by the ITRs. The genome is packaged in the icosahedral capsid. The *AAV* vector has its whole genome replaced by the transgene(s) and is only capable of shuttling the DNA into the host cell. Adapted from Büning et al., 2004 (with permission). **B**. *AAV* binds to the receptors on the cell surface and can be taken up via several endocytotic pathways. Through clathrin-independent carriers/GPI-enriched endocytic compartment (CL*IC*/GEEC) endocytic pathway, via clathrin coated pits (CCP) or by caveolar endocytosis (CAV) *AAVs* can enter. Early endosomes (EE), late endosomes (LE) and perinuclear recycling endosomes (PRNE) are intermediate steps towards the trans-Golgi network (TGN). Through acidification capsid proteins change conformation and escape the LE or are proteolysed (LY). Escaped virions enter the nucleus (Nuc) via the nuclear pore complex (NPC) and release the DNA by uncoating from the capsid. Adapted from Nonnenmacher et al., 2012 (with permission).

are replication deficient. Usually a *rAAV* expression construct or expression cassette consists of a specific promoter, the transgene of interest, a polyadenylation signal and eventually posttranscriptional regulatory elements, e.g. *Woodchuck Hepatitis Virus Posttranscriptional Regulatory Element* (WPRE) (Paterna et al., 2000) .

The process of transduction (=entry of the virus and release of its DNA) is initiated by the binding of the virion to the plasma membrane (Figure 12B). *AAV* binds to heparan sulfate proteoglycans as its primary target receptor (Summerford and Samulski, 1998). Other receptors that are important for binding are fibroblast growth

factor 1(Qing et al., 1999), integrin αß1, integrin αß5 (Summerford et al., 1999), laminin receptor (Akache et al., 2006) and the hepatocyte growth factor (Kashiwakura et al., 2005). Once the viruses have bound, the internalization starts via endocytotic pathways. The virus-receptor complex is taken up, probably via clathrin coated pits and/or other clathrin independent mechanisms (Nonnenmacher and Weber, 2012). The next step in the endocytosis is the formation of the endosome retaining the virus-receptor complex and subsequent acidification and transport of the endosome to the nucleus. It is thought, that the acidification in the late endosome and the perinuclear recycling endosomes induces release from the receptors and causes conformational changes in the VP1 and VP2 proteins and thereby enables subsequent release of the viruses from the endosome. *AAVs* enter the nucleus through the nuclear pore complex, where uncoating is thought to happen. After replication via the host cell protein machinery, double stranded *AAV* DNA is available for transcription and ensuing gene expression. Commonly, the *rAAV* genome copies form head-to-tail concatamers, persisting in a stable, episomal state. This allows for long term expression and most importantly does not alter the host genome (Duan et al., 1998).

Previous work by Christian Porres (Porres C., 2012) on gene delivery into the *Mongolian Gerbil's* central nervous system, especially the midbrain and brainstem, showed that lentiviral vectors with *CamKIIα* promoter failed to transduce neurons therein. Exchanging the promoter with *synapsin I* helped to transduce neurons in the *IC* but failed to transduce neurons in the *MNTB*. Other tested viral vectors like the *Semliki-Forest-Virus* and *Pseudo-Rabies-Virus* also failed to meet the requirements as reliable gene delivery system for our model organism. Therefore, the use of *rAAV* vectors for a reliable gene delivery into neurons of the gerbil auditory brainstem and midbrain might be a working alternative.

In sum, *rAAV*s are easy and safe to use due to their lack of pathogenicity, low immunogenicity, replication deficiency and therefore low biological safety level. Also the production is safe due to the deconstruction of the *AAV* genome and provision of required genes in trans. *AAVs* effectively transduce neurons and allow long term expression without mutating the host cell.

1.6. The *Mongolian Gerbil* as a model organism for hearing

The *Mongolian Gerbil (Meriones unguiculatus)* is a popular model organism for human hearing. Its audiogram largely overlaps with that of human's, with an extended hearing range for higher frequencies but a decline in lower frequencies (Ryan, 1976). Gerbils can localize sounds in the horizontal plane based on their ILD as well as ITD (Maki and Furukawa, 2005b). Its physiological spectrum for ITDs range from +/- 120µs and the maximal natural ILD of about 30dB SPL occurs at

~30kHz. The *gerbil* has prominent and well described LSOs and MSOs extracting either ILDs and ITDs (Grothe and Pecka, 2014). Their performance in listening tasks mimicking the cocktail party effect are comparable to human listeners (Lingner et al., 2012). The circuitries underlying sound localization and potentially the precedence effect are well described *in vitro* and *in vivo* (Ammer et al., 2015a; Grothe et al., 2010; Grothe and Sanes, 1994; Pecka et al., 2008; Pecka et al., 2007; Seidl and Grothe, 2005; Siveke et al., 2006). Also similar to the human hearing, the *gerbil* auditory system also suffers from age related hearing loss (Mills et al., 1990).

Albeit the gerbil has many advantages as a model organism for hearing, it has also deficits in regards to its accessibility as a laboratory animal model. Up to now, no transgenic or knock-out gerbils exist. Its genome has not been sequenced and annotated. Little is known about the molecular identity of neuronal subtypes and circuitries, besides the increasing body of physiological and immunohistochemical evidence. The breeding and reproduction of gerbils is also more complicated than compared to mice. Gerbils are nearly monogamous, their sexual maturation, the female-male pair formation and subsequent breeding (first litter ~ 50 days after pair formation on average) are time consuming and not always successful (Ågren, 1984; Salo and French, 1989). Nonetheless, mice are no alternative model organism for human hearing because mice rely on ILDs for sound localization in the horizontal plane. Their hearing range does not extend below 4/5kHz, whereas humans show the highest hearing sensitivity from 2-5kHz (Ryan, 1976). Furthermore, the MSO is barely developed in mice and no study so far has characterized if there is any ITD computation in mouse MSO (Kuwabara and Zook, 1992).

1.7. Motivation and Aim of study

No means for silencing and exciting neurons with the spatial and temporal precision offered by optogenetics, are available for experiments in the *Mongolian Gerbil*. In addition to the methods that became standard in electrophysiology, *in vivo* and *in vitro*, optogenetic methods would therefore aid greatly in understanding the functions of auditory circuits by reversibly activating or silencing defined elements or nuclei in the circuit. A successful application in optically driving or silencing the *MNTB*, *in vitro* and *in vivo*, can help to decipher the role of glycinergic inhibition from the *MNTB* in the computation of ITDs. Another major and important application is the optical manipulation of the *DNLL*, which would allow to prove existing hypotheses about the *DNLL's* role in the precedence effect. It is still unclear where in the auditory system the physiological basis for this perceptual phenomenon resides. As mentioned before (see chapter 1.3), current hypotheses imply that the *DNLL* shapes the spatial selectivity of *IC* neurons to sound. This spatial selectivity can be temporarily suspended for lagging sounds when the *DNLL* is persistently inhibited by an initial sound. By reversibly manipulating the *DNLL* with light in *in vivo* experiments the following points can be addressed: (1) Optically silencing or stimulating the *DNLL* should lead to decreased or increased PI in the contralateral *DNLL*. This would further harden the evidence collected by several studies identifying the *DNLL* as the source of PI (Ammer et al., 2015b; Pecka et al., 2007). (2) Silencing or activating the *DNLL* should mimic PI or temporarily suppress it (Burger and Pollak, 2001). Thereby the ILD sensitivity in a portion of the *IC* should be turned off or on for the duration of the light pulse. (3) In sound localization tasks stimulating or silencing the *DNLL* optically should impact on the listening performance when a precedence effect paradigm is used. A temporarily inactivated *DNLL* should confuse the perception and localization of a leading and lagging sound.

Therefore establishing optogenetic tools for *in vivo* applications in the *Mongolian Gerbil* is a key technology for our understanding of the precedence effect and of course optogenetic approaches would also help to clarify other scientific questions.

This study aims to establish optogenetic methods in the auditory brainstem and midbrain of the *Mongolian Gerbil*. In order to express channelrhodopsins in designated auditory nuclei, initially a reliable gene delivery vector needs to be established. Once gene delivery is established, the channelrhodopsins need to be characterized *in vitro* to estimate their effect on neuronal spiking and to design an efficient light stimulation protocol. In a final step and proof of principle experiment, sound evoked neuronal spiking needs to be manipulated with light in transduced neurons of the auditory system *in vivo*.

Firstly, *rAAV's* aptitude as a neuron specific and reliable gene delivery tool needs to be tested (see *Results* section, chapter 4.2 for additional details). Therefore appropriate *AAV* plasmids (*pAAVs*) have to be cloned in the first place. Subsequently the plasmid vectors have to be processed into functional

rAAV2/8Y337F vectors. Most importantly, these vectors need to be tested by injecting them in the *MNTB, IC* and *DNLL*. The conditions that have to be met by the *rAAV* vector in all these three auditory nuclei are: (1) transduce neurons; (2) specifically and exclusively drive expression of a functional transgene in neurons; (3) the expression should be stable over time but should also have a fast onset (≤2 weeks); (4) transduce as many neurons as possible i.e. at least 30-50% of the neurons in an injected area; (5) the expression level should be high enough that finally the expressed *ChRs* impact on the membrane potential. Only when all these criteria are fulfilled, the vector is used to express *ChRs* in the next set of experiments. Otherwise a different *AAV* serotype will be tested.

Secondly, the impact and properties of different *ChRs in vitro* need to be characterized. The appropriate expression times, the kinetics, light dependence and success rate in photostimulation have to be determined for different *ChRs*. *In vitro* patch-clamp recordings from transduced neurons in acute brain slices serve to directly or indirectly measure these properties. Only if the tested *ChR* is successful in eliciting or suppressing spikes with light and the other mentioned properties are known, optogenetic stimulation requirements for an *in vivo* application can be estimated.

Thirdly, the optogenetic application of the candidate *ChRs* needs to be tested and established in extracellular *in vivo* recordings in the *IC* and *DNLL*. In a proof of principle experiment and as a final criterion, either auditory evoked spiking has to be suppressed with light (*NpHR3.0*) or spiking has to be elicited with light in the absence of auditory input (*CatCH*). Only when this last condition is met, optogenetics is finally established *in vitro* as well as *in vivo* in the auditory system of the *Mongolian Gerbil*.

This would also pave the way for further applications of optogenetic methods e.g. for in depth optogenetic *in vivo* and *in vitro* experiments and even for optogenetic experiments with freely behaving animals, none of which has been possible in the *Mongolian Gerbil* before.

1.8. Contributions

Thanks to the collaboration with PD Dr. Stylianos Michalakis I was able to clone new *rAAV* vectors in his laboratory. Fred Koch helped me with the cloning of the first p*AAV*2-ss-hSyn-GFP-WPRE construct. Molecular cloning of the other vectors was done by me, cell culture work was done by Elisabeth Schulze and me and final *rAAV* purification was also done by Elisabeth Schulze and me. Virus titering was done by Fred Koch and Elisabeth Schulze. Counting of transduced MNTB neurons was done by Barbara Beiderbeck.

2. Material

2.1. Molecular Cloning

2.1.1. Constructs

pAAV2-ss-hSyn-EYFP-WPRE

pAAV2-ss-hSyn-GFP-WPRE

pAAV2-ss-hSyn-CatCH-mcherry-WPRE

pAAV2-ss-hSyn-ChETA-mcherry-WPRE

pAAV2-ss-hSyn-CatCH-mcherry-T2A-NpHR-WPRE

pAAV2-ss-hSyn-NpHR-EYFP-WPRE

pAAV2-ss-hSyn-Arclight Q239-WPRE

pAAV2-sc-hSyn-NpHR 3.0-mcherry-SV40pA

for injections diluted to a concentration 9.5-9.8x10^8 gc/µl

2.1.2. Cloning primers

All sequences are listed in 5' to 3' direction

Forward primer:"fw-SalI-Cat"

TATAGTCGACATGGATTATGGAGGCGC

Reverse primer:"rev-HindIII-Cat"

GGCTGGCGCGGTACCCAAGCTTAT

Forward primer:"fw-HindIII-chry"

TATAAAGCTTATGGTGAGCAAGGGCG

Reverse primer:"rev-HindIII-chry"

CGAGCTGTACAAGTAAAAGCTTAT

Forward primer:"fw-SalI-ChE"

TATAGTCGACATGGACTATGGCGGC

Reverse primer:"rev-HindIII-ChE"

CCGGCGCGGTACCCAAGCTTATA

Forward primer:"fw-HindIII-chry"

TATAAAGCTTATGGTGAGCAAGGGCG

Reverse primer:"rev-HindIII-chry"

CGAGCTGTACAAGTAAAAGCTTAT

Forward primer: "Fw-Syn-SalI"

ACATGTCGACGTGTCTAGACTGCAGAGGGCCCTGC

Reverse primer: "Rev-NpHR-TS"

ATCCTCCTCGCCCTTGCTCACCATCACGTTGATGTCGATCTGGTCCAGGG
G

Forward primer: "Fw-mCherry-oh"

CTGGACCAGATCGACATCAACGTGATGGTGAGCAAGGGCGAGGAGGATA
AC

Reverse primer: "Rev-mCherry-ER"

TTACACCTCGTTCTCGTAGCAGAACTTGTACAGCTCGTCCATGCCGCCGG

Forward primer: "Fw-SV40-ER-oh"

TTCTGCTACGAGAACGAGGTGTAAAGACATGATAAGATACAT
TGATGAGTT

Reverse primer:" MscI – HindIII –SV40Rev"

ACATT TGGCCA AAGCTT TACCACATTTGTAGAGGTTTTACTTGC

Reverse primer :"SV40 XhoI rev"

TATTCTCGAGTACCACATTTGTAGAGGTTTTACTT

Forward primer : "fw T2A NpHR"

GACGTGGAAGAAAACCCCGGTCCTATGACAGAGACCCTGCCTCCC

Reverse primer: "rv ecoRI NpHR"

CTCTGAATTCTTTACACCTCGTTCTCGTAGCAGAACACGTTGATGTCGATC
TGGTCC

Forward primer: "ArcL-Sal1-fw"

GGT ACG TCG ACA TGG AGG GAT TCG ACG GTT CAG ATT TTA G

Reverse primer:" ArcL-Hind3-rv"

GGTACT TCGAATCATTTGTATAGT TCA TCC ATG CCA TGT G

2.1.3 Colony PCR and sequencing primer

Forward primer: "fw T7-prom"

AATACGACTCACTATAGGG

Reverse primer: "rev SP6-prom"

CTATAGTGTCACCTAAAT

Forward primer: "M13F"

GTAAAACGACGGCCAG

Reverse primer: "M13R"

CAGGAAACAGCTATGAC

(all cloning primers were ordered from Eurofins Genomics GmbH; colony PCR and sequencing primers were supplied by Eurofins Genomics GmbH or included in the cloning vector kit)

2.1.4. DNA polymerases

PfuUltra II Fusion HS DNA Polymerase(Agilent Technologies GmbH), Phusion DNA Polymerase (New England Biolabs GmbH), T4 DNA Polymerase (New England Biolabs GmbH), Phusion Hot Start DNA Polymerase (Finnzymes, Thermo Fisher Scientific Inc.), Red Taq Kit (VWR International LLC.)

2.1.5. Restriction enzymes

BamHI, NheI, SalI, HindIII, Bgl II, XhoI, MscI, PstI, EcoRI (New England Biolabs GmbH)

2.1.6. Phosphatases

Alkaline phosphatase (rAPid, Rapid DNA Dephos & Ligation Kit, Roche Diagnostics Corp.)

Alkaline phosphatase (Calf Intestinal (CIP), New England Biolabs GmbH)

2.1.7. Gelextraktion

QIAquick Gel Extraction Kit (Qiagen GmbH)

2.1.8. Cloning plasmids

pJet 1.2 - CloneJet PCR Cloning Kit (Thermo Fisher Scientific Inc.)

pCR Blunt II TOPO vector (Life Technologies, Thermo Fisher Scientific Inc.)

2.1.9. Ligation

Rapid DNA Dephos & Ligation Kit (Roche Diagnostics Corp.)

T4 DNA Ligase (New England Biolabs GmbH)

2.1.10. Gel-electrophoresis

Agarose (peqGOLD Universal-Agarose, Peqlab)

Gel Doc 2000 (Biorad Laboratories Inc.)

Ethidium-bromide ([conc.] 800ng/ml; Carl Roth GmbH & Co. KG)

1kb DNA ladder (Invitrogen, Thermo Fisher Scientific Inc.)

Electrophoresis power supply (Biorad Laboratories Inc.)

Horizontal electrophoresis chamber (Biorad Laboratories Inc.)

10x TBE-buffer (0.9M TrisHCl, 0.9M boric acid, 20mM EDTA pH 8.0; Sigma Aldrich Chemie GmbH)

6x loading dye (60% TBE, 18% Ficoll Type 400, 0.12mM EDTA pH8.0, 0.15% bromophenol blue, 0.15% xylencyanol FF; Sigma-Aldrich Chemie GmbH)

2.1.11. Transformation

Chemically competent ß10 E.coli strain

LB (+) Medium (10g Pepton,5g Yeast extract, 5g NaCl, 1g Glucose ad 1l ddH$_2$O, pH 7.2-7.5; Sigma-Aldrich Chemie GmbH)

LB (+) Agar (15g Agar ad 1l LB (+) Medium + selection antibiotic [100µg/ml]: ampicillin or kanamycin; Sigma-Aldrich Chemie GmbH))

2.1.12. DNA amplification at small scale (mini-prep)

Resuspensions buffer (6.06g Tris, 3.72g EDTA ad 1l ddH$_2$O, 100mg RNAse A, pH 8.0; Sigma Aldrich Chemie GmbH)

Lysis buffer (8g NaOH, 100ml 10%SDS ad 1l ddH$_2$O; Sigma Aldrich Chemie GmbH)

Neutralisation buffer (294.5 g CH$_3$COOK ad 1l ddH$_2$O, pH 5.0; Sigma Aldrich Chemie GmbH)

2.1.13. DNA amplification at medium or large scale (maxi-prep)

PureYield Plasmid Midiprep Systems (Promega GmbH)

Genopure Plasmid Maxi Kit (Roche Diagnostics Corp.)

Ultra-centrifuge for cell harvesting (Rotor JA-10; Beckmann Coulter GmbH)

2.2. *AAV* Production

2.2.1. Transfection

HEK293T cells (Leibniz-Institut DSMZ-Deutsche Sammlung von Mikroorganismen und Zellkulturen GmbH)

HBSS (cat. number: 14175-046; Gibco, Thermo Fisher Scientific Inc.)

DMEM (cat. number: 61965-026; Gibco, Thermo Fisher Scientific Inc.)

Cell culture medium: DMEM + GlutaMAXTM-I Medium (+ 4,5 g/l Glucose, - Pyruvate, + 10% FBS (Biochrom), + 1% Penicillin/ Streptomycin (Biochrom))

Petri dishes (150mm, Sarstedt AG &Co.)

$CaCl_2$ (2,5M in ddH_2O) (Sigma Aldrich Chemie GmbH)

Polybrene (Hexadimethrin Bromid in ddH_2O) (8 mg/ ml) (Sigma Aldrich Chemie GmbH)

Dextran 500 *from Leuconostoc spp.* (10 mg/ml) (Sigma Aldrich Chemie GmbH)

pAdDeltaF6 ([29]), *pAAV2/8Y733F* (Koch et al., 2012), amounts (x) used for transfection:

$$x = \frac{(270\mu g * molecular\ weight\ of\ helper\ plasmid\ or\ packaging\ plasmid)}{molecular\ weight\ of\ vector\ plasmid}$$

2x BBS (4.26g BES, 6.54g NaCl, 0.085g $Na_2H PO_4$ ad 400ml ddH_2O , pH 6.95; Sigma Aldrich Chemie GmbH, Carl Roth GmbH & Co. KG)

2.2.2. Cell harvest

Ultra-centrifuge for cell harvesting (Rotor JA-10; Beckmann Coulter GmbH)

Lysis buffer (150mM NaCl, 50mM TrisHCl pH 8.5; sterile filtered; Sigma Aldrich Chemie GmbH)

Cell scraper (VWR International GmbH)

2.2.3. Density gradient centrifugation

Benzonase nuclease, [conc.] 50U/ml (cat.number: 1.01695.0001; VWR International GmbH)

Iodixanol (Opitprep, cat. number 1114542; Progen Biotechnik GmbH)

15% Iodixanol gradient solution (1mM $MgCl_2$, 2.5mM KCl, 1M NaCl, 12.5ml Opitprep 0.00075% phenol red, 5ml 10xPBS ad 50ml with ddH_2O)

25% Iodixanol gradient solution (1mM $MgCl_2$, 2.5mM KCl, 20.9ml Opitprep 0.001% phenol red, 5ml 10xPBS ad 50ml with ddH_2O)

40% Iodixanol gradient solution (1mM $MgCl_2$, 2.5mM KCl, 1M NaCl, 33.3ml Opitprep, 5ml 10xPBS ad 50ml with ddH_2O)

60% Iodixanol gradient solution (1mM $MgCl_2$, 2.5mM KCl, 0.00025% phenol red ,50ml Opitprep)

Ultra-centrifuge for density gradient (Sorvall Discovery 90, Rotor 70 Ti; Thermo Fisher Scientific Inc.)

2.2.4. Ion exchange chromatopraphy

Ion exchange chromatography (ÄKTAprime plus system; GE Healthcare GmbH)

Ion exchange column (5 ml HiTrap Q HP column; GE Healthcare GmbH)

Ion exchange Buffer A (20mM Tris, 15mM NaCl ad 500ml with ddH_2O; pH 8.5)

2.2.5. Size exclusion centrifugation

Centrifugation filter (Amicon Ultra-4, 100kDa; Merck Millipore, Merck Chemicals GmbH)

PBS-MK (10% PBS (10x), 1mM MgCl2, 2.5mM KCl, sterile filtered; Sigma Aldrich Chemie GmbH)

Centrifuge (Rotor J2-MC; Beckmann Coulter GmbH)

2.3. Immunohistochemistry

Heparin (Meditech Vertriebs GmbH)

Tris-HCl-buffer (pH 7.66, 0.05M: 12.2g Tris, 75ml HCl (1M) ad 2l ddH_2O ; Sigma Aldrich Chemie GmbH)

PBS (0.1M, pH 7.4: 137mM NaCl, 2.7mM KCl , 1.47mM KH_2PO_4, 4.3mM $Na_2HPOx2H_2O$ ad 1l ddH_2O; Sigma Aldrich Chemie GmbH)

Peristaltic pump (Reglo, Ismatec GmbH)

Blocking Solution (1% bovine serum albumin, 0.1% Saponin, 1-0.3% Triton X-100 in 0.1M PBS; Sigma Aldrich Chemie GmbH)

Vibratome (VT1200S, Leica Mikrosysteme Vertrieb GmbH)

Anti-MAP-2 antibody, IgY, Host: Chicken, used [c] 1:5000 (cat. number: CH22103; Neuromics)

Anti-*NeuN*-antibody, IgG_1, Host: Mouse, clone: A60, used [c] 1:1000 (cat.numner: MAB377; Merck Millipore, Merck Chemicals GmbH)

Anti -S100ß-antibody, IgG, Host: Rabbit, used [c] 1:500, (cat. Number: 37A; SWANT)

2.4. Stereotactic Injection

Vertical glass electrode puller (PE-2, Narishige Ltd.)

XYZ- axis controller (SM-5, Luigs & Neumann Feinmechanik & Elektrotechnik GmbH)

Micro manipulator (Junior XYZ-R, Luigs & Neumann Feinmechanik & Elektrotechnik GmbH)

Custom-built stereotaxic frame (Schuller G.)

Custom-built heating pad

Micro injector (Nanoliter 2000, World Precision Instruments Inc.)

Glass capillaries (ID = 0.530 mm ± 25 µm, OD 1.14 mm, Item#: 4878, World Precision Instruments Inc.)

Dental Cement (Harvard Dental International GmbH)

Electric shaver (Exacta, Aesculap Suhl GmbH)

Suture material (Suprama HS18 USP 4/0, Feuerstein GmbH)

Binocular/stereo-microscope (GmbH SOM 62, Karl Kaps GmbH)

Mineral oil (World Precision Instruments Inc.)

2.5. Electrophysiology

2.5.1. *In vitro* recordings

Microscope (BX51WI, Olympus Europa SE & CO. KG)

4x and 60x Objectives (Plan N 4x/0.10 and LUMPlanFL N 60x/1.00 W, Olympus Europa SE & CO. KG)

Infrared lamp (TH4-200, Olympus Europa SE & CO. KG)

Condensor (Aplanat Achromat 1.4NA Oil condensor, Olympus Europa SE & CO. KG)

Fluorescence lamp (LQ-HXP-120-3, LEJ GmBH)

LED controller, LED Yellow, LED Blue (KSL Duo ,KSL 083 590nm-LED, KSL 010 470nm-LED, Rapp OptoElectronics GmbH)

Peristaltic pump (Reglo, Ismatec GmbH)

Patch amplifier (triple patch clamp EPC 10, HEKA Elektronik Dr. Schulze GmbH)

Camera and camera controller (Orca R2 camera, C10600, Hamamatsu Photonics K.K)

Temperature controller (Dual Automatic Temperature Controller TC-344B, Warner Instruments LLC)

Micromanipulator (Patchstar, Scientifica Ltd.)

Vibratome (VT1000S and VT1200S, Leica Mikrosysteme Vertrieb GmbH)

Water bath (BWT-U heated, bioSan GmbH)

Electrode puller (DMZ Universal Puller, Zeitz Instruments GmbH)

Light power meter and spectrometer console (PM100D, Thorlabs Inc.)

Solutions

ACSF slice solution:

50mM sucrose, 25mM NaCl, 25mM $NaHCO_3$, 2.5mM KCl, 1.25mM NaH2PO$_4$, 3mM $MgCl_2$, 0.1mM $CaCl_2$, 16mM glucose, 0.4mM ascorbic acid, 3mM myo-inositol and 2mM Na-pyruvate (Sigma-Aldrich Chemie GmbH)

ACSF external recording solution:

25mM $NaHCO_3$, 2.5mM KCl, 1.25mM NaH2PO$_4$, 125mM NaCl, 16mM glucose, 0.4mM ascorbic acid, 3mM myo-inositol, 2mM Na-pyruvate, 2 mM $CaCl_2$, and 1mM $MgCl_2$ (Sigma-Aldrich Chemie GmbH)

Internal recording solution (current clamp):

145mM K-gluconate, 5mM KCl, 15mM HEPES, 2mM Mg-ATP, 2mM K-ATP, 0.3mM Na_2-GTP, 7.5mM Na_2-phosphocreatine, and 5mM K-EGTA (Sigma-Aldrich Chemie GmbH)

Internal recording solution (voltage clamp):

105mM Cs-gluconate, 26.7mM CsCl, 10mM HEPES, 20mM TEA-Cl, 5mM Cs-EGTA, 3.3mM $MgCl_2$, 2mM Na_2-ATP, 0.3mM Na_2-GTP and 3mM Na_2-phosphocreatine (Sigma-Aldrich Chemie GmbH)

2.5.2. *In vivo* recordings

I/O Processor (RZ6 Multi I/O Processor, Tucker Davis Technologies)

Amplifier (EPC10/ USB , HEKA Elektronik Dr. Schulze GmbH)

Noise eliminator (Humbug, Quest Scientific Instruments Inc.)

Earphones (ER-4PT, Etymotic Research Inc.)

Micro manipulator (IVM single axis manipulator, Scientifica Ltd)

Syringe Pump (801, Univentor Ltd.)

LED Driver (4 Channel LED Driver (DC4104) + Single LED Connector Hub (DC4100HUB), Thorlabs Inc.)

LED Blue, LED Orange (FibreCoupled HighPower LED, Blue (470 nm) M470F1, Orange (617 nm) M617F1, SMA, 1000 mA, Thorlabs Inc.)

Ferrule connector (Ceramic Split Mating Sleeve for Ø2.5 mm Ferrules (ADAF1), Thorlabs Inc.)

Optical fibre (Rotating Patch Cable, SMA to FC/SC, Ø200 µm, 0.39 NA (RJPS2), Thorlabs Inc.)

Optical fibre (Multimode Optical Fibre, 0.39 NA, Ø200 µm Core, HighOH (FT200UMT), Thorlabs Inc.)

Ceramic ferrule (FC/SC Ceramic Ferrule, Ø2.5 mm Multimode Ø230 µm Hole Size (CF23010))

Glue (epoxy glue for Fibre Optic Connectors, Fast Room Temperature Cure (F120), Thorlabs Inc.)

Custom –made stereotaxic frame

Direct current injector (Stimulus Isolator A360, World Precision Instruments Inc.)

Glass capillaries (Harvard Apparatus Inc.)

Condenser microphone (Bruel& Kjær Type 4138)

Measuring amplifier (Bruel& Kjær Type 2636)

2.6. Drugs (*in vitro*, *in vivo* and surgeries)

DNQX (BioTrend Chemikalien GmbH), used [c] 20µM

D-APV (BioTrend Chemikalien GmbH), used [c] 50µM

Meloxicam (Metacam, 5mg/ml, Boerhinger Ingelheim), used [c] 10mg/kg body mass

Medetomidin (Domitor, Pfizer Inc.), used [c] 0.15mg/kg body mass

Midazolam (Midazolam, Ratiopharm GmbH), used [c] 7.5mg/kg body mass

Fentanyl (Fentanyl, Janssen Pharmaceutica), used [c] 0.03 mg/kg body mass

Pentobarbital (Narcoren, 16g/100ml, Merial GmbH) used [c] 2 mg/kg body mass

Isofluran (IsoFlo, Abbot Laboratories)

Ringer infusion (B.Braun Melsungen AG)

Atipamezol (Antisedan, Orion Pharma), used [c] 0.4µg/kg body mass

Flumazenil (Anexate, Roche Pharma AG), used [c] 0.4µg/kg body mass

Naloxon (Naloxon, Hameln Pharma Plus GmbH), used [c] 0.5µg/kg body mass

Ketamine chloride (20 mg/ml, Ketavet, Zoetis Deutschland GmbH)

Xylazine chloride (0.8 mg/ml, Rompun, Bayer HealthCare AG)

Ketamin/Rompun mixture 0.5ml/100g body mass

2.7. Imaging & Microscopy

TCS SP5-2 confocal laser scanning microscope (Leica Mikrosysteme Vertrieb GmbH)

63x objective (HCX PL APO lambda blue 63.0x1.40 OIL UV oil, Leica Mikrosysteme Vertrieb GmbH)

20x objective (HCX PL APO CS 20.0x0.70 IMM UV oil, Leica Mikrosysteme Vertrieb GmbH)

Diodelaser 405 nm kpl Coherent (25 mW)

Argon Laser (458 nm, 476 nm, 488 nm, 514 nm)

DPSS Laser kpl 561 nm MG (10 mW)

HeNe Laser 594 nm, Uniphase (2.5 mW)

HeNe Laser 633 nm, Uniphase (10 mW)

Vectashield H-1200, Vectashield H-1000 mounting medium (VECTOR LABORATORIES INC.)

Virtual Slide Microscope (VS120 S1, BX61VST; Olympus Europa SE & CO. KG)

10x objective (UPLSAPO 10x; Olympus Europa SE & CO. KG)

2.8. Software

Patchmaster v2x69 (HEKA Elektronik Dr. Schulze GmbH)

Igor Pro 6.35A (Wavemetrics) with Patchers Power Tools 2.19

FIJI, Biovoxxel extensions (Jan Brocher), Bio-Formats extension (LOCI), Cell Counter Plugin (Kurt de Vos)

Graphpad Prism 5 (Graphpad Software)

SigmaPlot 11.0 (Systat Software)

Jan Schnupp's Brainware 9.1 (Tucker Davies Technologies Inc.)

Matlab R2014a (The MathWorks Corp.)

Office 2007 (Microsoft Corp.)

CLC Sequence Viewer (CLC Bio, Qiagen GmbH)

Illustrator (Adobe Systems Corp.)

OlyVia (Olympus Europa SE & CO. KG)

2.9. *pAAV* Maps

2.9.1 Control fluorophors

pAAV2.1-ss-hSyn-EYFP-WPRE
5372bp

pUC ori · L-ITR · hSyn · EYFP · WPRE · hGH polyA · R-ITR · f1 Origin · AmpR

pAAV2.1-ss-hSyn-GFP-WPRE
5262bp

pUC ori · L-ITR · hSyn · GFP · WPRE · hGH polyA · R-ITR · f1 Origin · AmpR
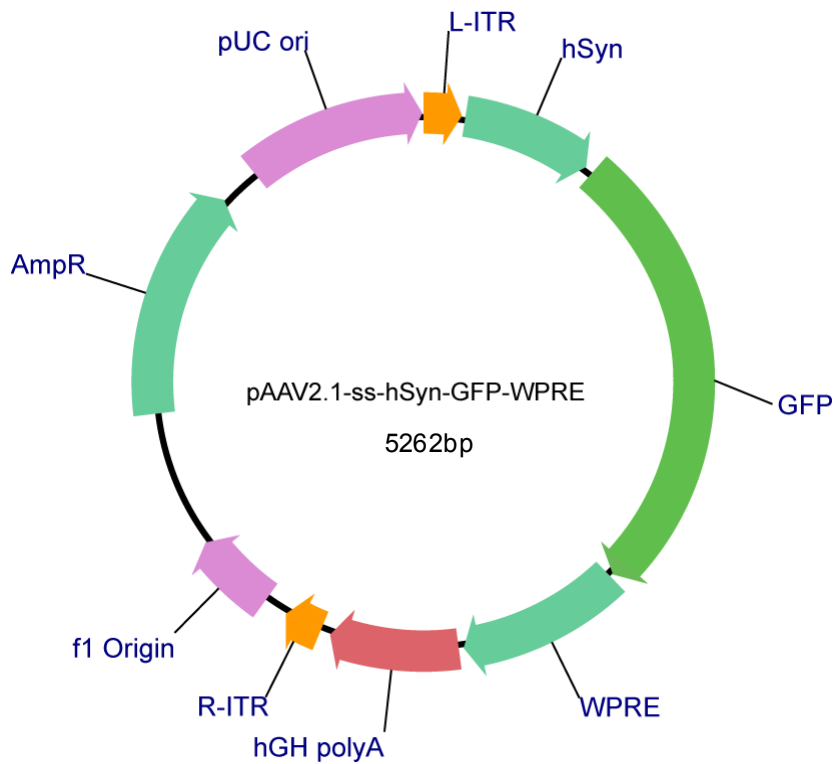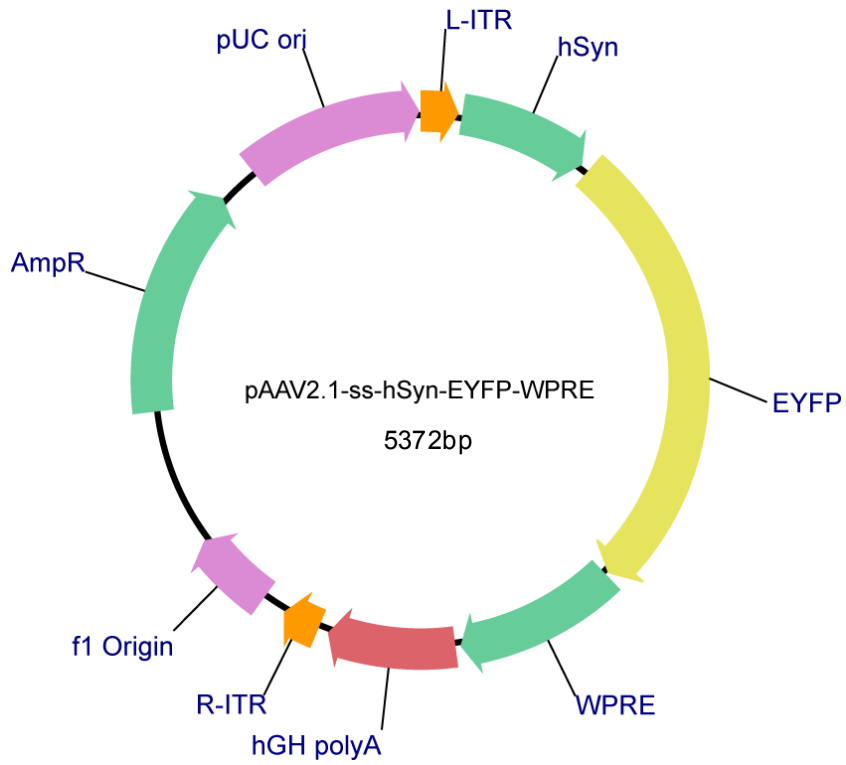
2.9.2. Tools for excitation

pUC ori
L-ITR
hSyn
AmpR
CatCH
pAAV2.1-ss-hSyn-CatCH-mcherry-WPRE
6197bp
mCherry
f1 Origin
R-ITR
hGH polyA
WPRE

pUC ori
L-ITR
hSyn
AmpR
ChETA
pAAV2.1-ss-hSyn-ChETA-mcherry-WPRE
6197bp
mCherry
f1 Origin
R-ITR
hGH polyA
WPRE
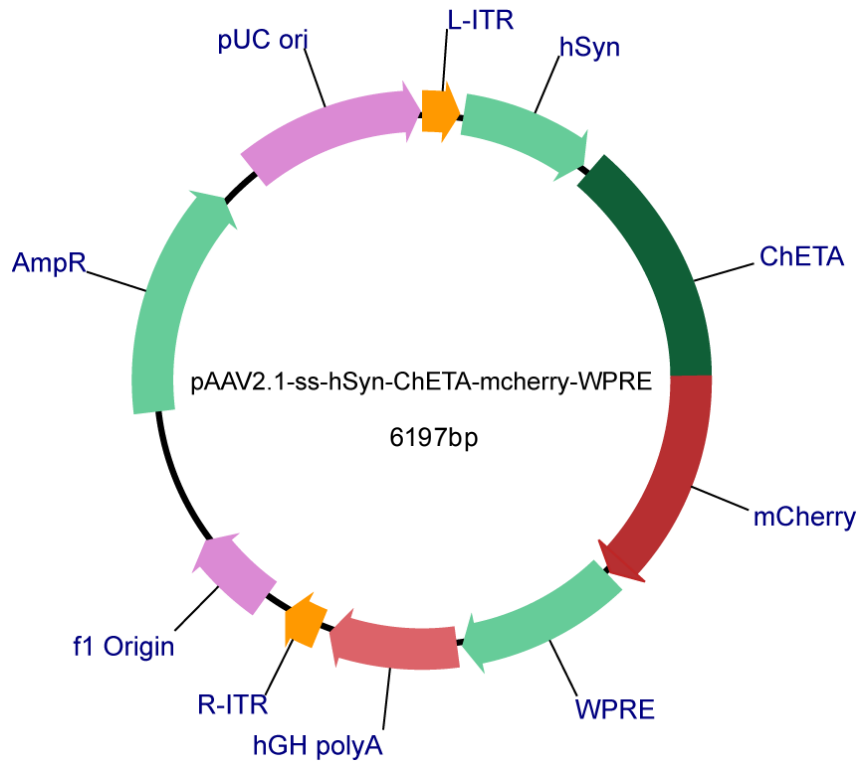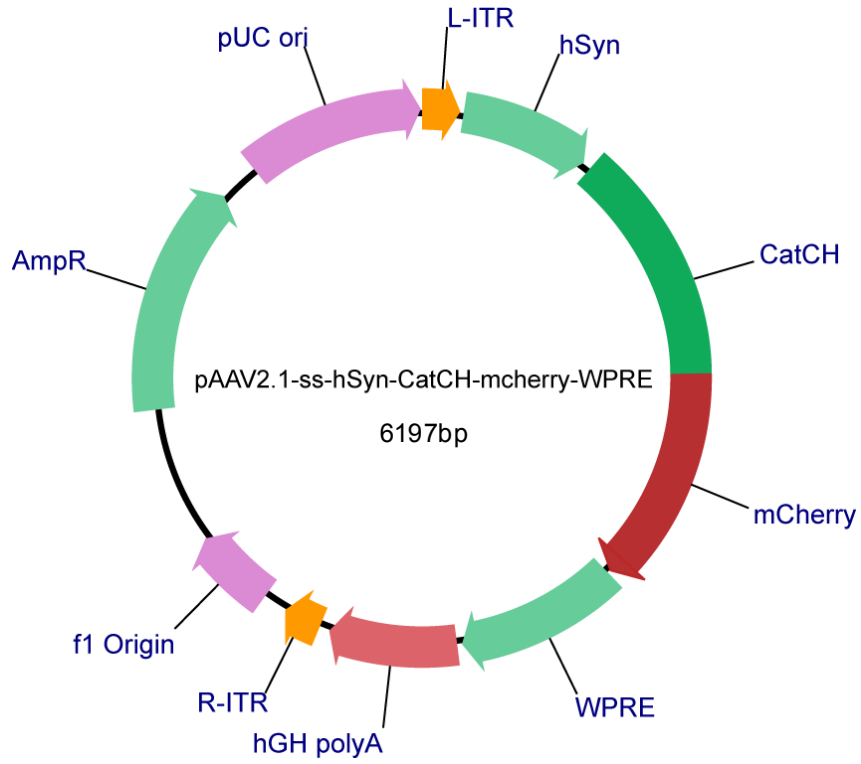
2.9.3. Tools for inhibition
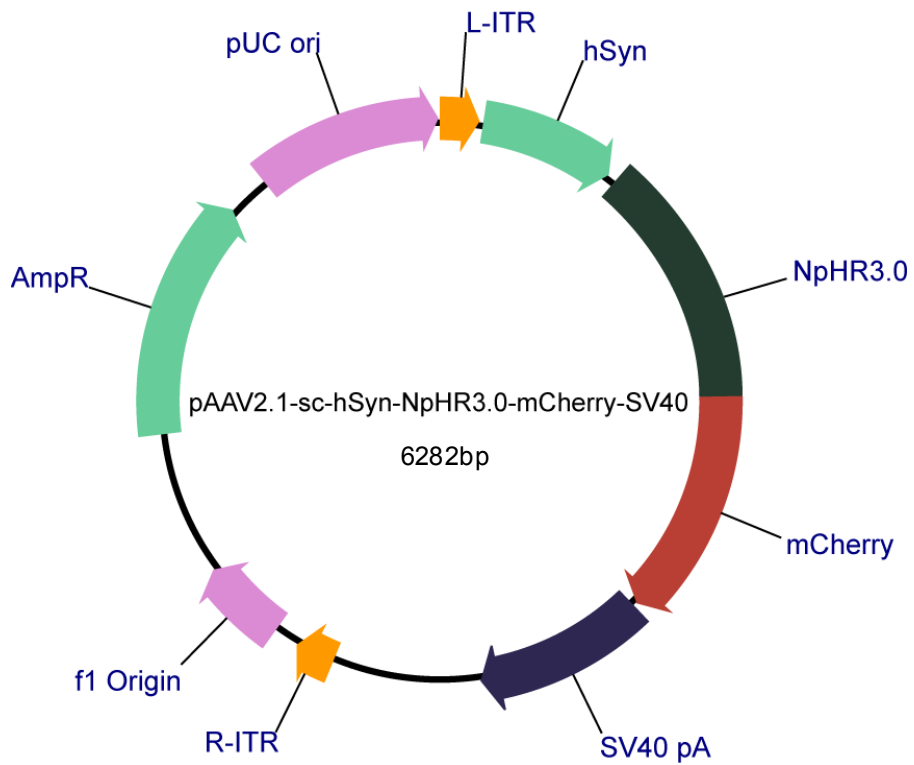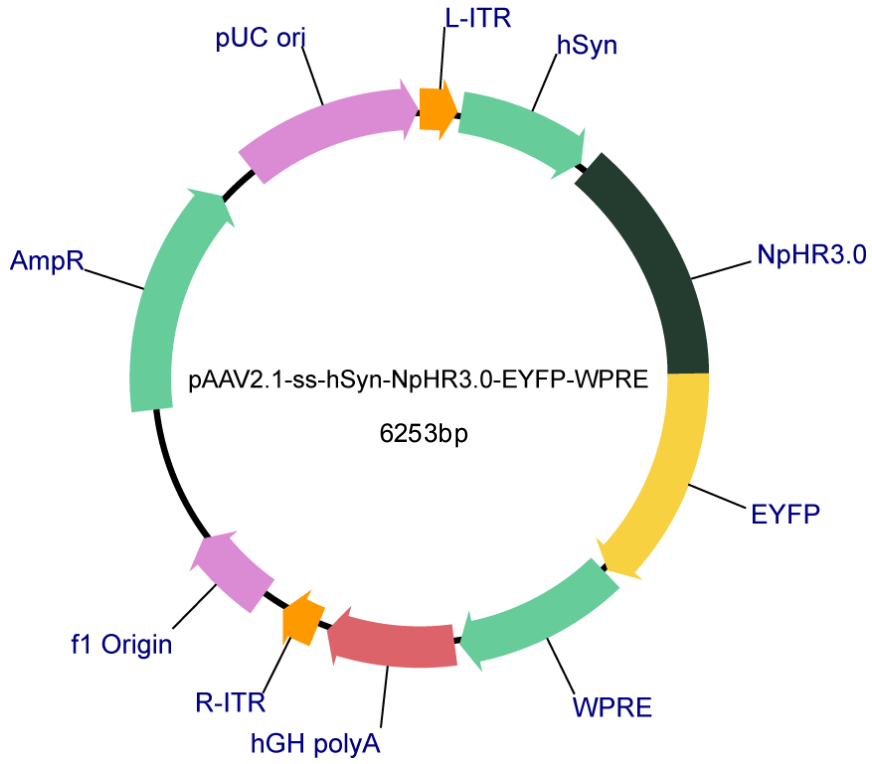
2.9.4. Tools for simultaneous excitation and inhibition
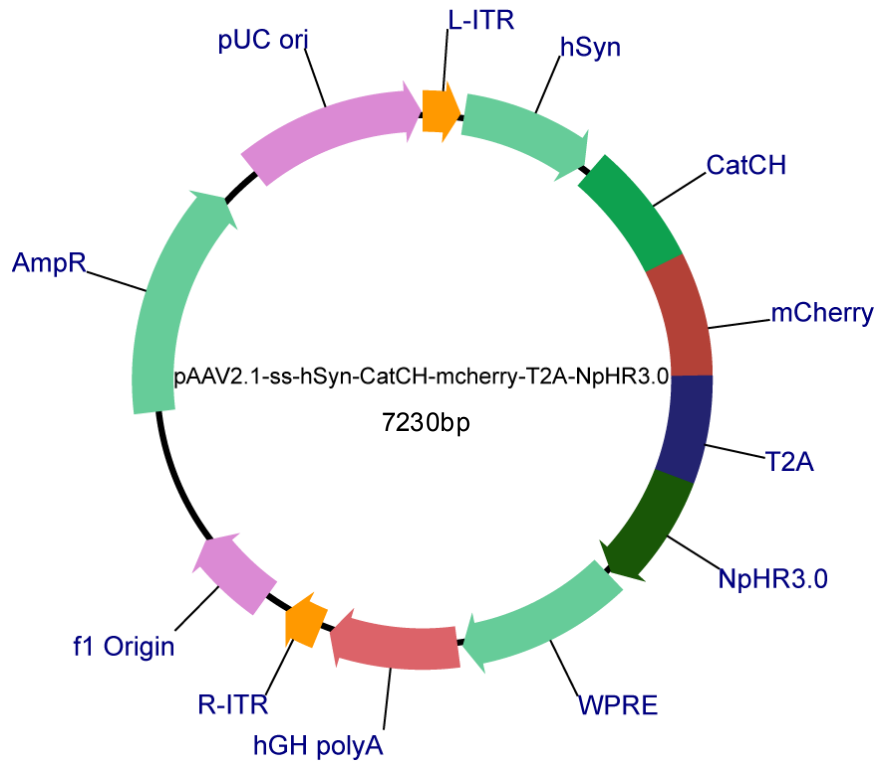
2.9.5. Voltage sensor
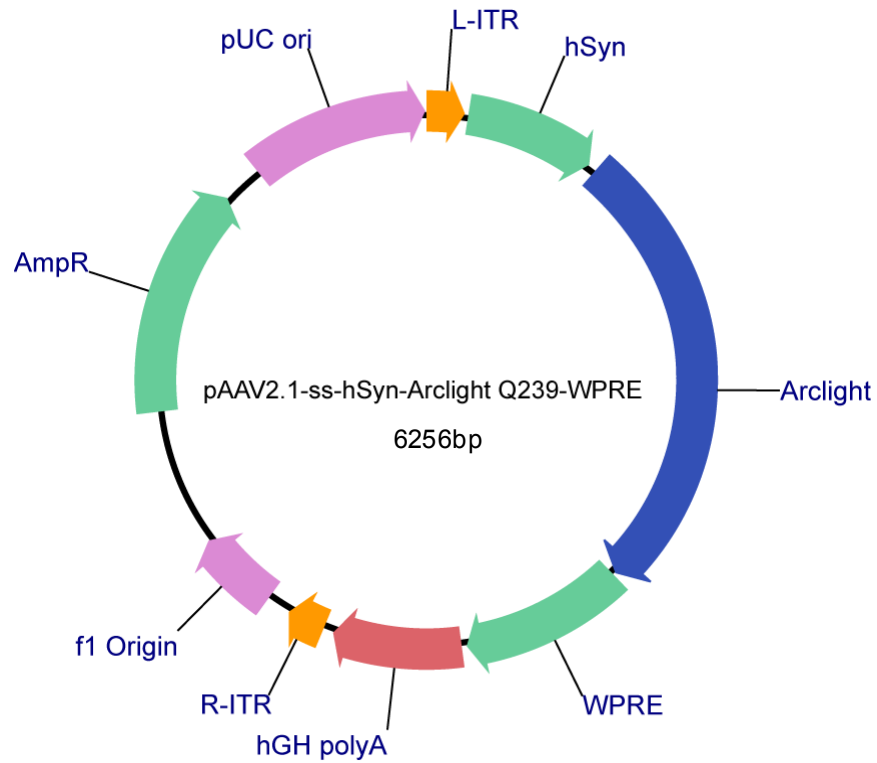
3. Methods

3.1. Molecular Cloning

3.1.1. Polymerase Chain Reaction (PCR)

All primers – except for fusion PCR - were designed to have a melting temperature (Tm) between 50 - 60°C. If restriction-sites on the 5`end were included three to four nucleotides were added to the 5´end of the respective primer. Primers were used at a final concentration of 0.2µM. Deoxynucleotides (dNTPs) were used at a concentration of 200µM. The amount of template-DNA was varying between 0.1 and 10ng. Buffer concentrations were used according to manufacturers'recommendation and occasionally supplemented with additional $MgCl_2$ (final conc. 2.5-5mM) and DSMO (2% v/v) for GC-rich conditions (e.g. hSyn-promoter template). All reactions were carried out in a final volume of 50µl and with Hot-Start DNA polymerases involving a 95°C activation step at the beginning.

95°C	2 min	
95°C	30 sec.	
50-60°C	30 sec.	35-40x
72°C	X (1000nt*min)	
72°C	10 min	
10°C	∞	

Table 1: Scheme for typical PCR programme

3.1.2. Fusion PCR

All fusion primers (f-primers) were designed to have a high Tm of 69-70°C. The annealing temperature of the overlapping sequences was designed to match 59-62°C.
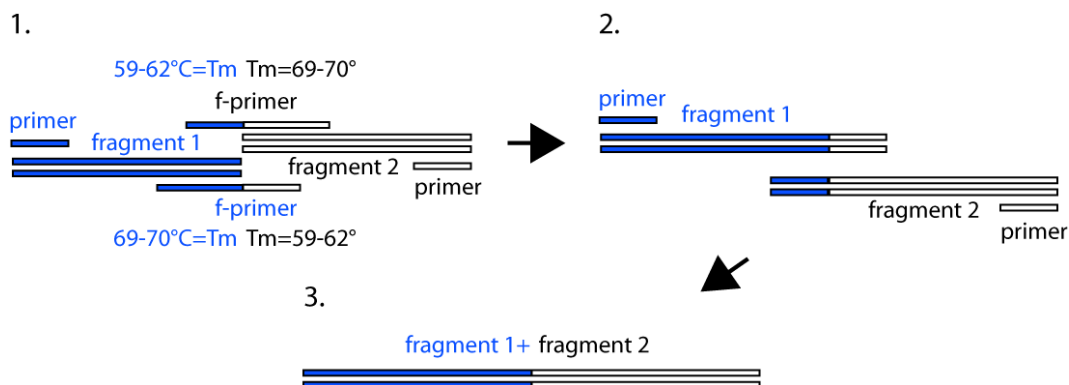
Figure 13: Scheme for Fusion PCR

The overlapping part of the fusion primer (f-primer) was designed to hybridise up to 59-62°C whereas the melting temperature for the non-overlapping part was aimed at 69-70°C. In the first PCR reactions fragments with overlapping end(s) had to be amplified (1.) and these amplified fragments were then fused in a subsequent reaction (2.) which yielded the fusion-product (3.). The design as depicted here was used to fuse up to four fragments in consecutive reactions.

Primers were used at a final concentration of 0.2-1µM. Deoxynucleotides (dNTPs) were used at a concentration of 400µM. The amount of template DNA was varying between 0.1 and 1ng. Buffer concentrations were used according to manufacturer's recommendation and occasionally supplemented with additional $MgCl_2$ (final conc. 2.5-5mM) and DSMO (5% v/v) for GC-rich conditions. All reactions were carried out in a final volume of 50µl and with Hot-Start DNA polymerases involving a 95°C activation step at the beginning. To increase the yield of the fusion product a lower annealing temperature was used in the first five rounds of the fusion PCR.

95°C	2 min	
95°C	30 sec.	
50-60°C	30 sec.	5x
72°C	X (1000nt*min)	
95°C	30 sec.	
65-70°C	30 sec.	40x
72°C	X (1000nt*min)	
72°C	10 min	
10°C	∞	

Table 2: Scheme for typical Fusion PCR programme

3.1.3. Colony PCR

E.coli colonies from selective agar plates were each picked with a 10µl-tip and transferred into a PCR tube – one tube for each colony. Thereby the colonies served as DNA template. Primers used for amplification of the insert were standard primers complementary to the flanking sites on the cloning vector, namely T7 promoter and SP6 promoter. Primers were used at a final concentration of 0.2µM. Deoxynucleotides (dNTPs) were used at a concentration of 200µM. Buffer concentrations were used according to manufacturer's recommendation. All reactions were carried out in a final volume of 20µl.

95°C	2 min	
95°C	30 sec.	
50°C	30 sec.	35x
72°C	X (1000nt*min)	
72°C	10 min	
10°C	∞	

Table 3: Scheme for typical Colony PCR programme

3.1.4. Gel electrophoresis

According to DNA fragment size the agarose content of the gel was varied: for fragments smaller than 500bp 2% agarose gels were prepared, otherwise 1% agarose gels and for fragments larger than 1200bp 0.7% agarose gels were used. Agarose was diluted in 1x TBE, boiled in a microwave and after cooling down to 40-50°C ethidium-bromide at a concentration of 800ng/ml was added to the gel to visualize the DNA. Subsequently the agarose gel was poured into horizontal chambers and after hardening transferred into the plotting device and submerged in 1xTBE. Samples were mixed with loading dye (6x) and loaded onto the gel alongside with an aliquot of a 1kB DNA-ladder for size comparison. Direct current of 100-150V was applied until the DNA samples were separated with sufficient resolution. The agarose gel was removed from the plotting chamber and put into the Gel Doc apparatus. DNA bands were visualized with UV light and photographed.

3.1.5. Gel-elution

With the help of UV light, DNA was visualized in the Gel Doc apparatus and DNA bands of anticipated size were cut out from the agarose gel. The cut out agarose gel was weighed, transferred into a 2 ml tube and QG-buffer was added (3x volumes of QG-buffer per 1x volume agarose gel). After 10-15 min at 50°C the agarose gel was completely dissolved in QG-buffer. 1x volume of isopropanol was added and the sample gently mixed. Up to 800µl of the sample were then transferred onto the QIAquick spin-columns and centrifuged for one minute at ~13000rpm. Flow-through was discarded, columns loaded with 0.75ml PE-buffer and centrifuged one minute at ~13000pm as a washing step. Flow-through was discarded and the columns were dried with an additional centrifugation step for one minute at 13000rpm. To elute bound DNA 30-50µl elution-buffer or ddH$_2$O was applied to the column and after one minute incubation columns were centrifuged again for one minute at 13000rpm. The thereby eluted DNA was collected in a 1.5 ml tube.

3.1.6. DNA dephosphorylation and ligation

According to the manufacturer's protocol up to 1µg DNA was mixed with 0.5µl phosphatase and 1µl of buffer (10x) and ddH$_2$O added to a final volume of 10µl. The mixture was incubated for 10-30min. at 37°C. For further use of the now dephosphorylated DNA samples, the phosphatase was inactivated by a heating step to 75°C for 2 min or the DNA samples were purified via gel electrophoresis if the phosphatase was not heat-inactivatable.

To ligate inserts into vectors a surplus of insert DNA (75-100ng) was mixed with vector DNA (25ng), 1µl DNA Dilution buffer(5x), 5µl T4 DNA Ligation buffer(2x), 0.5µl T4 DNA ligase and diluted with ddH$_2$O to a final volume of 10µl. The ligation mixture was then incubated for 10-30 min. at room temperature and an aliquot of 3-5µl used directly for transformation or stored at -20°C until further use.

3.1.7. DNA digestion

Up to 5µg of DNA was mixed with 5µl of the appropriate restriction buffer (see manufacturer's recommendations for details), 0.5µl enzyme and ddH$_2$O was added to a final volume of 50µl. The digestion mixture was incubated for 60 min. at 37°C and afterwards an aliquot of 30 µl was loaded onto an agarose gel for separation of DNA fragments and for purification from enzymes.

3.1.8. DNA blunting

In order to generate blunt ends from sticky ends the DNA sample was mixed with 0.5µl T4 DNA Polymerase, 200µM Deoxynucleotides (dNTPs) and 2µl T4 DNA Ligase buffer (10x) and filled up with ddH$_2$O to a final volume of 20µl. The mixture was incubated for 15min at 12°C, afterwards the reaction stopped by adding EDTA to a concentration of 10mM and a heating step to 75°C for 20 min. The DNA sample was then purified via gel electrophoresis.

3.1.9. Transformation

100µl of chemically competent E.coli were slowly thawed on ice and once liquid an aliquot (3-5µl) from the ligation mixture was added, gently mixed and incubated for ten min. on ice. A heat shock at 42°C for 30 sec. was delivered to the E.coli by placing them in the water bath. Afterwards E.coli were again incubated on ice for two more min. before distributing 50µl per plate on selective agar. The plates were incubated over night at 37°C. Colonies from plates were then picked and used for colony PCR or mini-prep. For intermediate storage plates were kept at 4°C.

3.1.10. Plasmid preparation I (Mini-prep)

Individual E.coli colonies from selective agar plates were carefully picked with the help of a pipette tip and each transferred into a vial with 5ml liquid selection medium. These liquid cultures were incubated overnight at 37°C and constantly shaken at 225 rpm. Via centrifugation for 10 min. at 1000 x g and 4°C cells were concentrated at the bottom of the vial whereas supernatant was discarded. Cells were diluted with 250µl resuspension buffer and then transferred into a 2ml tube. Addition of 250µl lysis buffer and carefully mixing was followed by addition of 250µl neutralization buffer after a maximum of 5 min. incubation. After another 5 min. tubes were centrifuged for 15 min. at 1000 x g and 4°C. The supernatant was transferred into a fresh 1.5 ml tube. In order to precipitate the DNA 525µl isopropanol was added. The mixture was centrifuged for 15 min. at 1000 x g and 4°C. Supernatant was carefully discarded without spilling the DNA-pellet. A washing step included addition of 750µl ethanol (70%) and centrifugation for 15 min. at 1000 x g and 4°C. Supernatant was discarded and remainders were evaporated in a vacuum centrifuge. The DNA pellet was dissolved with 30-50µl ddH$_2$O. Plasmids with

correct inserts were identified with restriction analysis and subsequently sent for sequencing. (c.f. Results Chapter)

3.1.11. Plasmid preparation II (Maxi-prep)

Once the restriction analysis and the read for a plasmid turned out positive, 100ml of liquid selection medium was inoculated with the positive *E.coli* clone. After incubation at 225rpm at 37°C over night the culture is transferred into two 50ml falcons and centrifuged at 4000 x g and 4°C for 10 min. Supernatant was discarded and cells were diluted with 12ml resuspension buffer and transferred into a fresh falcon. Cells were gently mixed with 12ml lysis buffer and incubated for 3 min. at room temperature. After addition of ice cold 12ml neutralization buffer and gently inverting the falcon tube, the mixture was incubated on ice for 5 min. Centrifugation at 5000 x g and 4°C for 10 min. followed. The supernatant was then applied onto the preequilibrated column. Flow-through was discarded, 16 ml wash buffer was loaded onto the column and the washing step was repeated one time. Once the column ran dry, 15ml of elution buffer was applied and flow-through collected in a fresh falcon. DNA was precipitated by addition of 11ml isopropanol and centrifugation at 5000 x g and 4°C for 60-90 min. Supernatant was gently removed and the DNA pellet washed with 4ml ethanol (70%) and centrifuged again at 5000 x g and 4°C for 20 min. Supernatant was removed and the DNA pellet was dried for 10-30 min. and redissolved in 500µl ddH$_2$O.

3.1.12. Sequencing

DNA samples were diluted to a concentration of 50-100ng/µl in a volume of 15µl. These DNA samples were sent to Eurofins Genomics GmbH and the PCR inserts sequenced.

3.2. *AAV*-Production

3.2.1. Transfection (calcium-phosphate method)
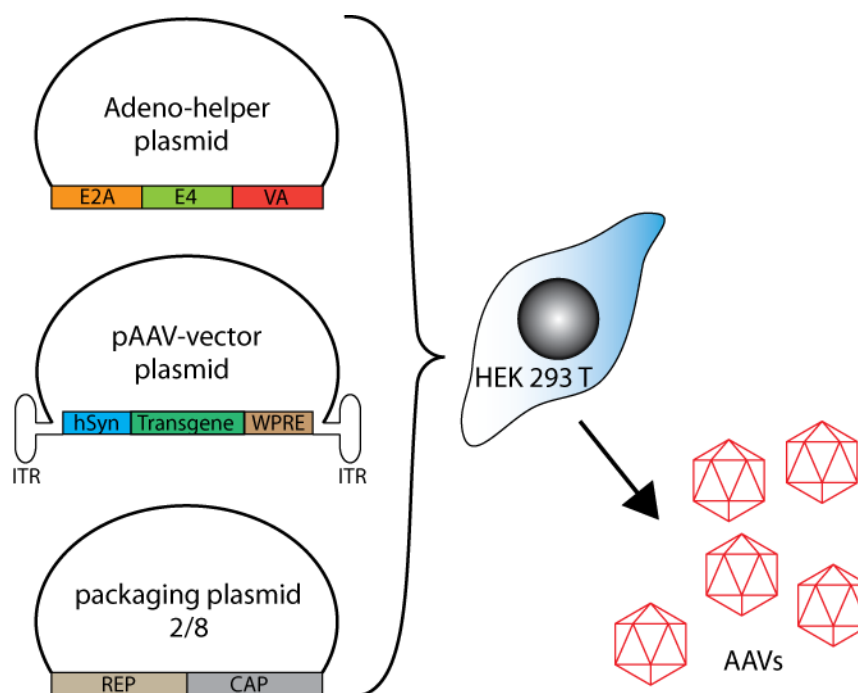
Figure 14: Schematic for *AAV* production

HEK293T cells were transfected with three plasmids in order to produce complete AAV particles: Adeno-helper plasmid comprising genes important for replication of ss-DNA, the packaging plasmid comprising genes for capsid proteins and replication and the actual vector plasmid with the promoter sequence, transgenes (ChRs and/or fluorophores), expression enhancers (WPRE or SV40-pA) and the flanking inverted terminal repeats (ITR). Virions were purified from the cells after assembly inside the cell.

15 plates with HEK293T cells were incubated with 10% CO_2 at 37°C until 70-80% confluency was achieved. Two hours before transfection started cell culture medium was replaced with fresh medium. The transfection reagent included three plasmids namely the vector plasmid/construct (including ITRs flanking the expression cassette based on *AAV*2 backbone: hSyn-promoter, transgenes, regulatory elements), the pAdhelper (the adeno-helper plasmid including adenoviral genes E2A, E4 and VA) and the packaging plasmid (containing rep and cap genes for appropriate serotype). 270µg of vector plasmid DNA, (x) µg pAdhelper and (x) µg *pAAV2/8Y733F* (c.f. material section for calculation of x) were mixed with 17.5µl Polybrene, 1.75ml Dextran filled up to 15.75 ml with ddH_2O and only at the very last 1.75ml $CaCl_2$ was added. After gently mixing 17.5ml 2xBBS were added dropwise and gently mixed again. After 10 min. 2.3ml of transfection reagent was pipetted evenly onto each plate.

The cells were incubated with 3-5% CO_2 at 37°C over night. The following day medium was exchanged and cells were incubated with 10% CO_2 at 37°C over night

3.2.2. Cell harvest

Cells were detached with a cell scraper and transferred into a sterile flask. The cells were centrifuged at 3000 x g and 4°C for 15 min. Supernatant was discarded and cell pellet resuspended in 7.5ml lysis buffer, three times frozen in liquid nitrogen and thawed again in 37°C. Cells were put to -80°C after freezing the third time in liquid nitrogen.

3.2.3. Density gradient centrifugation (iodixanol gradient)

Cells were thawed, mixed with benzoase (50U/ml) and incubated for 30 min. at 37°C in the water bath. Centrifugation at 3700 x g and 4°C for 25 min. was followed by transfer of the supernatant into a falcon. 8ml 15% iodixanol, 5ml 25% iodixanol, 5ml 40% iodixanol and 8ml 60% iodixanol was gently folded in the supernatant. The falcon was then ultra-centrifuged at 70000 rpm and 18°C for 105 min. Density phases could be clearly distinguished due to their different color. The 40% iodixanol phase was recovered with a needle and syringe by piercing through the falcon. The needle was approximately placed in the interphase of the 40-60% phase and the 40% phase aspirated until coming close to the 25% phase. The aspirated 40% fraction was stored at -80°C for further purification.

3.2.4. Ion exchange chromatography

For further concentration, ion exchange chromatography was performed. The column was equilibrated with approximately 25 ml of buffer A. Then the virus phase from the density gradient centrifugation was diluted 1:1 with buffer A and loaded onto the column via injection loop at a constant flow rate (1ml/min). Once the detector measured an UV-absorption of about 2800mAU and a conductivity of 16mS/AU, fractions were collected. After the conductivity started to decline, 2.5M NaCl were used to elute the bound molecules. All fractions showing at least 16mS/AU were pooled and stored at -20°C for further purification.

3.2.5. Centrifugal ultra-filtration (Amicon™)

An 4 ml aliquot of the pooled virus fraction from ion exchange chromatography was transferred into the filtration falcon and centrifuged at 4000 rpm and 20°C for 15 min. The flow-through was discarded and the previous steps repeated until the complete virus volume was transferred. A washing step included rinsing the filter membrane with 1ml of 0.014/Tween/PBS-MK and centrifugation at 4000rpm and 20°C for 15 min. Centrifugation was continued in short steps and flow-through discarded until a remainder of 100-150µl was left, which was then aliquoted in 10µl samples and stored at -80°C. Before *AAV* samples were used for injection, concentration (gc/µl) was determined by qPCR (see below).

3.2.6. Determination of *rAAV* genomic titer

Quantification of *rAAV* genomic titer was done via quantitative PCR (qPCR) using primers directed against the WPRE sequence and carried out by Fred Koch and colleagues in the laboratory of Dr. Stylianos Michalakis (Ludwig-Maximilians-University Munich, Department of Pharmacy).

3.3. Animal rearing and license

Animals (*Meriones unguiculatus*) were reared in parental pairs together with their most recent litter and kept in cages with enriched environment. A light and dark rhythm of 12 hours was maintained in the animal breeding facility. Both sexes were used for experiments. Animals at the age of postnatal day (P) 28-60 were used for immunohistochemical experiments and *in vivo* experiments. Animals at the age of P0-30 were used for *in vitro* patch-clamp experiments.

All experiments were approved according to the German Tierschutzgesetz (55.1-1-54-2531-105-10).

3.4. Stereotactical Injection

3.4.1. Surgery

Animals were briefly anaesthetized with isofluran and immediately injected subcutaneously (s.c.) with a medetomidin, midazolam, fentanyl (MMF) mixture (medetomidin: 0.15mg/kg body mass, midazolam: 7.5mg/kg body mass, fentanyl: 0.03 mg/kg body mass) and additionally injected with meloxicam (10mg/kg body mass) and Ringer infusion. Animals were put back into the cage and the cage covered with a blanket while constantly monitoring the animal. Depth of anaesthesia was controlled by testing the paw pinch reflex. Anaesthetized gerbils were placed onto a heating pad to maintain body temperature. A short strip (~2cm) of fur was sheared along the midline on the gerbils' head to lay bare the skin. The skin was disinfected with ethanol (80%). An incision was made from lambda to 1cm rostral of bregma. The bone rostral to bregma was cleaned with a pledget and a scraper. With dental cement a custom-made head fixative was glued onto the skull directly rostral to bregma. Gerbils were then head fixed in a custom-made stereotaxic frame by screwing the head fixative onto the head bar.

3.4.2. Stereotactical alignment

For the basic orientation the skull was aligned relative to the two sutures lambda and bregma (c.f.Figure 15A). Comparative measurements were taken until x and z coordinates were converging on zero with a tolerance of +/- 25µm. To even the head in x-plane comparative measurements were taken by aligning the two points +2000µm and -2000µm on the x-axis from midline (straight line from lambda to bregma) until converging on zero. Coordinates relative to lambda (x=0, y=0, z=0) for the DNLL, IC and MNTB were all derived from this basic alignment with differences in injection angle (c.f Figure 15B). For setting the injection angle (Fig. α and β) the animal's skull was again rotated in the appropriate plane relative to the basic alignment.

3.4.3. Injection

For the craniotomy a small hole (2mm diameter) was drilled into the skull at the appropriate x-/y-coordinates and the dura mater removed. A glass capillary with

a tip size of 30-40µm (inner diameter) was clamped into the injector and front filled with an aliquot of 1µl *rAAV* containing $9.5\text{-}9.8\times10^{8}$ total vector genomes.

The capillary was lowered to the appropriate coordinates (relative to lambda):

Nucleus	x-coordinate	y-coordinate	z-coordinate	Injector angle
IC	+1900µm	0µm	-3900 /-4000µm	α: 20° to rostral
DNLL	+1750µm	-800 /-900µm	-5400 /-5500µm	β : 4-5° to medial
MNTB	+1050µm	+950µm	-8050 /-8150µm	α: 12° to medial

Stepwise, at a rate of 9.2nl/10sec., the injection was delivered until a final volume of 250nl per injection spot. After 5 min. the injection needle was retracted and the gerbil removed from the stereotaxic frame. For the *in vivo* experiments three to four injections were made in 100µm intervals at the injection coordinates, in the same z-plane. This increased the transduction volume in the DNLL and increased the chances for a direct on target hit.
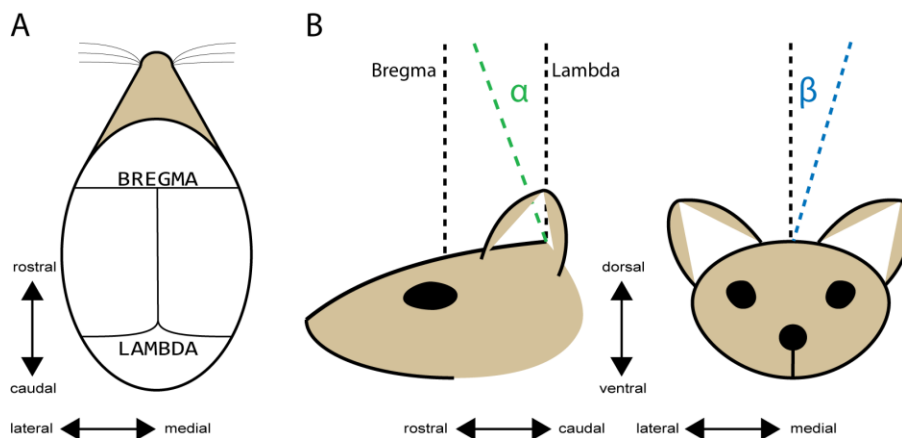
Figure 15: Anatomical landmarks for alignment and injector angles

A. The two sutures lambda and bregma were reference points for stereotactical alignments. **B**. For injections into the DNLL, IC and MNTB different injector angles - α or β - were used.

3.4.4. Post-surgery treatment

The incision on the head was stitched and additionally glued with histoacryl at both ends. The anaesthesia was antagonized with a mixture (AFN) of atipamezole (0.4µg/kg body mass), flumazenile (0.4µg/kg body mass) and naloxon (0.5µg/kg body mass). Ringer infusion (250-500µl) was administered via s.c. injection to prevent dehydration of the animal. The gerbils were monitored closely until recovery and meloxicam administration (10mg/kg body mass) continued for five days post surgery, administered at 24 hour intervals.

3.5. Immunohistochemistry

3.5.1. Transcardial perfusion with PFA

The animals were anaesthetized with a lethal dose of pentobarbital (2 mg/kg body mass) injected intraperitoneally (i.p.). Depth of anesthesia was controlled by the paw pinch reflex. After reflexes and breathing declined the animal's limbs were fixated with tape. With a Y-section from the abdomen to sternum the skin was detached and with an additional transverse section the abdominal cavity was opened and the thoracic diaphragm was cut. With two lateral cuts the rib cage was cut loose and folded out. The left ventricle was pierced with an injection needle. The right atrium was incised at the same time as the perfusion with phosphate-buffered saline (PBS) (with 0.1% heparin and 155 mM NaCl) was started. After five min. the perfusion solution was changed to 4% PFA for 20-30 min. For postfixation the brain is retrieved and incubated in 4% PFA overnight.

3.5.2. Antibody staining

Brains were washed twice in 0.1M PBS and embedded in 4% agar. Brain slices of 50 µm thickness were cut with the vibratome. Slices were collected in 24-well plates and washed again two times for 10 min. in 0.1M PBS. To prevent unspecific binding of the antibodies, slices were incubated in blocking solution with varying Triton-X100 concentration for one hour at room temperature. Primary antibodies were diluted in blocking solution and slices were incubated in the diluted primary antibodies for 24-48 hours at 4°C. Afterwards the slices were washed three times in 0.1M PBS for 10 min. and incubated in secondary

antibodies (diluted in 0.1M PBS) for 4 hours at room temperature. Remaining antibodies were removed from slices by washing three times in 0.1M PBS. The free floating slices were transferred onto a microscope slide and embedded in mounting medium and sealed with a cover slip and nail polish.

3.6. Microscopy

3.6.1. Confocal microscopy

Images were acquired with 8 bit intensity resolution per channel and with a z-step size 0.97μm and size of 512x512 pixels resulting in a voxel size of 0.7568x0.7568x0.6294 μm^3 for the 20x magnification and in 0.2403x0.2403x0.9651 μm^3 for the 63x magnification. Laser scanning frequency was set to 400Hz in unidirectional mode and lines average was calculated from three line scans. Pinhole size was adjusted automatically by the microscope software. Gain and laser power were adjusted in order to balance over- and underexposure of the fluorescence signal.

3.6.2. Virtual Slide Microscopy

Images were acquired with 16 bit intensity resolution per channel and with either 10x or 20x magnification for a whole brain slice in order to confirm anatomical localization of virus injections. Exposure time and light intensity were adjusted in order to avoid over- and underexposure of the fluorescence signal.

3.6.3. Image processing and analysis
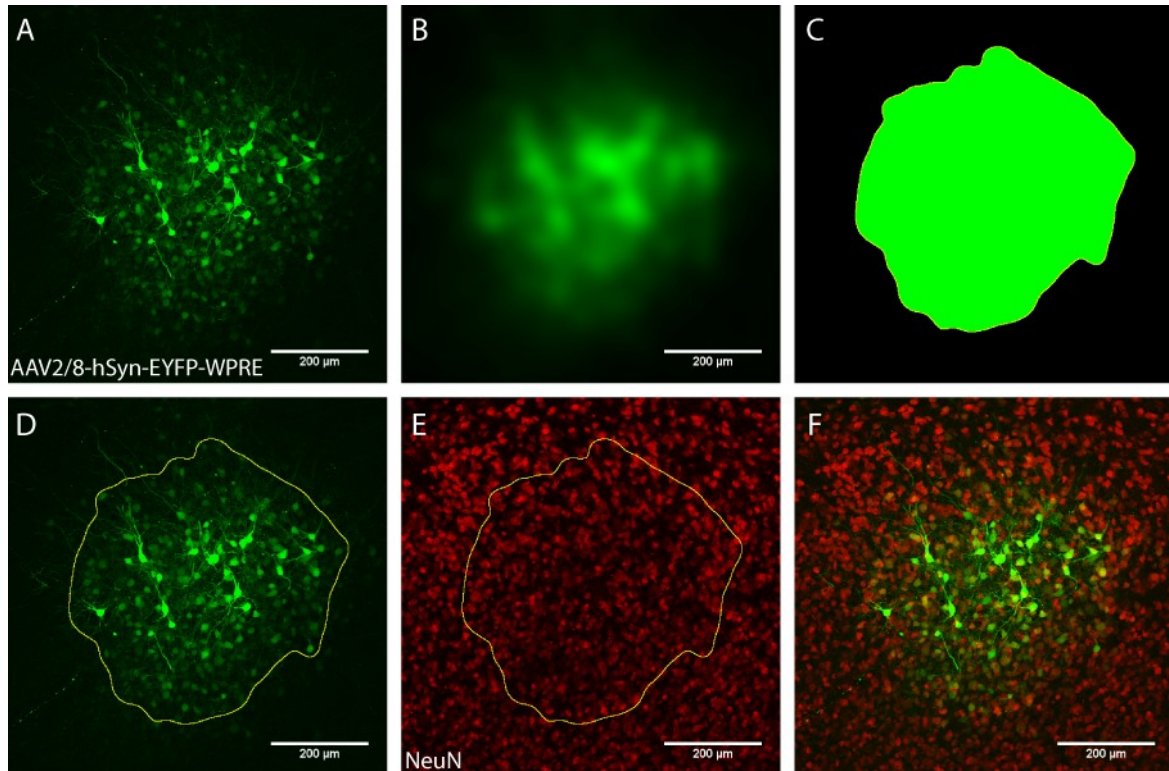
Figure 16: Image processing - Determination of transduction area and counting cells

A. Z-projection of confocal stack with fluorescence channel from virally transduced neurons expressing EYFP was improved in signal-to-noise ratio. **B**. A gaussian blur filter with 20µm diameter was applied to the image to dimish the impact of bright dendrites and axons on the thresholding procedure. **C**. The image was thresholded and thereby made into a binary mask (green area for the signal and black for the background). **D&E**. The outline of the binary mask (yellow line) was applied to the images in the EYFP (**D**) and NeuN channel (**E**). Cells expressing EYFP and cells stained with NeuN within the outline were counted manually. **F**. Overlay of the channels was qualitatively done, to look for co-localization of neuronal marker and virus mediated EYFP expression. Images are examples from a coronal slice of a *rAAV8YF.hSyn.EYFP* transduced IC, three weeks after injection.

A maximum intensity projection or a projection by summation of slices in the confocal stacks was carried out with correction for chromatic aberration (Figure 16A). Background subtraction with a sliding paraboloid radius of 50µm to preserve structures was done to improve signal to noise ratio and contrast was enhanced without saturating pixels. In the overlay of channels the co-localization of neuronal markers (*Map2* or *NeuN*) with virus expressed control-fluorophor (*EYFP* or mCherry) was determined (16F). The channel of the neuronal markers also served as basis to identify auditory nuclei.

For counting cells also maximum intensity projection or a projection by summation of slices in the confocal stacks was carried out as described above. The channel with the signal from transduced neurons expressing EYFP was gaussian blurred with a radius of 20µm to preserve the signal from cell somata but to diminish the signal from small structures like dendrites and axons. in order to improve the results of thresholding (c.f. 16B). The gaussian blurred picture was thresholded by a level at least 3 times above background intensity via mean intensity algorithm and the resulting area determined as "transduction area" (16C). Area and volume of the transduction area were measured. The cells stained with neuronal marker (*NeuN*) and the transduced neurons expressing EYFP inside the area were counted two times manually and the average determined as the total number of neurons in the transduction area or as the number of transduced neurons in the transduction area respectively (16E&D). The ratio of transduced neurons to total number of neurons was determined as transduction efficiency.

$$transduction\ efficiency = \frac{(number\ of\ transduced\ neurons)}{(total\ number\ of\ neurons)}$$

To determine the multiples of background fluorescence ("fold background"), which can be seen as signal to noise ratio (SNR), sum projections from confocal scans were made. All confocal scans were made with the same laser power (35%), signal gain (35%) and signal threshold (0.4% offset). A circle with 8µm diameter was fitted into the soma of a transduced neuron and the average pixel intensity inside the circle in the *EYFP* channel was measured. This was done for 52 transduced neurons per injected animal. The average background fluorescence was measured as well, by choosing three different spots of random size outside the injection area and measuring the average pixel intensity in the *EYFP* channel in this spots. The average of these three values was determined as the average background intensity. The "fold background" was then calculated by dividing the average pixel intensity from a transduced neuron by the average background intensity.

$$fold\ background = \frac{(average\ intensity\ transduced\ neuron)}{(average\ background\ intensity)}$$

3.7. Electrophysiology

3.7.1. *In vitro* recordings

10-28 days post injection (dpi) gerbils were anaesthetized with Isofluran and decapitated. The brain was removed and kept in slice solution bubbled with 95% O_2 and 5% CO_2. For gerbils below the age of postnatal day (P) 21, the slice solution was bubbled on ice whereas for older stages slice solution was bubbled at room temperature. Acute, coronal brainstem sections of 200µm thickness were cut using a vibratome. They were incubated in at 36°C for 45 min. and the extracellular recording solution bubbled with 5% CO_2 and 95% O_2.

After incubation, slices were transferred to a recording chamber attached to the microscope and weighted down with nylon strings fastened to a silver brace. The recording chamber was continuously perfused with extracellular solution containing D-APV and DNQX to block glutamatergic transmission for current clamp experiments. All voltage clamp and current clamp recordings for experiments with *NpHR3.0* were carried out at near-physiological temperature (33–36°C) whereas current clamp recordings for experiments with CatCH were done at room temperature. All voltage clamp recordings were done with a holding potential at -60mV. All cells were visualized with infrared differential interference contrast and transduced neurons were identified by the *EYFP-* or *mCherry* tag when switching into the fluorescence channel. The offsets from the pipette (C-fast) and the membrane (C-slow) were compensated in all recordings. The liquid junction potential was not compensated. For voltage-clamp recordings, access resistance was compensated to residual of 3-4 MΩ of the initial value. Neurons were accessed with glass pipettes (resistance between 3-5 MΩ). Data was acquired at a sampling rate of 20 kHz and Bessel filtered at 2.9 kHz and 10 kHz.

Light stimulation was precisely triggered by the patch-clamp amplifier and delivered through the microscope's objective illuminating the whole slice. Light intensity (0-7.3mW/mm^2) was precisely set by the voltage from analog output of the patch-clamp amplifier. The light intensity output at the level of the slice was measured with the power meter console according to manufacturer's recommendations.

All recording protocols were created in the pulse generator or pulse editor tool in the patchmaster program. For the characterization of the cell the following protocols were carried out: To calculate the membrane resistance (R_m) a current step of -5pA for 500ms was injected into the cell in current clamp mode and the sweep repeated 50 times. To determine the action potential threshold 1ms long step currents starting from 0 pA with an increment of +25 pA were

injected into the cell in current clamp mode for 40 sweeps. To determine the firing pattern 500ms current steps were injected starting at -500pA with an increment of 25pA and ending at +500pA.

Protocols for CatCH experiments included triggered light pulse trains at 5,10,20,33.3,40,50,66.6 and 100Hz frequency with 100% light intensity (=7.3mW/mm^2 at 470nm) but varying pulse width (ranging from 0.04 to 100ms) in current clamp mode for five sweeps with 5 sec. break in-between sweeps.

Protocols for *NpHR3.0* experiments included a triggered light pulse for 500ms with 100% light intensity (=6.2mW/mm^2 at 590nm) for five sweeps in voltage clamp mode.

To determine the light intensity dependence of the photocurrent the response to a triggered light pulse for 500ms starting from 0% light intensity and ending at 100% with increments of 10% was recorded in voltage clamp mode.

In vitro data analysis

Electrophysiological data (*.dat files) were loaded into IGOR Pro with Patchers Power Tools 2.19 extension (link). Raw traces were analyzed with custom written user procedures. Latencies were measured as the time from trigger onset to the peak of the action potential (AP). Only APs elicited within 30ms or shorter than one period of the stimulation frequency after trigger onset were considered successful. The phase (Θ) of each successful elicited AP was calculated for all trials (n). Vector strength (r) was calculated according to the formula below as in Goldberg, J.M. and Brown, P.B. (Goldberg and Brown, 1969).

$$r = \frac{\sqrt{(\sum \cos \theta_i)^2 + (\sum sin \theta_i)^2}}{n}$$

Jitter was calculated as the standard deviation (sd) of AP latencies (x) over all trials (n) according to the formula below ($\overline{x}$ is the expected value):

$$jitter = sd = \sqrt{\frac{\sum(x - \overline{x})^2}{(n-1)}}$$

Efficiency of light stimulation was calculated as "successful spike (%)" according to the formula below:

$$successful\ spike\ (\%) = \left(\frac{elicited\ AP}{total\ number\ of\ trigger\ events}\right) * 100$$

Extra spikes were regarded as APs happening after the light stimulation ended or APs happening after the first spike within a period of the stimulation frequency. The occurrence of extra spikes (in %) was calculated according to the formula below:

$$extra\ spike\ (\%) = \left(\frac{extra\ spike}{total\ number\ of\ trigger\ events} \right) * 100$$

The median latency of a spike was calculated from five repetitions.

The 20/80 rise time ($t_{20/80}$) was calculated as the time from 20% to 80% amplitude of the peak photocurrent.

Tau on (τ_{on}) of the photocurrent was determined as the tau of an exponential function fitted to the average photocurrent (range for fitting: trigger onset to peak of photocurrent). For the curve fit, the inbuilt exponential function in Igor Pro was used.

Tau off (τ_{off}) of the photocurrent was determined as the tau of an decaying exponential function fitted to the average photocurrent (range for fitting: from the end of the trigger to baseline current (0pA)). The formula of the exponential function used for the fit is the same as described above.

3.7.2. *In vivo* electrophysiology

Surgery and stereotactical alignment

3-8 weeks after *rAAV*-injection gerbils were anaesthetized by an initial intraperitoneal injection of a Ringer infusion containing ketamine chloride in 20% v/v and xylazine chloride in 2% v/v and depth of anaesthesia was monitored by testing the paw pinch reflex. During recording, animals were injected continuously with anesthetic via an automatic pump at a pump rate of 1.6–2.4 µl/min, depending on body weight. Animal body temperature was monitored and, if necessary, adjusted using a thermostatically controlled heating pad. Before recording, skin and tissue covering the upper part of the skull were removed carefully. A small metal rod was mounted on the frontal part of the skull to secure the head of the animal in a stereotaxic frame during recordings.

After surgery, the animal was transferred into a sound-attenuated chamber, and the animal's head was fixed in a custom-made stereotaxic frame (Schuller et al., 1986). The animal's position in the stereotaxic frame was standardized by stereotactic landmarks on the surface of the skull (intersections of the bregmoid

and lambdoid sutures with the sagittal suture in horizontal and vertical alignment) (Loskota et al. 1974). For electrode penetrations to the DNLL and IC, a small rectangular hole was drilled into the skull extending 1−2.5 mm lateral from the midline and 0.5–1mm caudal of the interaural axis. The dura mater overlying the cortex was removed carefully and during the recording session Ringer infusion was applied to the opening to prevent dehydration of the brain. For DNLL recordings, the recording electrode was tilted 10° or 5° medially, for some IC recordings the electrode was tilted 20° rostrally. The position of the last recording was marked by a current induced lesion of 25% of 100 µA for 90 sec. using metal electrodes. After recording, the animal was killed by intracardial injection of 250µl pentobarbital.

Light delivery

For light stimulation an optic fibre (200µm) was inserted into a steel cannula and the upper end glued into a ceramic ferrule. Ferrule and fibre end were sanded with increasingly finer grading until perfectly flush. The fibre was then connected to the LED light source via connectorized 2m long optic fibre and mating sleeve. LEDs were controlled with a 4 Channel LED Driver and Single LED Connector Hub and triggered and intensity-adjusted with the patch-clamp amplifier. The cannula holding the optical fibre was fixed onto a micromanipulator and placed either within 100-350µm proximity of the recording site or exactly contra-lateral to the recording site. The maximal light power right in front the optical probe was measured to be 7.1mW and the maximal light power at the tip of the optical probe was measured to be 0.5 - 4.5mW depending on the flushness of the connection. The LEDs output was always set to its maximal power of 9.0mW at 617nm.

Recordings and stimuli

Single unit responses were recorded with glass electrodes filled with 1 M NaCl (~6-10 MΩ). The recording electrode was advanced under remote control, using the single axis micromanipulator. Extracellular action potentials were recorded with the patch-clamp amplifier; a noise eliminator removing residual line noise picked up by electrode was used and the signal from the patch-clamp amplifier converted by a RZ-6 Multi I/O Processor. Isolation of action potentials from a single cell (signal-to-noise ratio >2) was ensured by visual inspection of the voltage traces amplitude of the action potential and by off-line spike cluster analysis based on stable amplitudes of the positive and negative peaks (volt) and robust spikes waveform in Brainware.

Acoustic stimuli were generated at 50kHz sampling rate and digitally filtered using finite impulse response folding (FIR) by the RZ-6 Multi I/O Processor to generate a phase- and amplitude-corrected output from the earphones. Output of the earphones was calibrated with a measuring and the impulse response recorded with a condenser microphone.

The standard setting was a broadband stimulus with duration of 200ms plus squared-cosine rise/fall times of 5ms on the contralateral ear and the same stimulus with duration of 20ms on the ipsilateral ear after the first 100ms, with 900ms pause between every repetition. For all recordings, stimulus presentation was random interleaved. To search for acoustically evoked responses, noise stimuli without interaural time and intensity differences were delivered binaurally. When a neuron was encountered, its best frequency (BF) and threshold using binaurally identical (ILD/ITD = 0) sinus tone stimulation was determined. The frequency that elicited responses at the lowest sound intensity was defined as BF, the lowest sound intensity evoking a noticeable response at BF as threshold. Additionally, its aurality (monaural: E0/0E or binaural: EI, IE, EE. E…excitatory ear, I…inhibitory ear, 0…no input) and its firing pattern was identified with basic stimuli. These properties were determined on-line by audio-visual inspection in all neurons and, in almost all neurons, confirmed by a careful off-line analysis of the frequency versus level response areas. These parameters were used to set stimulus parameters subsequently controlled by the computer. In addition, monaural and binaural broadband noise was presented so that the binaural properties (aurality) could be determined.

Data analysis

Recordings were saved in the *.bwvt and *.src file format. Spikes were sorted in Brainware by plotting the amplitudes of the positive voltage peak against the negative voltage peak.

Spike counts were determined by counting the number of spikes during the stimulus evoked response and subtracting the spontaneous spikes in absence of a stimulus by using the Brainware routine for spike counts. This subtraction was carried out to isolate the stimulus evoked responses. The normalized spike count was derived by dividing the sum of all spike counts (= 50 repetitions) of a test condition by the sum of all spike counts in the control condition without light (= 50 repetitions).

$$normalized\ spike\ count = \frac{\sum_{i=0}^{i=50}(spike\ counts: condition\ with\ light)_i}{\sum_{i=0}^{i=50}(spike\ counts: control\ without\ light)_i}$$

The effect size was calculated by taking the absolute value of the difference of the spike counts of the control condition without light and the test condition with light and dividing it by the spike count of the control condition without light. When the value for effect size reaches one, it means complete suppression of spiking whereas a value of zero means no suppression in the test condition. Values above one mean an enhancement of spiking in the test condition.

$$effect\ size_i = \frac{(|spike\ counts{:}test\ condition - spike\ counts{:}control\ without\ light|)_i}{(spike\ counts{:}control\ condition\ without\ light)_i}$$

The latencies of the spikes were all measured from the beginning of the recording (=0ms), not from the onset of the sound stimulus.

4. Results

4.1. Molecular Cloning

In order to apply the following new recombinant *AAV* (*rAAV*) vectors in experiments, the *AAV* vector backbone had to be cloned first in the form of a plasmid (*pAAV*). The expression cassette is the basis for actual *rAAV* and comprised of the promoter, the transgene and expression elements (e.g. WPRE, hGH polyA signal,…) flanked by the viral ITRs. To amplify the *pAAV* in bacteria a origin of replication (e.g. pUC ori, f1 ori,..) is incorporated outside the expression cassette. A selection marker (e.g. ampicillin resistance) is incorporated outside the expression cassette as well, to allow for the positive selection of bacterial hosts containing the vector plasmid (for details see Material and Methods section, chapter 2.9). The final, functional *rAAV* virion containing single stranded (ss) DNA is then named by its backbone and serotype separated by a slash, in my experiments the backbone used is the *AAV2* and the serotype used is the serotype *8Y337F*, hence *rAAV2/8Y337F.* The abbreviation *rAAV8YF* is also used synonymously.

4.1.1. pAAV2-ss-hSyn-GFP-WPRE

To test for neuron specific expression after *rAAV* transduction in auditory nuclei and as a control vector this construct was cloned to mediate *GFP* fluorescence in affected cells. As a donor plasmid for the *pAAV2* backbone with a *eGFP* fluorophor served *pAAV2-ss-hArr-eGFP-WPRE*. The *hArr* promoter was cut out with NheI and BamHI and the sticky ends of the vector plasmid were blunted with T4 polymerase. For the insert the *hSyn* promoter (485bp) was cut out from the *pAAV2-ss-hSyn-EYFP-WPRE* vector (from Dr. Karl Deisseroth) with NotI and BamHI and ends were blunted with T4 polymerase. The blunted *pAAV2-ss-[/]-eGFP-WPRE* vector was dephosphorylated and ligated with the blunted *hSyn* insert. Subsequently chemical competent ß10 *E.coli* were transformed with the ligated DNA. *E.coli* clones with the correct plasmid and insert in the right orientation were determined by digesting the isolated plasmid DNA with XbaI and BsrgI after preparation. Finally, the integrity of the ITRs was successfully tested by digesting with Eam1105 (1319, 1609, 2334bp fragments) and SmaI (11, 2367, 2873bp fragments) (Figure 17).
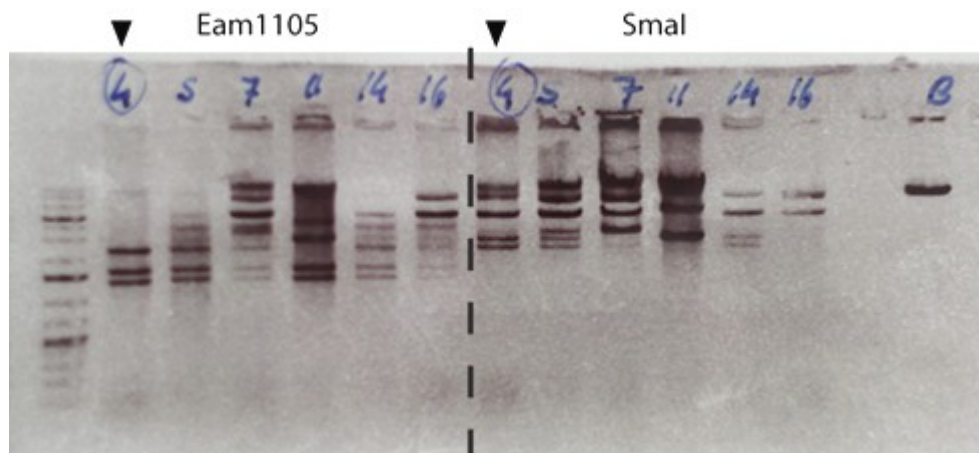
Figure 17: Digest of pAAV2-ss-hSyn-GFP-WPRE clones with Eam1105 and SmaI

Picture of the agarose gel with separated DNA bands from the digests. On the left side of the dashed line digests with Eam1105 are shown, on the right side digests with SmaI are shown. The clone with the correct fragment pattern was clone "4" also marked by the black triangle.

4.1.2. pAAV2-ss-hSyn-CatCH-mcherry-WPRE

To test for the amount and precision of photostimulation after *rAAV* transduction in injected nuclei, this construct was cloned to mediate excitation by *CatCH* and fluorescence by *mcherry* in affected cells.

pAAV2-ss-hSyn-hChR(H134R)-mcherry-WPRE (from Dr. Karl Deisseroth) served as donor plasmid for the vector backbone. The whole insert between the *hSyn* promoter and the WPRE sequence had to be cut out with SalI and HindIII (Figure 18A), because there were no cloning sites available to retain *mcherry*. Additional dephosphorylation of the resulting sticky ends avoided any stochastic re-ligation. The *CatCH* insert (950bp) was amplified with the primers "fw-SalI-Cat" and "rev-HindIII-Cat" in a PCR with annealing temperature set at 60°C and elongation time of 1 minute and 30 sec. for 35 PCR cycles (Figure 18B). The PCR product was agarose gel purified, cut with SalI and HindIII and gel purified again. The cut *CatCH* insert was ligated into the dephosphorylated vector plasmid. The ligation was transformed into ß10 *E.coli* and the positive clones were selected by digesting isolated plasmid DNA with BstE II (resulting in fragments of 1460 and 4024bp length). The now ligated vector plasmid *pAAV2-ss-hSyn-CatCH-WPRE* was cut with HindIII and dephosphorylated (Figure 18C&D). As a fluorescent tag *mcherry* was chosen due to a different excitation spectrum than *CatCH*. The *mcherry* insert was amplified in a PCR with the primers "fw-HindIII-chry" and "rev-HindIII-chry". The annealing

temperature was set to 60°C and the elongation time to one minute for 35 cycles. The PCR product (707bp) was agarose gel purified, digested with HindIII and gel purified again. The cut *mcherry* insert was ligated in the *cut pAAV2-ss-hSyn-CatCH-[/]-WPRE* and ligation was transformed into the ß10 *E.coli*. Positive clones with the correct plasmid were identified by digesting isolated DNA after preparation with PvuII (1410, 2171 and 2620bp fragments) and integrity of ITRs was verified by digesting with SmaI (11, 2681 and 3494bp fragments) and Eam1105 (370, 474, 963, 1262, 1356 and 1773bp fragments) (Figure 18E&F).
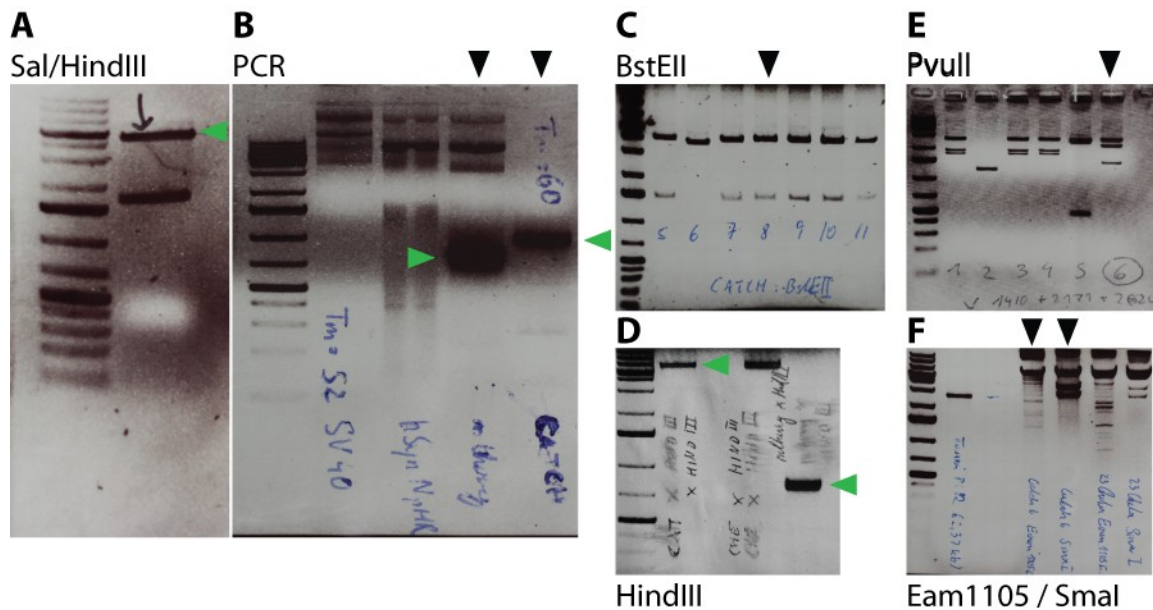
Figure 18: The cloning steps for *pAAV2-ss-hSyn-CatCH-mcherry-WPRE*

A. Picture of agarose gel shows digestion of *pAAV2-ss-hSyn-hChR(H134R)-mCherry-WPRE* with SalI and HindIII. Green triangle highlights the cut vector of correct fragment size. **B**. Picture of the agarose gel with the separated PCR products of *CatCH* (950bp) and *mcherry* (707bp) inserts. The green triangels mark both bands of correct size. **C.** Picture of the agarose gel with BstEII digests of pAAV2-ss-hSyn-CatCH-WPRE. The black triangle marks the lane with the clone "8" displaying the correct fragment pattern. **D.** Picture shows the agarose gel of a HindIII digest of the *pAAV2-ss-hSyn-CatCH-WPRE* vector and the *mcherry*-insert. Green triangles point towards the correct fragments. **E.** The picture shows a PvuII digest of *pAAV2-ss-hSyn-CatCH-mcherry-WPRE* clones. The black triangle points to the lane of the correct clone. **F.** Picture from the agarose gel shows the fragment pattern of SmaI and Eam1105 digests of the correct clone. Black triangles point to both lanes with the correct fragment pattern.

4.1.3. pAAV2-ss-hSyn-ChETA-mcherry-WPRE

To test for the amount and precision of photostimulation after *rAAV* transduction in injected nuclei, this construct was cloned to mediate fast and precise excitation by *ChETA* and fluorescence by *mcherry* in affected cells.
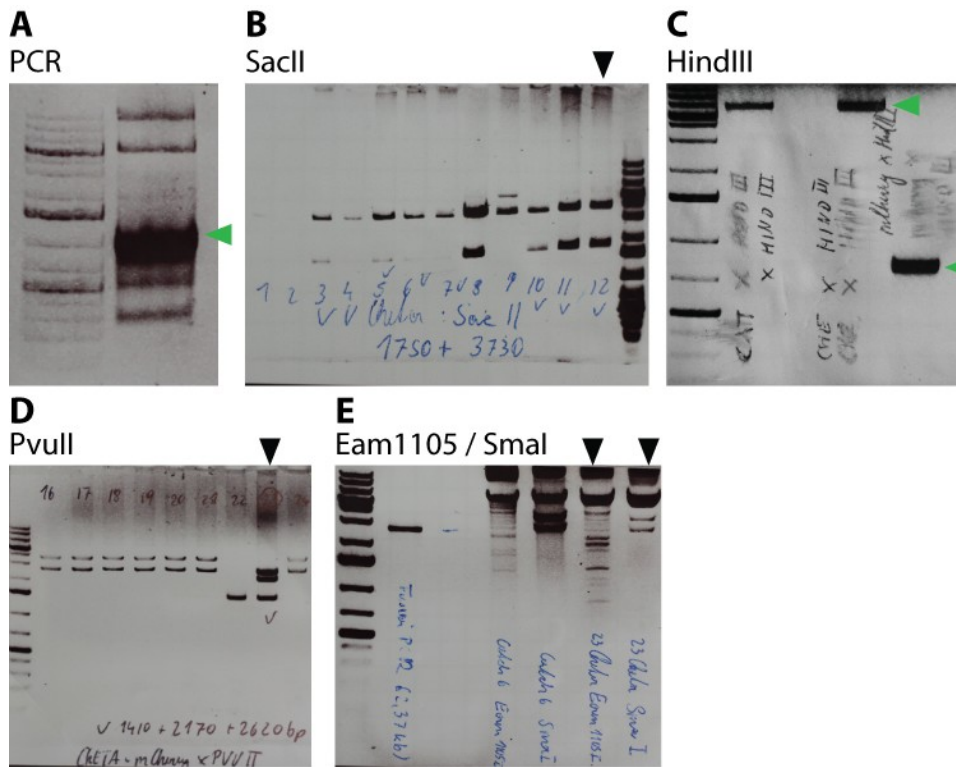
Figure 19: Cloning steps for *pAAV2-ss-hSyn-ChETA-mcherry-WPRE*

A. Shows agarose gel of ChETA amplicon from a PCR. Green triangle points towards correct band. **B.** Shows agarose gel of SacII digested clones of *pAAV2-ss-hSyn-ChETA -WPRE*. Black triangle marks the lane with the correct fragment pattern. **C.** Shows agarose gel of HindIII digested *pAAV2-ss-hSyn-ChETA -WPRE* and *mcherry*-insert. Green triangle points to the correct bands. **D.** Agarose gel of *pAAV2-ss-hSyn-ChETA -mcherry-WPRE* clones digested with PvuII. Black triangle marks the lane with the right fragment pattern. **E.** Agarose gel of digests with Eam1105 and SmaI. Black triangle points towards the lanes with the correct fragment pattern.

The same donor plasmid *pAAV2-ss-hSyn-hChR(H134R)-mCherry-WPRE* and cloning strategy as before was employed. The donor plasmid was digested with SalI and HindIII and dephosphorylated and purified by agarose gel electrophoresis. *ChETA* (930bp) was amplified with the primers "fw-SalI-ChE" and "rev-HindIII-ChE" by PCR. Annealing temperature was set to 60°C and elongation time to 1 minute and 30 sec. for 35 PCR cycles. The PCR product was agarose gel purified (Figure 19A), digested with SalI and HindIII and purified again. The cut *ChETA* amplicon was ligated into the dephosphorylated vector and the ligation transformed into ß10 *E.coli*. Positive clones were

identified by digesting isolated DNA from plasmid preparation with SacII (resulting in fragments of 1750 and 3730bp length) (Figure 19B). The correct plasmid was cut with HindIII and dephosphorylated. The flourescent *mcherry* tag was amplified and cut with HindIII like described above (Figure 19C). The cut *mcherry* amplicon was ligated into the cut *pAAV2-ss-hSyn-ChETA-[/]-WPRE* and ligation transformed into ß10 E.coli. The correct *pAAV2-ss-hSyn-ChETA-mcherry-WPRE* plasmid was identified by digesting with PvuII (1410, 2170 and 2620bp fragments) and fidelity of ITR sequences were again tested by digesting with SmaI and Eam1105 (Figure 19D&E).

4.1.4. pAAV2-ss-hSyn-CatCH-mcherry-T2A-NpHR3.0-WPRE

To combine photostimulation and suppression with light simultaneously after *rAAV* transduction in neurons, this construct was cloned to mediate excitation by *CatCH*, suppression by *NpHR3.0* and fluorescence by *mcherry* in affected cells. The *T2A* element allows for posttranslational segregation of the flanking genes.

The donor plasmid *pAAV2-ss-hSyn-hChR2(H134R)-EYFP-WPRE* (from Dr. Karl Deisseroth) was digested with SalI and EcoRI to cut out the part between hSyn promoter and the WPRE sequence and dephosphorylated. The new insert *CatCH-mcherry-T2A-NpHR* was constructed by fusion PCR. The three parts of the insert, namely *CatCH-mcherry* (1638bp length), *-T2A-* (80bp length), and *-NpHR3.0* (1001bp length), were first amplified in PCR. With the primers "fw sal1 catch" and "rv *mcherry*", annealing temperature set at 61°C and elongation time at 1 minute and 45 sec., the *CatCH-mcherry* part was amplified in 38 PCR cycles. With the primers "Fw *mcherry* T2A" and "Rev T2A", the annealing temperature set at 60°C and the elongation time set to 10 sec. the *T2A* part was amplified in 35 PCR cycles. With the primers "fw T2A NpHR" and "rv ecoRI NpHR", annealing temperature set at 61°C and elongation time at 1 minute the *NpHR3.0* part was amplified in or 35 PCR cycles. All three amplicons were purified with an agarose gel electrophoresis (Figure 20A). In a next PCR, the part 2 and part 3 were fused with primers "Fw *mcherry* T2A" and "rv ecoRI NpHR" annealing temperature set at 63°C and elongation time at 1 minute and 10 sec. in 38 PCR cycles. The now combined part was agarose gel purified and joined with the first part by another fusion PCR. The primers "fw sal1 catch" and "rv ecoRI NpHR" were used at 60°C annealing temperature and 3 min. elongation time in 38 PCR cycles. The resulting amplicon *CatCH-mcherry-T2A-NpHR3.0* (2680bp length) was purified with agarose gel

electrophoresis (Figure 20B) and ligated into the *pJet1.2* cloning vector. The ligation was transformed into ß10 *E.coli*. Correct clones were identified by digesting isolated DNA after preparation with PvuII (552, 1196 and 3943bp fragments) and NcoI (54, 870, 1345 and 3392bp fragments) (Figure 20C&D). The insert was then cut out from the correct cloning vector with SalI and EcoRI and ligated into the cut donor plasmid (Figure 20E). Again the ligation was transformed into ß10 *E.coli* and the isolated DNA was digested after plasmid preparation with PstI (163, 1787, 2605 and 2675bp fragments). Integrity of ITRs was verified by digesting with SmaI and Eam1105 (Figure 20F).
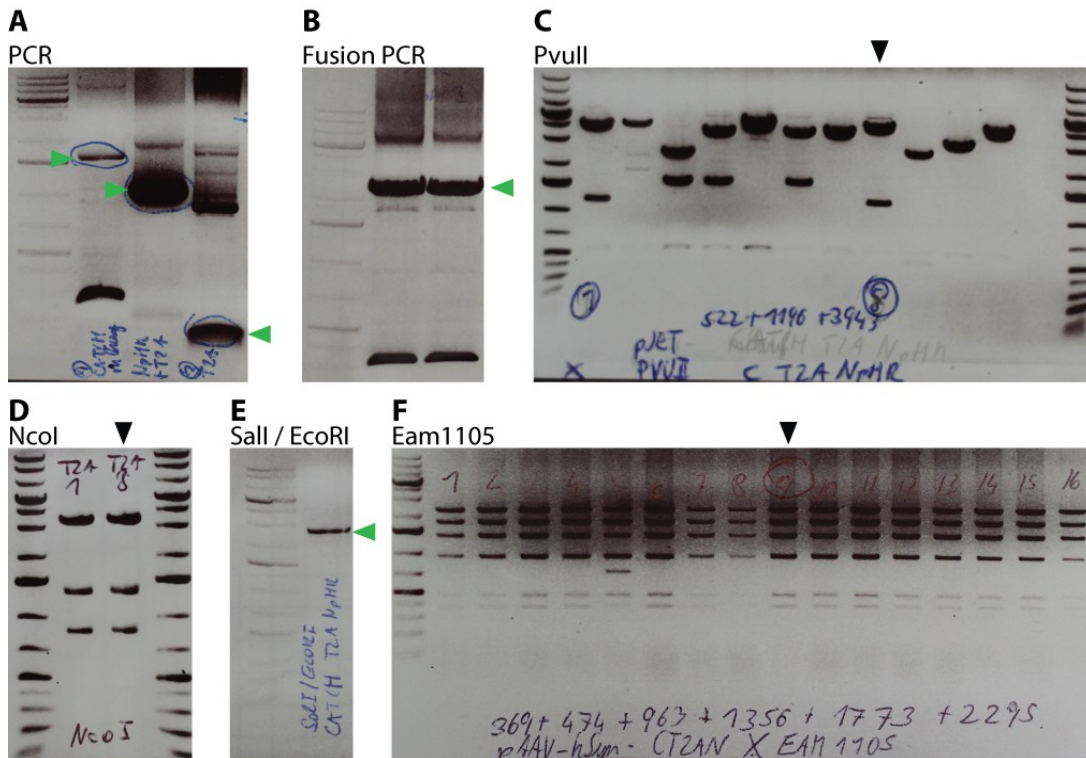
Figure 20: Cloning steps for *pAAV2-ss-hSyn-CatCH-mcherry-T2A-NpHR-WPRE*

A. The picture shows the PCR products of all three inserts, CatCH-mcherry, NpHR3.0 and T2A, separated on an agarose gel. The green triangles point towards right-sized bands. **B.** The picture shows an agarose gel of the joined PCR product from all three inserts. The green triangle points toward correct band. **C**. The picture shows an agarose gel with PvuII digested clones of pJet1.2 containing the fusion PCR inserts. The black triangle points towards clone with correct fragment pattern. **D**. The picture shows an agarose gel with the NcoI digested pJet1.2 clones. The black triangle marks the clone "8" with the correct fragmentation pattern used for further cloning. **E**. The picture shows an agarose gel of the fusion PCR insert cut out with SalI and EcoRI. The green triangle points towards the correct band. **F.** The picture shows an agarose gel loaded with the Eam1105 digest of pAAV2-ss-hSyn-CatCH-mcherry-T2A-NpHR-WPRE. The black triangle marks the lane with the correct fragment pattern.

4.1.5. pAAV2-sc-hSyn-NpHR-mcherry-SV40pA

For suppression and fast expression times after *rAAV* transduction in injected nuclei, this self-complementary construct was cloned to mediate suppression by *NpHR3.0* and fluorescence by *mcherry* in affected cells.
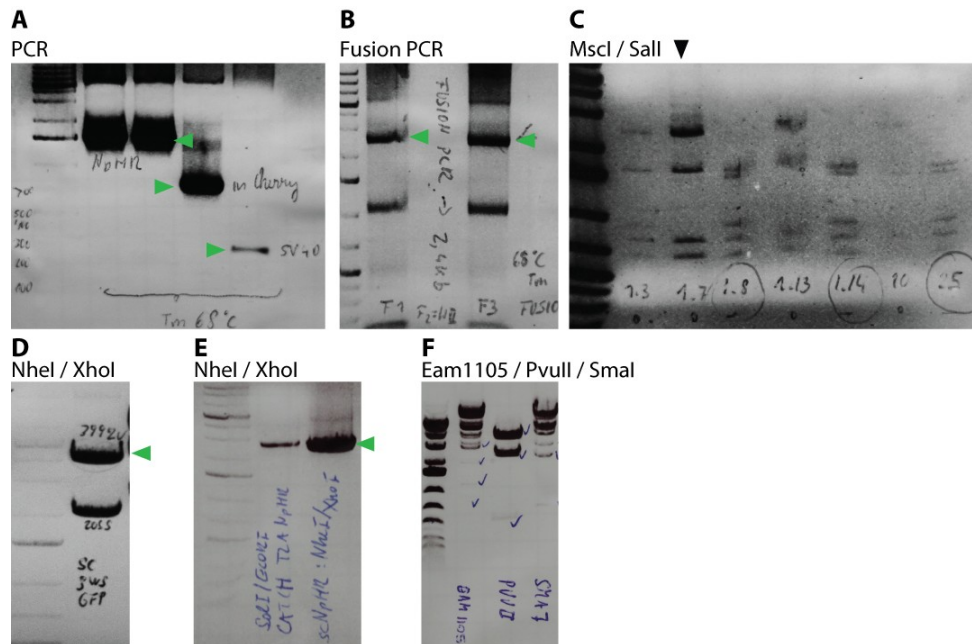
Figure 21: Cloning steps for pAAV2-*sc-hSyn-NpHR3.0-mcherry-SV40pA*

A. Shows agarose gel with PCR products for all three inserts: *hSyn-NpHR3.0*, *mcherry* and *SV40pA*. Green triangles point towards correct bands. **B.** Agarose gel shows fusion PCR product from all three inserts. Green triangles point towards the correct sized bands. **C** Agarose gel loaded with digest of subclones pRC with SalI and MscI. Black triangle marks the lane with the correct fragment pattern. **D** Digest of the sc-donor plasmid with NheI and XhoI separated on an agarose gel. Green triangle points to the correct band. **E**. Fusion PCR insert cut out from subclone with NheI and XhoI and separated on a agarose gel. Green triangle points to the correct band. **F.** Test cuts of *pAAV2-sc-hSyn-NpHR3.0-mcherry-SV40pA* separated on an agarose gel. From left to right: Eam1105, PvuII and SmaI. All digests showed the correct fragment pattern.

As donor plasmid for the self-complementary *AAV* backbone served *pAAV2-sc-SWS-GFP*. The donor plasmid was cut with NheI and XhoI, dephosphorylated and agarose gel purified. Since the insert size for the self-complementary vector was restricted to 2.4-2.5 kb, the *WPRE* sequence and the hGH-polyA signal were replaced with the shorter *SV40-polyA* sequence (only 255bp length instead of ~1100bp). The insert was produced by fusion PCR. The first part *hSyn-NpHR3.0-* (1493bp length) was amplified with the primers "Fw-Syn-SalI" and "Rev-NpHR-TS" with the annealing temperature set at 68°C and elongation time at 1 minute and 15 sec. for 38 PCR cycles. The second part *-mcherry-*

(756bp length) was amplified with the primers "Fw-mCherry-oh" and "Rev-mCherry-ER" in a PCR with the annealing temperature set at 68°C and the elongation time at 1 minute for 38 cycles. The third part -*SV40pA* (255bp length) was amplified in a PCR with the primers "Fw-SV40-ER-oh" and "Msc1-Hind3-SV40-Rev" and with annealing temperature set at 68°C and elongation time set to 20 sec. All three amplicons were purified by agarose gel electrophoresis (Figure 21A). The joined product of all three parts -*hSyn-NpHR3.0-mcherry-SV40pA*- (2432bp length) was generated in a single fusion PCR. With the primers "Fw-Syn-SalI" and "Msc1-Hind3-SV40-Rev" the elongation time set to 2 min. and 30 sec. The annealing temperature for the first six cycles was set to 60°C and for the following 32 cycles set to 68°C. The PCR product was agarose gel purified (Figure 21B) and sub-cloned into the *pRC Blunt II TOPO* cloning vector. *ß10 E.coli* were transformed and correct inserts identified by cutting isolated DNA with EcoRI (325 and 2769bp fragments) and double digesting with MscI and SalI (96, 359, 660, 793, 925, 1495 and 1616bp fragments) after plasmid preparation (Figure 21C). Now the cloning vector with the fused insert served as PCR template. The insert was amplified in 35 PCR cycles with the primers "NheI-hSyn-Fw" and "SV40 XhoI rev" at an annealing temperature of 60°C and an elongation time of 2 min. and 30 sec. The amplicon was agarose gel purified, cut with NheI and XhoI and gel purified again (Figure 21D&E). The cut PCR product was ligated into the cut and dephosphorylated self-complementary vector. The ligation was transformed into ß10 *E.coli*. Positive clones were identified by digestion of isolated plasmid DNA with PvuII (551+2221+3638bp fragments) and test cuts with SmaI (639, 2047 and 3702bp fragments) and Eam1105 (876, 1128, 1777 and 2629bp fragments) verified integrity of ITRs (Figure 21F).

4.1.6. pAAV2-ss-hSyn-ArclightQ239-WPRE

For imaging of transmembrane potentials after *rAAV* transduction in injected nuclei, this construct was cloned to mediate voltage dependent fluorescence by *ArclightQ239* in affected cells

As donor plasmid served again *pAAV2-ss-hSyn-hChR2(H134R)-EYFP-WPRE* (from Dr. Karl Deisseroth). The donor plasmid was digested with SalI and HindIII, gel purified and dephosphorylated. *ArclightQ239* insert (1443bp length) was amplified in a PCR from the template plasmid (addgene #36856) with the primers "ArcL-Sal1-fw" and "ArcL-Hind3-rv3". The annealing temperature was set to 60°C and the elongation time to 1 minute and 30 sec. for 35 cycles. The amplicon was agarose gel purified, digested with SalI and HindIII and agarose

gel purfied again. The cut insert was ligated into the cut and dephosphorylated *pAAV2-ss-hSyn-[/]-WPRE* vector (Figure 22A). The ligation was transformed into ß10 E.coli. Positive clones were identified by digesting isolated DNA after plasmid preparation with PvuII (690, 1320, 1365 and 2619bp fragments) (Figure 22B). Integrity of ITRs was successfully evaluated by digesting with SmaI (11, 2681 and 3291bp fragments) and Eam1105 (474, 963, 1773 and 2784bp fragments) (Figure 22C&D).
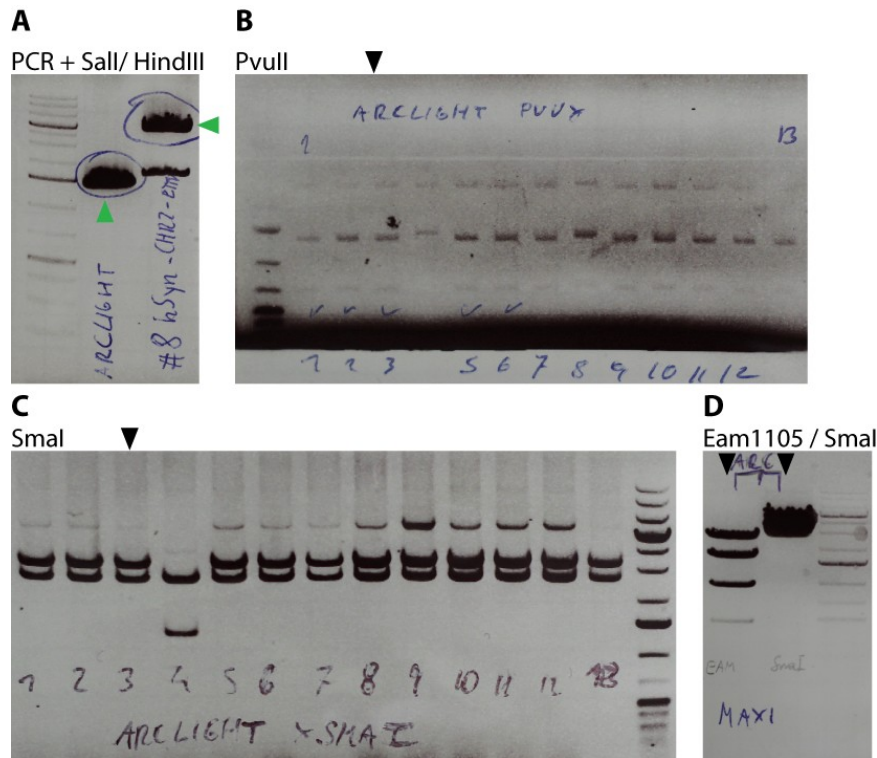
Figure 22: Cloning steps for pAAV2-ss-hSyn-Arclight Q239-WPRE

A. Shows Arclight PCR product and cut donor plasmid separated on an agarose gel. Green triangle point towards correct bands. **B.** Agarose gel loaded with PvuII digested *pAAV2-ss-hSyn-Arclight-Q239-WPRE* clones. Black triangle marks clone with correct fragment pattern. **C**. Agarose gel with SmaI digested clones. Black triangle marks clone with correct fragment pattern **D.** Agarose gel with Eam1105 (left lane) and SmaI (right lane) digested clone shows correct fragment pattern. Black triangles mark both lanes.

4.2. Prerequisites for gene delivery with *rAAV vectors*

As a vector for gene delivery into *the Mongolian Gerbil's* central nervous system *rAAVs* had to meet the following prerequisites for our experiments:

1) The *rAAV* vector must be able to transduce non-dividing cells like neurons in the auditory midbrain and brainstem.

2) Transgene expression must be restricted to neurons only and neuronal specificity of expression should be achieved by choice of the small (485 base pairs) and highly conserved *human synapsin* (hSyn) as a pan-neural promoter.

3) The transduction must be efficient and reliable i.e. transducing a considerable fraction of neurons at the injection site in all experiments to ensure reproducibility of transduction.

4) The time frame for *rAAV* transduction should entail an expression period as short as possible for initial transgene expression but also a long term stability of transgene expression.

5) Transgene expression must reach high enough levels to impact transmembrane potential and modify spiking behaviour in optogenetic experiments.

The first four points were answered in virus injection experiments and antibody immunohistochemical processing of injected brains with subsequent analysis under the microscope. The fifth point was tackled by *in vitro* whole-cell patch-clamp recordings as well as *in vivo* extracellular recordings. In the following *rAAV* vectors with the DNA backbone of the *AAV2* serotype packaged in the capsid of the *AAV8Y733F* were used for all experiments and henceforward the abbreviation *rAAV8YF* is used instead of the full *rAAV2/8Y733F* denotation.

4.3. *rAAV8YF* vector conveys neuron specific transgene expression

Cellular specificity and tropism of *rAAV8YF*

To address points 1) and 2) from the prerequisites and assess the aptitude of the *rAAV8YF* vectors to stably transduce neurons within auditory nuclei, the control vector (*AAV8YF.hSyn.EYFP)* expressing *EYFP* under control of the human synapsin promoter was injected into three different nuclei of the auditory system. In this straight forward approach any anterograde or retrograde

transport of the virus would also be observed by looking for *EYFP* expression in any other area synaptically connected to the injection site but not injected. Diffusion or spill over of *AAV* leading to ectopic expression in adjacent areas would also be detected. For the sake of technical simplicity, virus injection experiments were first carried out in the *IC*. Due to its dorsal position and its physical size, the *IC* was at short distance and easy to target via a dorsal approach through the skull with the stereotactical injection.

4.3.1. *rAAV8YF* injection into the *Inferior Colliculus* (*IC*)
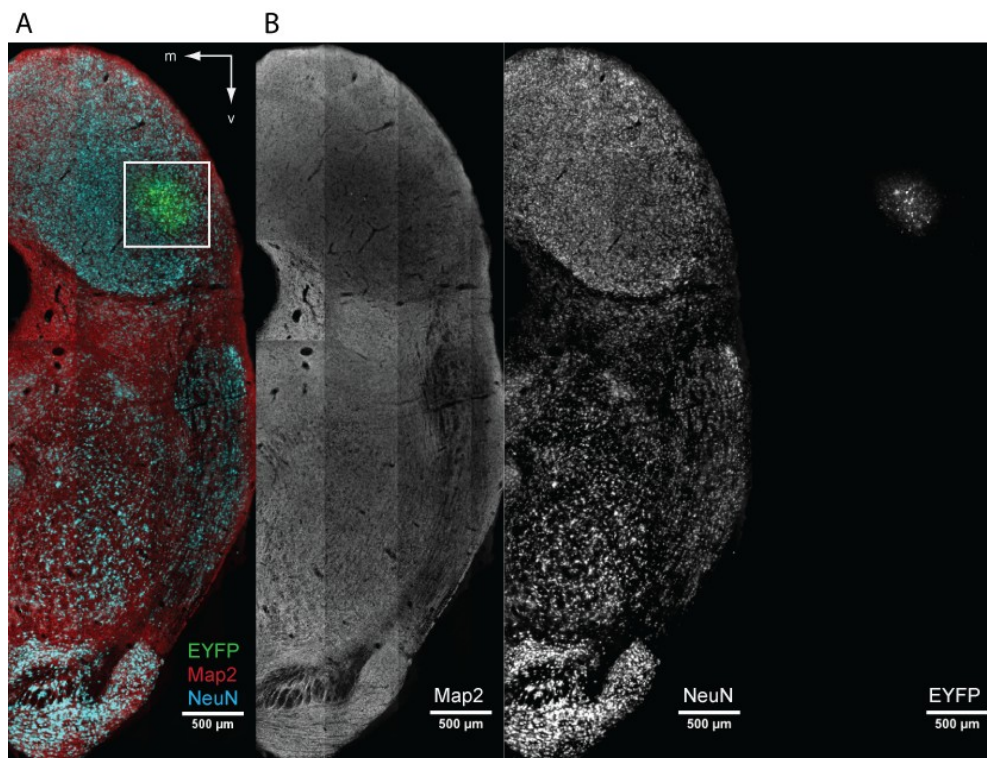
Figure 23: The *rAAV8YF* control vector injection into the IC drives *EYFP* expression in transduced neurons

A. The *rAAV8YF.hSyn.EYFP* vector transduces cells in the stereotactically targeted IC of a P28 animal and mediates expression of the control fluorophor *EYFP* after 21dpi. The picture shows a scan of a fixated, coronal brain section taken with the virtualSlide epifluorescence microscope. The area of transduction site is marked by a white rectangle. The green channel is the *EYFP* signal, the red channel is the *Map2* signal and the cyan channel is the *NeuN* signal. m=medial, v=ventral **B.** The individual fluorescence channels from the composite image in A. are shown. In the *EYFP* channel no off-target expression of the control fluorophor can be detected and the transduction is limited to the site of injection. In the *NeuN* channel bleaching from confocal scanning can be seen in the transduction area.

Gerbils of age P28-P60 were stereotactically injected with 250nl of *rAAV8YF.hSyn.EYFP* into the *IC* and sacrificed with a lethal dose of pentobarbital 7, 14, 21 and 28dpi after injection. The brains were retrieved after transcardial perfusion with 4% PFA, post-fixated over night and cut into 50µm thick coronal sections. Antibody immunohistochemistry for *Map2* and *NeuN* in parallel was used to conclusively identify both, neurons in higher magnification and the anatomical outlines of nuclei in lower magnification. With images from the virtualSlide epifluorescence microscope in low magnification (10x), the anatomical co-localisation of the injection site in the *IC* was confirmed (Figure 23). Success rate of stereotactical injection was at 100%, since in all experiments injection sites could be found in the *IC* (n=12). Outside of the injection site, no *EYFP* signal could be detected by retrograde transport to the *DNLL* or *SOC* (Figure 24). Anterograde labelling to the contralateral *IC* (Figure 24A.) or *MGB* (data not shown) could also not be detected by injecting *rAAV8YF* into the *IC*. Yet in some *IC* injection experiments (n=3/12)
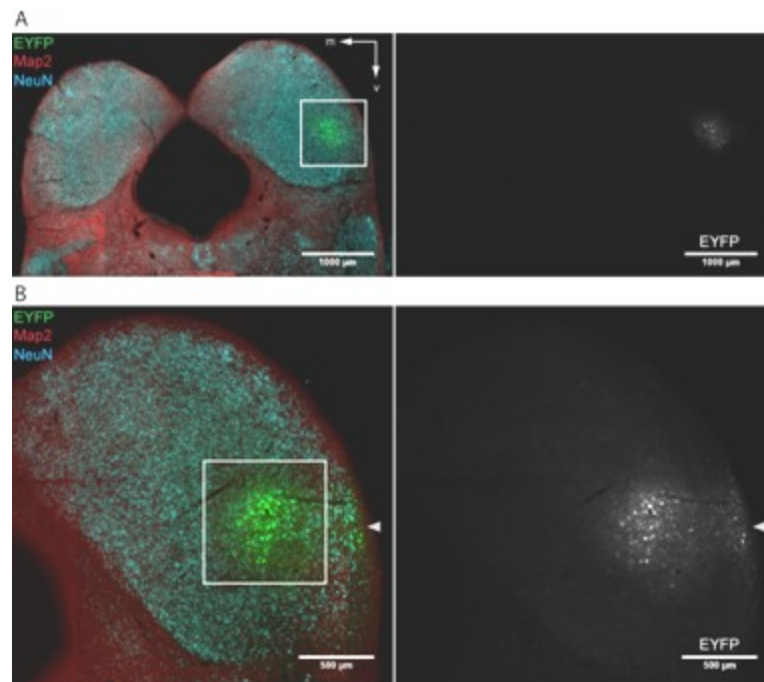
Figure 24: Transduction with *rAAV8YF* is limited to the site of injection in the IC

A.*EYFP* fluorescence is not observed in the IC contra lateral to the transduced area. The white rectangle highlights the site of rAAV injection. The isolated *EYFP* channel in the right panel shows only locally restricted fluorescence signal. m=medial, v= ventral. **B.** Injection of the control vector into the IC of another P28 animal shows transduced cells in the IC as well as in the ECIC close to the actual injection site after 21dpi. Grey triangles point towards the *EYFP* expressing cells in the ECIC. In **A** and **B** the green channel is the *EYFP* signal, the red channel is the *Map2* signal and the cyan channel is the *NeuN* signal.

transduction of the *ECIC* could be observed adjacent to the site of *rAAV* injection (Figure 24B). In projections of confocal z-stacks the presence of the cell filling *EYFP* was also detected along the axonal fibres coming from transduced *IC* cells and passing through the *commissure of Probst* and projecting to the contralateral hemisphere (data not shown). In the projections
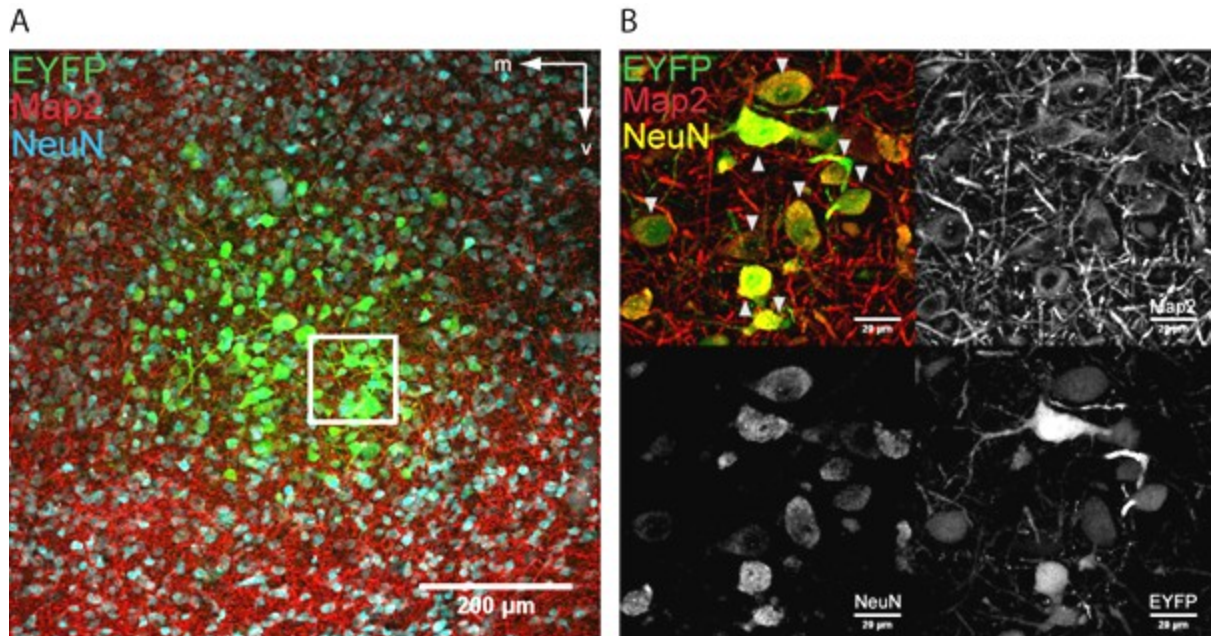
Figure 25: Co-localisation of neuronal markers and *EYFP* fluorescence in transduced cells.

A. Maximum projection of a confocal z-stack from a *rAAV8YF* injected IC 28dpi. The white rectangle marks the area for 63x magnification in B. The green channel is the *EYFP* signal, the red channel is the *Map2* signal and the cyan channel is the *NeuN* signal. m=medial, v=ventral. **B.** Maximum projection of confocal z-stacks in 63x optical magnification. All *EYFP* expressing cells are co-labelled with neuronal markers. Grey triangles point towards transduced cells. Notice that not all neurons in the field of view are transduced. The green channel is the *EYFP* signal, the red channel is the *Map2* signal and the yellow channel is the *NeuN* signal.

from confocal z-scans co-localisation of *EYFP* expressed by transduced cells and the neuronal markers *Map2* and *NeuN* was found in the overlay of these fluorescence channels. Co-localisation was observed in all the *rAAV* injections into the *IC*. This co-labelling revealed the exclusive neuronal transgene expression mediated by the *rAAV8YF* vector (Figure 25). As a negative control, a bolus injection of 250nl *rAAV* into the *IC* was carried out to inflict minor tissue damage and activate glial scar formation. After 14 and 21dpi the animals were sacrificed and transcardially perfused. The brains were retrieved, postfixated and sections cut. The sections were additionally immunohistochemical stained with anti-S100ß antibody to visualize glia cells. No co-localisation of *EYFP* and S100ß signal was detected (Figure 26). In 63x optical magnification it was apparent that not all neurons in the transduced area were actually transduced (Figure 25B) (for quantification see chapter 4.4). Nonetheless, these results recommended further experiments in the *IC* to quantify transduction efficiency. Also further experiments to test for neural specificity of *rAAV* transduction in

other auditory nuclei with the same promoter, vector backbone and capsid combination were carried out.
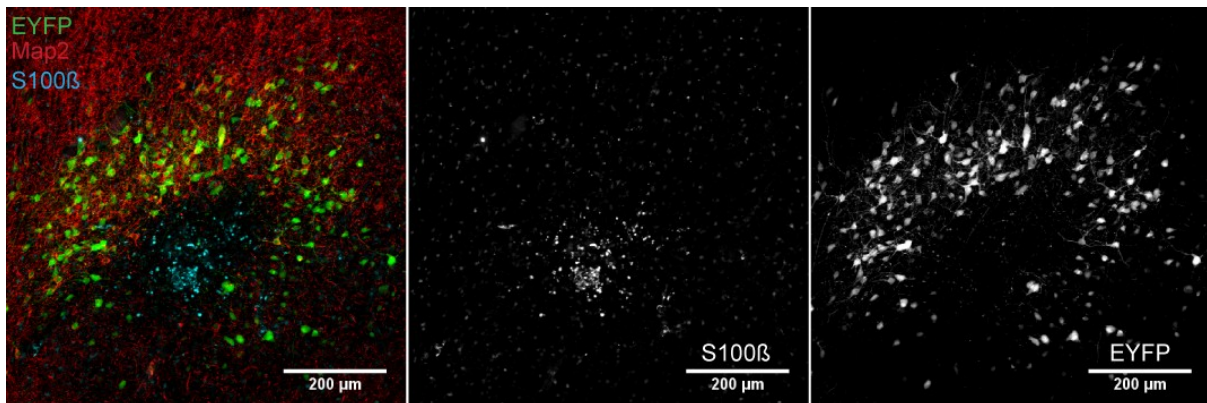
Figure 26: No glial expression of *EYFP* after rAAV control vector injection into the *IC*

21dpi after bolus injection of 250nl *rAAV8YF.hSyn.EYFP* glial cells were abundant at the center of injection and supplanted neurons. No co-localisation of glial marker and *EYFP* could be detected. Left panel shows overlaid sum projection of confocal z-stacks. The green channel is the *EYFP* signal, the red channel is the *Map2* signal and the cyan channel is the S100ß signal. The middle panel and the right panel show the individual channels for the S100ß signal and the *EYFP* fluorescence.

4.3.2. Injection into the Dorsal Nucleus of the Lateral Lemniscus (DNLL)

The *DNLL* represents another important target for optogenetical experiments. Therefore neuronal specificity of transduction with our *rAAV* control vector was tested. Again gerbils at the age of P28-P60 were stereotactically injected into the *DNLL* with 250nl of *rAAV8YF.hSyn.EYFP*. After an incubation period of 28dpi gerbils were sacrificed with a lethal dose of pentobarbital. Tissue was fixated by transcardial perfusion with 4% PFA, brains were retrieved and additionally post-fixated with 4 %PFA over night. Coronal sections of 50µm thickness were cut and immunohistochemistry with markers for *Map2* was performed to identifiy neurons. Images in the virtualSlide epifluorescence microscope were taken to localize anatomical position of the injection site (Figure 27A). The success rate of injections into the *DNLL* was lower compared to the *IC*. Roughly, only one third of
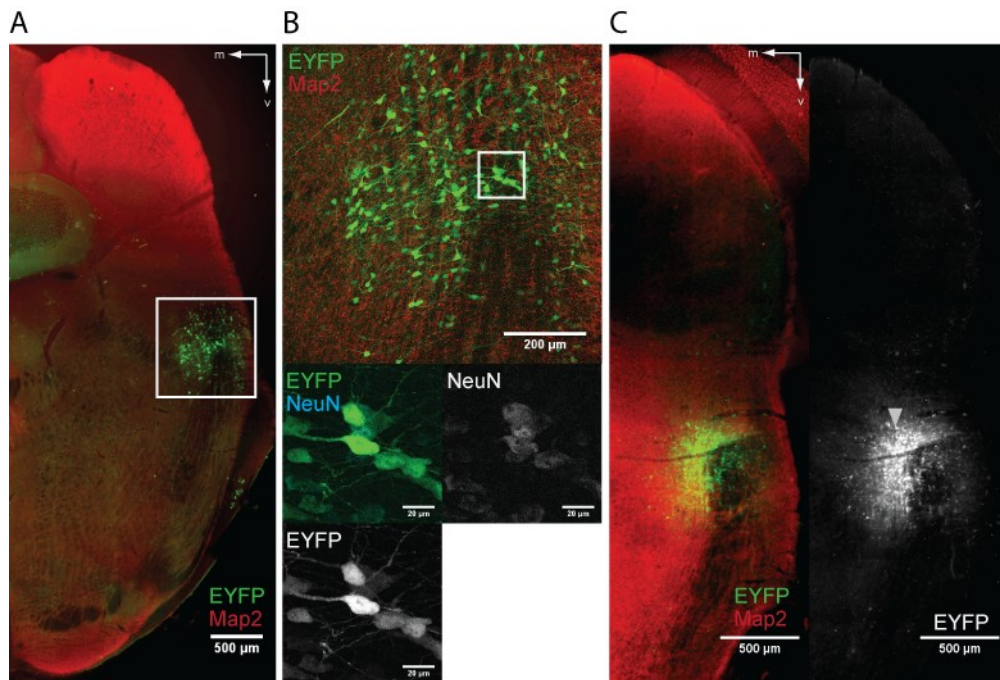
Figure 27: Stereotactical injection of *rAAV8YF* and neuronal specific expression in the *DNLL*

A. The site of injection and the *EYFP* fluorescence were localized in the *DNLL* but fluorescence was also detected in the neurons surrounding the *DNLL*. The white rectangle marks the site of transduction. **B**. The top panel shows transduced cells in the *DNLL* and surrounding area with 20x optical magnification and the lower panel depicts transduced neurons in 63x magnification. *EYFP* and *NeuN* fluorescence signal are co-localised in the overlay. The white rectangle encompasses the area shown in detail with 63x magnification below. **C**. Off target injection using identical coordinates: injection site was medial to the *DNLL*, nonetheless rAAV diffused into the *DNLL* and transduced cells. The grey triangle marks the medial offset of the injection capillary. m=medial, v=ventral. The *EYFP* fluorescence is the green, the *Map2* signal is the red, the *NeuN* channel is the cyan channel.

injections were on target and spill over and diffusion of *rAAV* into adjacent tissue were more frequently observed. Vice versa, on one hand an injection close (<100µm) to the *DNLL* also led to transduction of cells in the *DNLL* due to diffusion (Figure 27C). But on the other hand this deviation also decreased the transduction area in the *DNLL*. The *DNLL*'s smaller physical size, the long distance (~5,5mm from lambda) for injection and inter-individual differences in cranial anatomy limited stereotactical precision and efficiency. Again, the fluorescence channels of the *NeuN* signal and *EYFP* from confocal z-scans in 20x and 63x optical magnification were overlayed to determine co-localisation and therefore neuronal specificity of transduction (Figure 27B). All *EYFP* expressing cells were found to have a co-labelling with the neuronal marker *NeuN*. Similar to the quantification of transduced neurons in the *IC* (see chapter 4.4 for quantification in the *IC*), not all neurons in the transduction area were actually transduced, i.e. expressed *EYFP*.

4.3.3. Injection into the Medial Nucleus of the Trapezoid Body (MNTB)

Neural specificity of transduction was also tested for the *MNTB*. As in the experiments before, 250nl of *rAAV8YF.hSyn.EYFP* was stereotactically injected into the *MNTB* of P28-P60 gerbils. Gerbils were sacrificed with a lethal dose of pentobarbital after 21dpi and transcardially perfused with 4% PFA. Brains were retrieved, post-fixated over night and cut into 50µm thick coronal sections. In order to visualize neurons, anti-*Map2* antibody was used in the immunohistochemical staining procedure. Stained sections were scanned with 10x optical magnification in the virtualSlide microscope to assess anatomical position of the injection site. In the overlay of both channels, *Map2* and *EYFP* fluorescence, the area of transduction and the injection site could be referenced to the *MNTB* (Figure 28A). The success rate for on-target injections was roughly one hit in three experiments since the distance for the dorsally approaching injection capillary was already 8.2-8.4 mm in ventral direction from lambda. Locally limited diffusion of the virus and transduction of tissue surrounding the *MNTB* and close to the injection tract was also observed (Figure 28A). To assess the neuronal specificity of *rAAV2.1/8* transduction, maximum projections of confocal z-stacks with 63x optical magnification were generated and an overlay of both channels showed co-localisation of *EYFP* and the neuronal marker *Map2*. Again, all *EYFP* expressing cells co-expressed *Map2,* but not all neurons in the transduction area were expressing *EYFP* (Figure 28B). About 48 +/-18%

(n=2) of the *MNTB* neurons were transduced with a single injection of 250nl *rAAV8YF.hSyn.EYFP* into the *MNTB*.
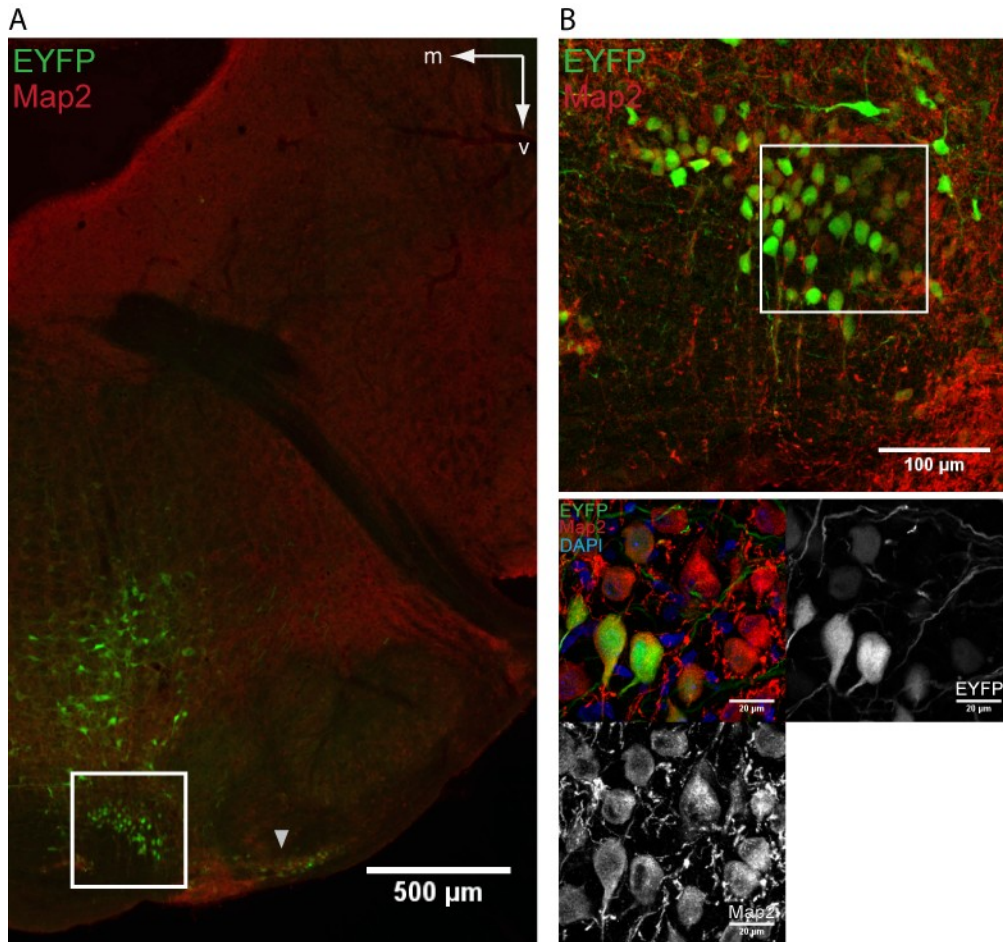
Figure 28: Stereotactical injection of *rAAV8YF* and neuronal specific expression in the *MNTB*

A. In the overlay of the *Map2* and the *EYFP* fluorescence channel the area of transduction and the injection site were localized in the *MNTB*. Diffusion of virus into the injection tract (above the white rectangle) and *LNTB* (grey triangle) resulted in detectable off-target transduction of neurons. The white rectangle marks the site of injection and encompasses the *MNTB*. The grey triangle points towards the off-target transduction of LNTB cells. **B.** In the maximum projection of a confocal z-stack with 20x magnification the transduced *MNTB* cells were clearly identified by their morphology. The white rectangle marks the area for the 63x optical magnification shown in the smaller panels below. The left middle panel shows the overlay of the *EYFP*, *Map2* and DAPI channel and the co-labelling of neuronal marker and *EYFP* fluorescence. Right middle panel and lower panel show the individual *EYFP* and *Map2* channels respectively. m=medial, v=ventral. The *EYFP* fluorescence is the green, the *Map2* signal is the red and DAPI is the blue channel.

4.3.2. Transduction efficiency and expression ratio increased over time

From the injection experiments into *IC*, *DNLL* and *MNTB* it was established that transduction of neurons with *rAAV8YF* vector was successful and indeed the small sized *hSyn* promoter exclusively drove neuronal specific expression. Therefore prerequisites 1) and 2) were met so far. Still, the observation that not all the neurons inside the transduction area were actually transduced needed a more quantified evaluation. Thus, point 3) and 4) from the prerequisites were addressed in the following experiments.

To determine the transduction efficiency, the number of transduced neurons and the total number of neurons inside the transduction area were counted for 1, 2, 3 and 4 weeks after injection in three biological replicates and at least five technical replicates per biological replicate. The *IC* of gerbils at the age of P28-P49 was injected with 250nl of the control *rAAV8YF.hSyn.EYFP*. The three biological replicates of each time point were all injected and subsequently processed on the same day in the same order and manner. Accordingly, animals were sacrificed with a lethal dose of pentobarbital and transcardially perfused with 4% PFA. After the brains were retrieved, postfixation overnight followed. Coronal sections of 50µm thickness were cut and immunohistochemistry with *Map2* and *NeuN* markers was carried out to label neurons. The volumes of the transduced *IC* sections were confocally scanned with 20x optical magnification (Figure 29A). Transduction area was measured by thresholding mean intensity for each section (Figure 29B). One biological replicate for the 3wpi time point had also *EYFP* expression along the injection tract. This area was also included for all measurements since it still belonged to the *IC*. Despite the enlarged transduction area in this case, the relative measurements and calculations stayed consistent with all other biological samples. In the sum projection of the confocal z-stacks, transduced neurons and total neurons inside the transduction area were then quantified (Figure 29C). Including all time points, in total 32369 neurons and 17579 transduced neurons were manually counted. When the transduction area was normalized to transduced or total neurons, total (including transduced) neurons occurred roughly twice as often in the same area as transduced neurons for all biological replicates and all time points (Figure 29D). This is consistent with the transduction efficiency, the ratio of transduced neurons to the total number of neurons inside the transduction area. At all four time points roughly half of the neurons inside the injection area were transduced, with a slight improvement at the later time points (1wpi= 47%, 2wpi=54%, 3wpi=53% and 4wpi=59% on average transduced; total average of 54% transduction efficiency over all time points). The biological replicates belonging to the same time point showed no significant variation, also percentages for all time points were not significantly different over time (Figure 29E). To quantify expression levels over time the
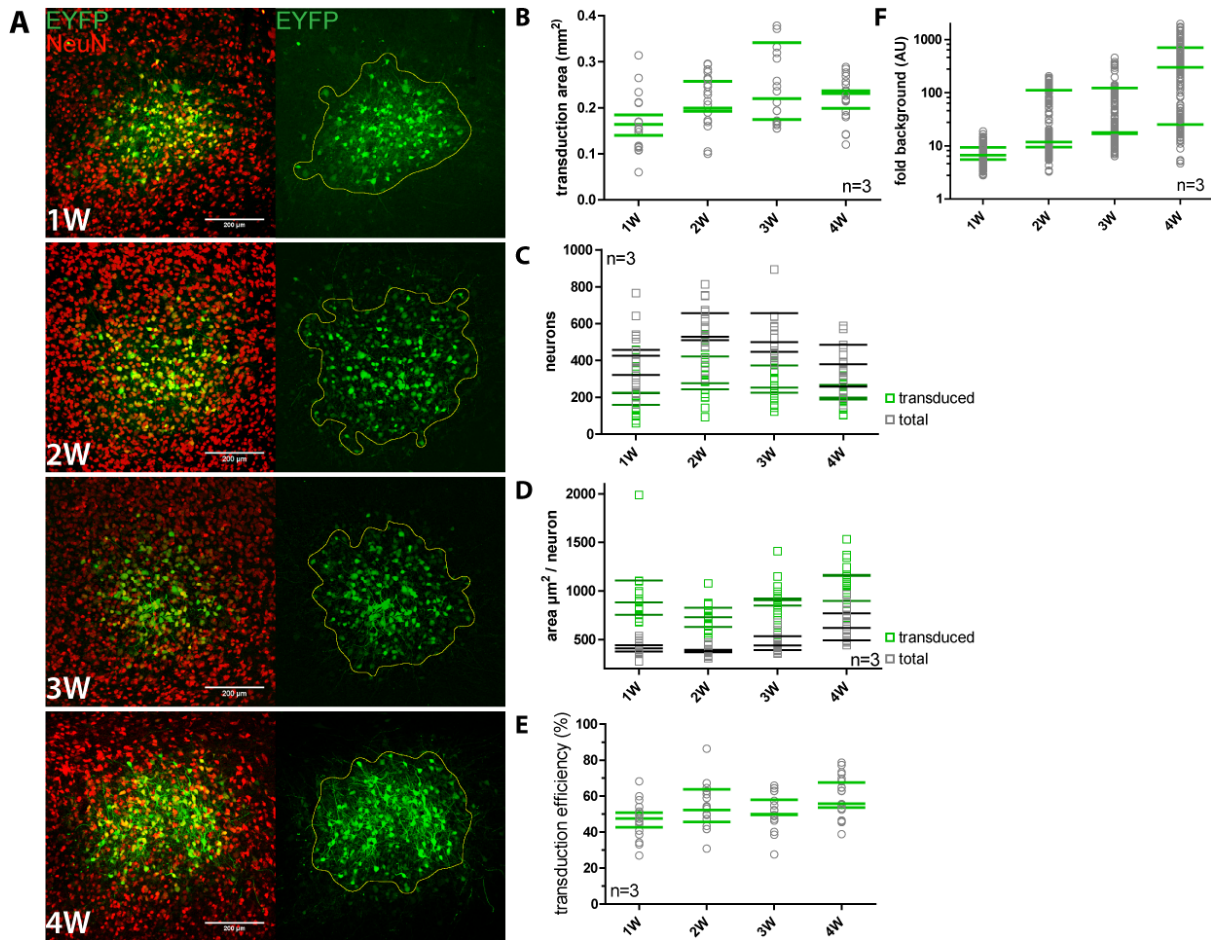
Figure 29: *rAAV8YF* transduction efficiency and expression ratio over 4 weeks after injection

A. From top to bottom: example images from each time point 1,2,3 and 4 weeks after *rAAV* injection into the IC. Left images show the overlay from maximum projections of confocal stacks from the *EYFP* (green) and *NeuN* (red) channel. Images on the right show the sum projection from confocal stacks in the according *EYFP* channel and the yellow outline of the calculated transduction area. Note that decreasing background noise from top to bottom is already apparent with the bare eye. **B.** The measured transduction area from all replicates is shown (grey circles). The sampled transductions areas were comparable for all time points, but average sizes slightly increased over time. Green horizontal strokes mark the mean value for each biological replicate. **C.** Shown is the number of transduced (green squares) and total neurons (grey squares) for all replicates. Green and grey horizontal stroke mark the mean number of transduced or total neurons respectively, for each biological replicate. **D.** Shown is the calculated area per transduced (green square) or for the total number of neurons (grey square) for each replicate. Green and grey horizontal stroke mark the mean area per transduced or non-transduced neuron respectively for each biological replicate. **E.** Shown is the transduction efficiency (%), i.e. percentage of transduced neurons inside the transduction area for each replicate (grey circle). See Methods section for details. The average percentage for each biological replicate is marked by a green horizontal stroke. **F.** Signal to noise ratio is significantly increasing with time. SNR is plotted as "fold background" in arbitrary units (AU) for each replicate (grey circles). Note the logarithmic scaling of the y-axes. Green horizontal strokes mark the average SNR for each biological replicate. 1W, 2W, 3W and 4W= 1, 2, 3 and 4 week(s) after injection

signal to noise ratio (SNR) in the form of multiples of the background fluorescence ("fold background") was measured. For each biological replicate the average *EYFP* intensity of 52 cells was measured in the sum projection of a

confocal z-stack. The SNR in fold background arbitrary units (AU) was significantly increasing over time with the highest values and highest dynamics at four weeks after injection (Figure 29F).

Summary

The results from the antibody stainings indicated that prerequisites 1-4) were met and neuron specificity of transgene expression was achieved in all tested auditory nuclei. Expression of *EYFP* was already detected one week after injection. At and around the injection site around half of the neurons were transduced. Longer expression times resulted in higher expression levels and increased number of transduced neurons.

4.4. Electrophysiological characterization of *CatCH* and *NpHR3*.0 in auditory neurons

In order to evaluate the aptitude of the channelrhodopsins to excite and halorhodospins to inhibit transduced neurons whole-cell patch-clamp recordings in current clamp and voltage clamp mode were performed. Thereby point 5 of the prerequisites could be answered. The outcome of the *in vitro* recordings was the determinant for follow-up *in vivo* experiments.

4.4.1. *In vitro* patch-clamp recordings

Optical stimulation experiments were performed to elicit either excitatory or inhibitory responses. Measuring the photostimulated responses confirmed the correct and functional expression of the transgenes as well as correct intracellular trafficking to the cellular membrane on one hand. On the other hand the effectiveness of the optical stimulation could be determined. Effective optical excitation was considered as each light pulse elicits one action potential. Effective optical inhibition was considered as a light pulse suppresses action potentials. Frequency of light pulses, the light pulse width and light intensity or power were the dependent parameters of optical stimulation. The temporal precision of the cellular responses in effective light stimulation was also quantified.

For all *in vitro* experiments animals at the age of P0-P30 were injected with *rAAV8YF vectors.* Animals were sacrificed after 10-28dpi, brains retrieved and cut into coronal sections of 150-200µm thickness.

4.4.2. Eliciting action potentials with *CatCH*

To depolarize the neurons with blue light (470nm) *rAAV8YF.hSyn.CatCH.mcherry* vector was injected into the *IC* and into the *MNTB* (Figure 30A&D). The drugs *AP-5* and *DNQX* were applied to the extracellular recording solution in order to block of glutamatergic transmission. Transduced neurons were visually identified by their *mcherry* fluorescence (610nm) (Figure 30G). The fluorescence pattern was spotted and concentrated at the plasma membrane (Figure 30A&D). Transduced neurons were patched and at first optical stimulation protocols were executed in current clamp to test for light sensitivity. 470nm light pulses at frequencies from 5-100 Hz were presented, with varying pulse widths (min. 40µs - max. 95ms width) but 100%

light power. For 11 of 21 recorded cells, action potentials could be elicited with
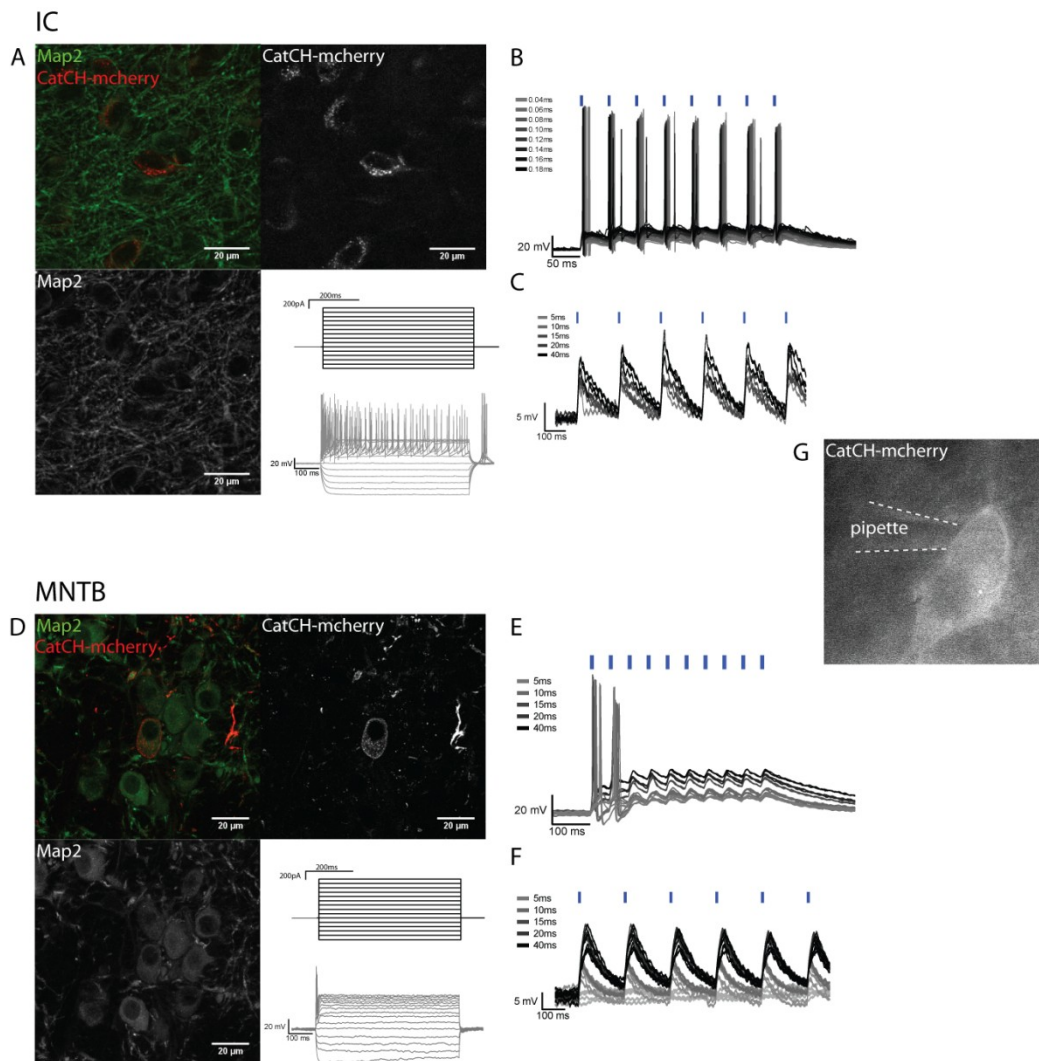
Figure 30: Transduced neurons expressing *CatCH-mcherry* in the *IC* and the *MNTB* could be depolarized with blue light

A. Maximum projections from a confocal z-stack showing transduced neurons in the IC expressing *CatCH-mcherry*. Note the clustered fluorescence pattern. Green fluorescence corresponds to the *Map2* signal and the red fluorescence to *CatCH-mcherry*. The right and lower left panel show the individual channels of the coloured overlay. The lower right panel shows the voltage traces of an photosensitive IC neuron in response to 15 current steps (from -500 to +900pA). **B.** Shows the voltage traces of an IC neuron firing when stimulated with light pulses of varying pulse widths (40µs-180µs) at 20Hz. **C.** Voltage traces of an IC neuron stimulated at 5Hz with light pulses of different widths (5-40ms) show only subthreshold responses. **D.** Maximum projections from a confocal z-stack showing transduced neurons in the *MNTB* expressing *CatCH-mcherry*. Green fluorescence corresponds to the *Map2* signal and the red fluorescence to *CatCH-mcherry*. The right and lower left panel show the individual channels of the coloured overlay. The lower right panel shows the voltage traces of an photosensitive *MNTB* neuron in response to different current steps (from -500 to +900pA). **E**. The picture shows voltage traces of an *MNTB* neuron firing when stimulated with light pulses of varying pulse widths (5-40ms) at 20Hz. **F.** Voltage traces of a *MNTB* neuron stimulated at 5Hz with light pulses of different widths (5-40ms) show only subthreshold responses. **G.** The picture shows the patch pipette accessing an IC neuron displaying *mcherry*-fluorescence. **B,C,E,F**: Blue strokes above voltage traces indicate the number and onset timing of the light pulses. Width of blue strokes is not to scale but enlarged for better visibility.

optical stimulation (Figure 30B&E). In the remaining neurons, only subthreshold depolarisations were recorded (Figure 30C&F) despite low frequency photostimulation (5Hz) that allows for longer pulse widths. For the latter neurons, light pulses exceeding 40ms width were not tested, though in principle longer illumination could have triggered action potentials since APs could be evoked with current injections. The next tested protocols included injection of current steps (-500pA to +900pA in 100pA steps) to characterize the neurons firing pattern (Figure 30A&D, lower right panel) and injection of smaller current steps to characterize passive membrane properties. Frequently, not all stimulation protocols and combinations of light pulse widths and frequencies could be acquired for each cell, due to its expiration during the recording. The success i.e. efficiency of photo stimulation was analyzed by counting the evoked spikes whereas any additional evoked spikes were counted as extra spikes. The pulse widths and the achievable upper frequencies for effective photo stimulation differed for each cell.

The first spike in the light pulse train was chosen for comparison due to absence of any spike history from preceding spikes (Figure 31A&B). In general, longer light pulse widths were more efficient but elicited also more extra spikes (Figure 31C&D). The shortest achievable spike latencies also differed from cell to cell. Commonly, spike latencies became shorter for longer light pulses and longer for shorter light pulses (Figure 31E&F). To quantify temporal fidelity jitter of photostimulated spikes was calculated. Jitter of light evoked spikes was in the range of (sub-)milliseconds (from 0.14ms up to 9.8ms jitter). In general, jitter decreased with longer pulse widths (Figure 31G&H). Spike latencies of the first and succeeding spikes did not differ significantly and average spike latency was 12.9ms +/-6.6ms SD for the first spike (n=9) and 14.0ms +/-7.2ms SD (n=10) for succeeding spikes (Figure 32A). From cell to cell the latencies for the 1st spike and all succeeding light evoked spikes was variable, i.e. sometimes succeeding spikes had shorter latencies sometimes longer latencies than the first light stimulated spike (Figure 32B). Those differences in latencies of elicited action potentials within light pulse trains are equivalent to phase shifts of action potentials. When latencies were averaged across all tested conditions of each cell including the latencies for the shortest and longest applied light pulses, the shortest measured latency for the first spikes was 2.3 ms for light pulses of 20ms width at 5Hz frequency and by far the longest was 32.7ms measured for a 5ms wide light pulse at 10Hz. Hence, there are phase differences in latencies of elicited action potentials between transduced neurons. To narrow down the parameter for efficient photostimulation, membrane resistance was calculated and plotted against average latency for the first spikes across all tested conditions to look for facilitation towards higher resistances. Yet no correlation between membrane resistance and fast photostimulation was found (Figure 32C). Another measure of temporal alignment of spikes is vector strength. To look for resonance effects that would

allow more precise spiking at certain light pulse frequencies, vector strength was calculated for a range of frequencies and pulse width. Under the presumption that a resonance was present, stimulating at the according resonance frequency would be more efficient. Yet, the dominant factor for temporal precision rather turned out to be light pulse width and facilitation due to resonance at any of the tested frequencies could not be observed (data not shown).

Summary

The point number 5 of the prerequisites was successfully met as shown by the *in vitro* electrophysiological characterization of *CatCH*. The *rAAV* vectors were able to confer functional and neuronal specific expression of channelrhodopsin after 10dpi already in sufficient levels to elicit action potentials when stimulated with blue light. Though, in some neurons even after 28dpi expression levels of channelrhodopsins did not suffice to depolarize the cell above action potential threshold when photostimulated. But still the photosensitivity was present and could be detected. The success of photostimulation was largely dependent on the amount of photons over time, i.e. pulse width in the current experiments. Unfortunately, not all light stimulation protocols could be tested for every neuron. The temporal fidelity of photostimulation for excitation did not match the high temporal precision of sensory responses in the auditory system. Therefore, photostimulation with *CatCH* for *in vivo* experiments was only advisable if temporal precision in the µs range did not play a critical role. Yet light activation in the range of several ms is possible.
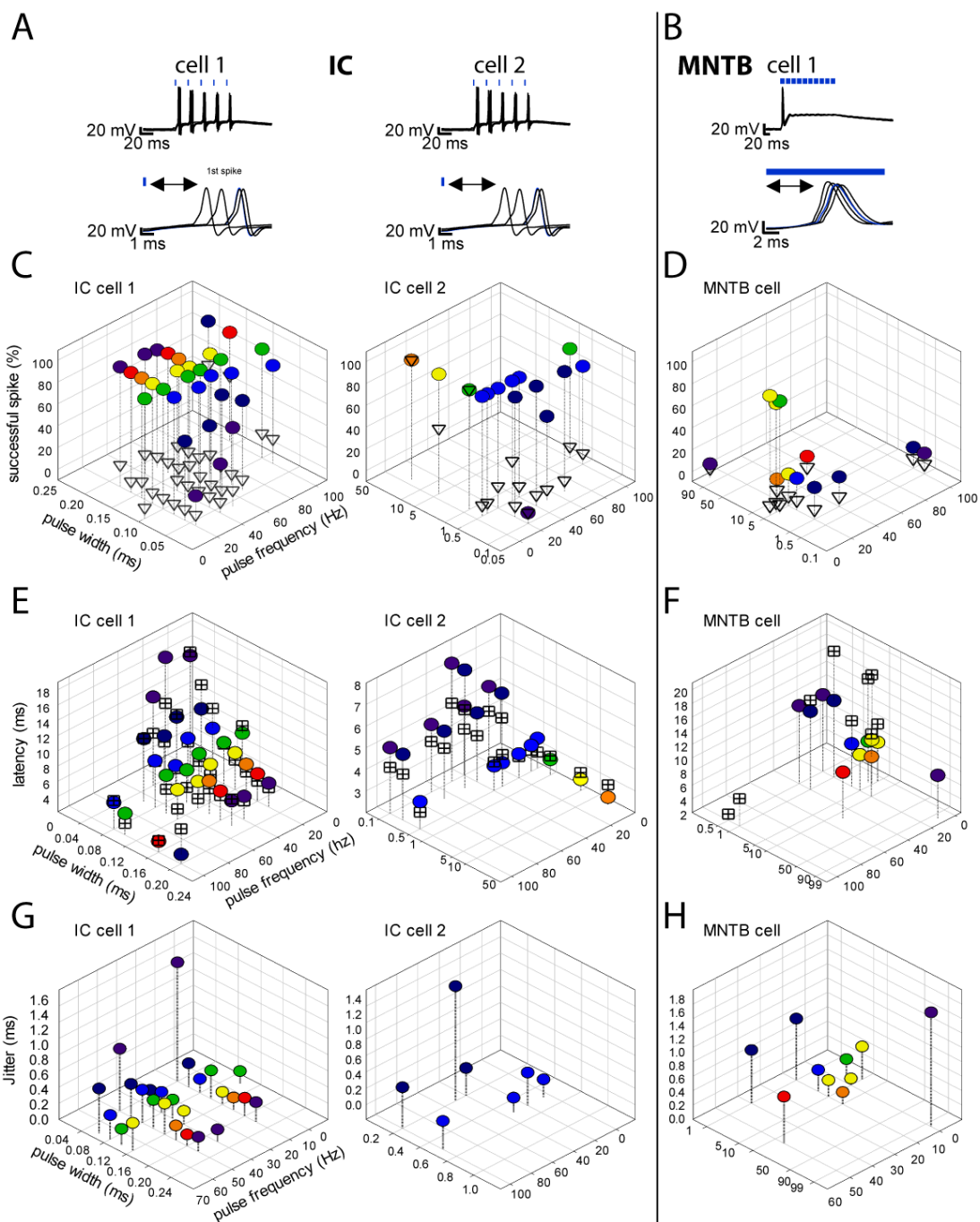
Figure 31: Efficiency of photostimulation, spike latencies and jitter of elicited APs in three exemplary neurons from IC and MNTB.

A. Overlay of voltage traces (5 trains) of two photostimulated IC neurons at 50 Hz light pulse frequency. Lower panels show the 1st spikes of each pulse train in the top panel. **B.** Voltage traces (5 trains) of a photostimulated *MNTB* neuron at 50Hz pulse frequency. Lower panel shows the 1st spikes of the pulse train. **A.,B.** Blue strokes above the traces indicate the number and onset timing of the light pulses. **C.,D.** Panels show the reliability of photostimulation in percent (%) over a range of pulse widths (IC cell 1: 0.04ms-0.2ms; IC cell 2: 0.1ms-20ms; *MNTB* cell: 0.5ms-95ms) and pulse frequencies (5-100Hz). Coloured circles represent the amount of successfully stimulated spikes within pulse trains (0-100%). Empty triangles represent the amount of extra/excess spikes due to photostimulation (%). **E.,F.** Latencies over a range of pulse widths (IC cell 1: 0.04ms -0.2ms; IC cell 2: 0.1ms-20ms; *MNTB* cell: 0.5ms-95ms) and pulse frequencies (5-100Hz).Coloured circles represent the latencies of the first photostimulated spike and crossed squares show the average latencies of all succeeding spikes within pulse trains. **G.,H.** Jitter over a range of pulse widths (IC cell 1: 0.04ms-0.2ms; IC cell 2: 0.1ms-20ms; *MNTB* cell: 0.5ms-95ms) and pulse frequencies (5-100Hz). Coloured circles represent the jitter of the first photostimulated spike in the pulse train.
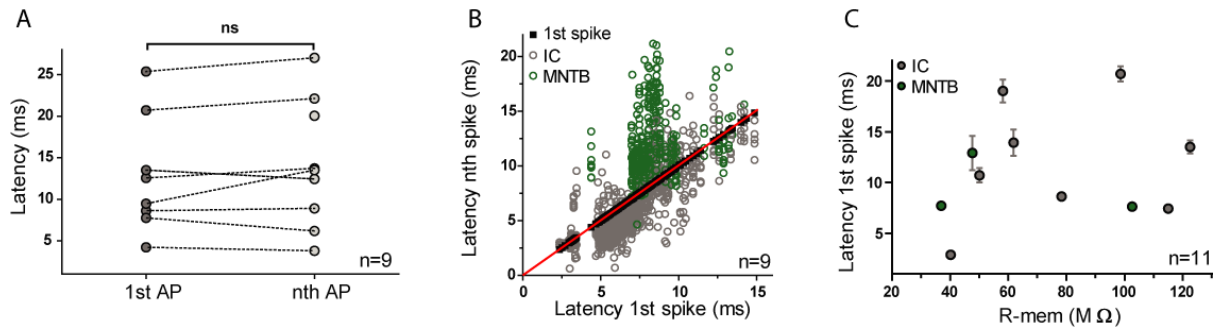
Figure 32: Pooled latencies of light evoked spikes in transduced neurons in the IC and MNTB

A. Comparison of light evoked first spikes and succeeding spikes averaged across all conditions for each cell (n=9 neurons total; IC=6 neurons; MNTB=3 neurons). There is no clear trend for speeding up or slowing down in spike latencies between the first and the following light stimulated spikes. Grey circles represent the first spikes in the light pulse train and light grey circles represent the succeeding spikes of the train. **B**. Latencies of all light evoked spikes plotted against the first spike on the x-axis and succeeding spikes on the y-axis. Black squares represent the 1st spike and empty circles represent succeeding spikes (grey=IC (n=6 neurons), green=*MNTB* (n=3 neurons)). A red regression line represents the fit to the first spikes. All succeeding spikes above the regression line had longer latencies whereas the spikes beneath the regression line had shorter latencies than the first spikes. **C**. The averaged latencies of the first spike across all tested condition plotted against the cell's input resistance (R-mem). No correlation of latencies with input resistance was found (n=11 neurons total; IC (grey) =8n; MNTB (green) =3n). The error bar corresponds to the standard deviation of the first spike's latencies (=jitter).

4.4.3. Evoking inhibitory currents and suppressing spikes with *NpHR3.0*
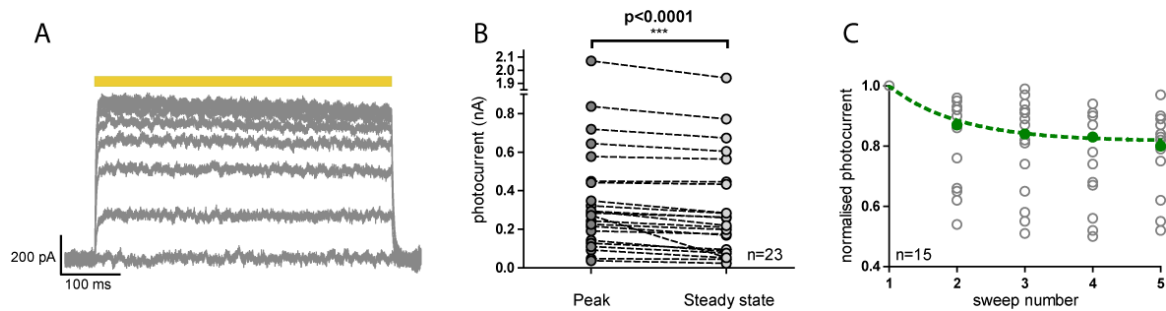
Figure 33: Light evoked currents in transduced *IC* and *MNTB* neurons expressing *NpHR3.0-EYFP*

A. Current traces of a transduced *IC* neurons responding to a 500ms yellow light pulse (yellow bar) with increasing light power in 10% steps. Note the photocurrent rundown from onset of the light pulse until the end. The evoked photocurrents saturated after reaching 50% light power. **B**. Pooled photocurrents (n=23) from all recorded *IC* (n=15) and *MNTB* (n=8) neurons in response to maximal light power. Grey circles correspond to the peak current and light grey circles correspond to steady state photocurrent. Due to photocurrent rundown steady state current was always lower than peak current. **C**. Grey circles correspond to the photocurrent normalized to the current of the first light pulse of five sweeps. The light elicited current decreased with each repetition. Green dashed line represents the exponential fit to the current rundown and green, full circles represent the median of the normalized photocurrents.

In order to suppress action potentials and hyperpolarize transduced cells with yellow/orange light (590nm), *rAAV8YF.hSyn.NpHR.EYFP* was injected into the *IC* and *MNTB*. Again *AP-5* and *DNQX* were applied to the extracellular recording solution to block glutamatergic transmission. Transduced neurons were first identified by their *EYFP* fluorescence and then patched. Yellow light pulses of 500 ms duration were presented with increasing intensity and the photocurrent was recorded in voltage clamp mode (Figure 33A) whereas the hyperpolarization of the membrane potential was recorded in the current clamp mode (Figure 35Figure 34D). The measured photocurrent exhibited rundown during stimulation due to depletion of 11-cis-retinal by photo conversion. From total 23 recorded cells in the *IC* (n=15) and *MNTB* (n=8) the average peak photocurrent was 390pA +/-424pA SD whereas the slightly lower steady state current was 344pA +/-408pA SD for the maximal light power (6.2mW/mm^2) at the level of the acute slice (Figure 33B). Rundown of photocurrent did occur between repetitions and when normalizing the photocurrent to the first sweep the current decayed with each succeeding repetition. Yet the photocurrent rundown was slowing down for each subsequent sweep and was steepest for the first repetition (Figure 33C). When the light power was increased, the photocurrent started to saturate after reaching half maximal light power. The average gain in photocurrent from 90% to 100% light power (100% ≡ 6.2mW/mm^2) was minimal (<+2%) (Figure 34A). As a next step the time
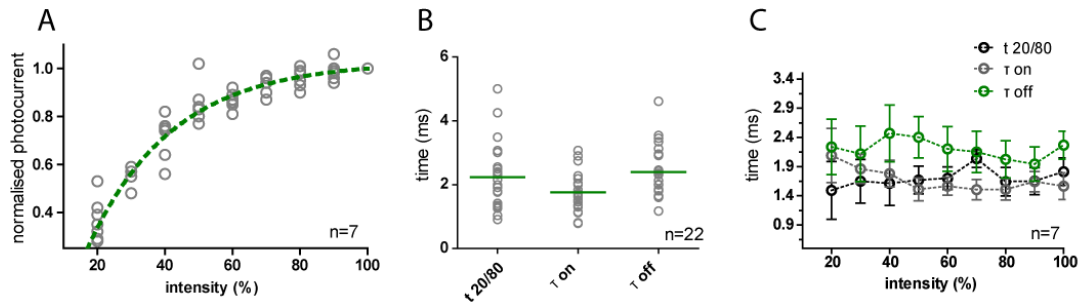
Figure 34: Light power dependency and photocurrent kinetics of NpHR3.0

A. Grey circles represent the photocurrents normalized to the response to the maximal light power. Green dashed line represents the exponential fit to the increasing photocurrents. **B.** Grey circles represent the calculated values for $t_{20/80}$, τ_{on} and τ_{off} for the measured photocurrents at maximal light power. Green horizontal strokes indicate the mean value. **C.** The parameters describing the current kinetics were calculated for each intensity step. Dark grey circles represent $t_{20/80}$, light grey circles represents τ_{on} values and green circles represent τ_{off}. Error bars indicate the standard deviation.

constants for the on and off kinetics of the photocurrent were calculated by fitting exponential functions. Since some of the recordings had noise perturbations at 50Hz from the AC of mains supply also the rise time ($t_{20/80}$) from 20% to 80% of the peak photocurrent was measured as an alternative parameter less affected by the noise. For the maximal light power the average τ_{on} was 1.7ms +/-0.6ms SD, the $t_{20/80}$ was 2.2ms +/-1ms SD and the current decayed with τ_{off} 2.4ms +/-0.8ms SD (Figure 34B). In a next step these kinetics were tested for light intensity dependency. Plotting τ_{on}, $t_{20/80}$ and τ_{off} for all tested intensities revealed their independency on light level (Figure 34C).

The cell's current threshold to fire an action potential was determined. Afterwards the cell was stimulated at a frequency of 10Hz with a train of current injections 10% above the determined action potential threshold and simultaneously light pulses with varying widths were presented to suppress spikes or even precisely suppress exactly one single spike within the train. When the light pulse preceded the current stimulation but ended right before the current injection so that there was no overlap, suppression of spiking was not effective (Figure 35A). Single spike suppression with light worked in only 1/5 tested cases and was less efficient than suppression of a spike train. In most cases the spike suppression with light worked best when the light pulse comprised the targeted spikes completely, started several milliseconds before the first spike and outlasted the current stimulation (Figure 35B). Photosuppression with *halorhodopsin* frequently led to postinhibitory rebound spikes due to the hyperpolarisation of the membrane potential and therefore resulted in unwanted extra spikes (Figure 35C&D).
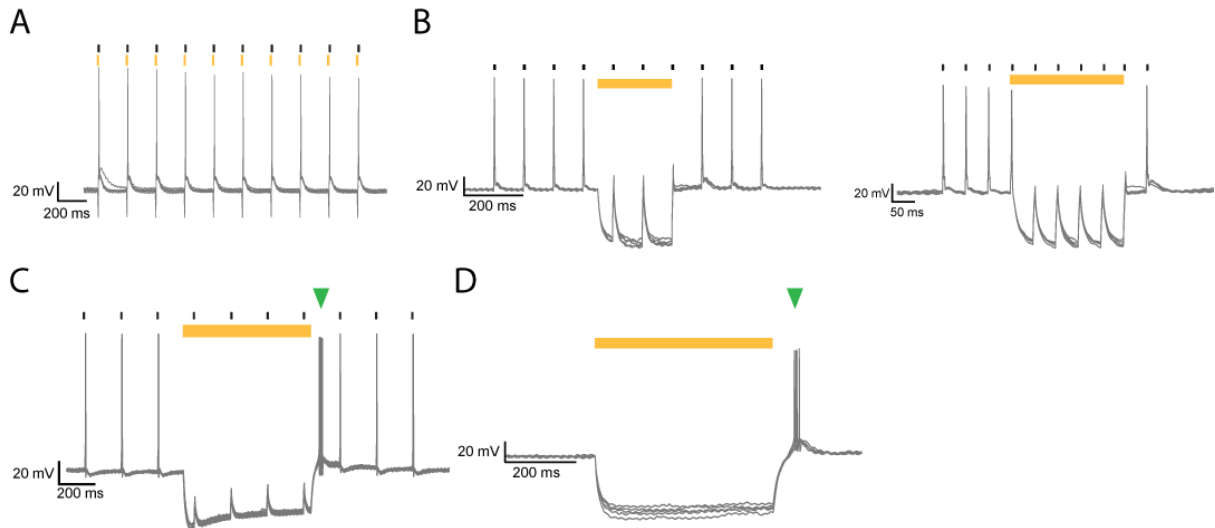
Figure 35: Suppression of spiking with light and evoked postinhibitory rebound spikes

A. Overlay of voltage traces of a transduced, *NpHR3.0-EYFP* expressing *IC* neuron when stimulated with current injections (black strokes) right after 5ms long light pulses (yellow strokes) at 10Hz. The neuron hyperpolarizes in response to the light pulses but fires a spike upon the current injection nonetheless. **B.** A transduced *IC* neuron was spiking when stimulated with current injections (black strokes) at 10Hz (left panel) or 20Hz (right panel) and a 200ms light pulse (yellow bar) effectively suppressed spiking in response to current injection. **C.** Current evoked (black strokes) spiking is suppressed in a transduced *MNTB* neuron during a 250ms light pulse (yellow bar). But after cessation of the light pulse an extra spike (green triangle) is elicited. **D.** An *IC* neuron expressing *NpHR3.0-EYFP* hyperpolarizes to -110mV in response to a 500ms light pulse (yellow bar) but spikes (green triangle) right after the end of the light pulse.

Summary

Expression of functional halorhodopsin was neuron specific in the *IC* and *MNTB*. The expression levels after 10dpi were already sufficient to inhibit spiking, in some cases even down to single spike precision. Elicited maximal photocurrent did vary a lot from cell to cell. Rundown of photocurrent did not pose a critical parameter for *halorhodopsin* application. For an *in vivo* application the light pulse would be most efficient when comprising and especially preceding the whole sensory stimulus.

4.5. Applying *NpHR3.0* to *in vivo* extracellular recordings

With the results of the immunohistochemical and *in vitro* experiments all previously mentioned prerequisites were met. Parameters (light pulse width and pulse timing) for efficient photostimulation with *CatCH* and effective optical silencing with *NpHR 3.0* were determined in the *in vitro* patch-clamp experiments. Expression times of at least 4 weeks post *rAAV8YF* injection were initially chosen to allow high expression levels of *NpHR3.0*.

The *IC* was targeted for initial *in vivo* experiments due to technical reasons like its dorsal position (only ~3.9mm ventral from lambda) and its physical size but also because its neurons' firing patterns upon auditory stimulation are well described. Short insertion distances of the optical fibre into the tissue as well as the possibility to inject *rAAV* vectors into several sites in the *IC* helped to reduce possible stereotactical errors and increase experimental efficiency.

The *DNLL* was the main experimental target for *in vivo* optogenetical experiments in order to elucidate its role in the phenomenon of precedence. As laid out in the introduction (see chapter 1.3 for details), profound hypotheses about the precedence effect can be assessed by manipulating the *DNLL* with light. Technically, the insertion of the optical fibre, the injection of the *rAAV* vectors and the positioning of the recording electrode were more demanding than for the *IC*.

In a first step the light delivery into the transduced areas had to be established. Also in the same step, *in vivo* evidence for an actual impact of channelrhodopsin/*halorhodopsin* on the firing behavior of stimulus responding neurons in the brainstem of the *Mongolian Gerbil* was yet to be collected. Therefore, extracellular potentials of *halorhodopsin* expressing neurons in the *IC* and *DNLL* of anaesthetized animals were recorded while presenting broadband noise stimuli and pulsed light simultaneously. This first proof of principle experiments were extremely important not only to establish optogenetic methods and confirm their effectiveness *in vivo* but also to estimate the effect size of the optical manipulation on stimulus evoked responses. Only in a next step, the ipsilateral *DNLL* can be optogenetically manipulated and the impact on PI can be measured with recordings of extracellular potentials in the contralateral *DNLL*.

4.5.1. Establishing *in vivo* photostimulation with optical fibres
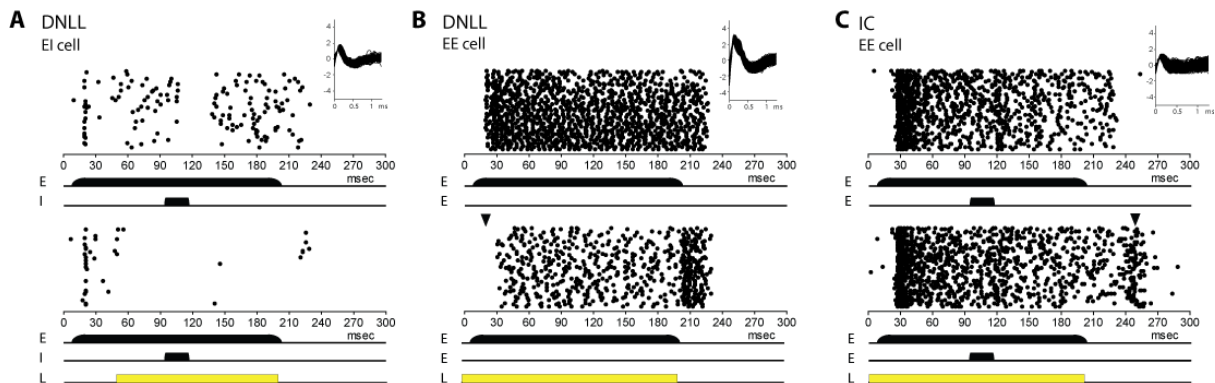
Figure 36: Effect of photosuppression on three exemplary cells extracellularly recorded in the *DNLL* and *IC*.

A. Shows an extracellular recording in the form of a peristimulus time histogram (PSTH) from a transduced *DNLL* (EI) neuron. Upper panel shows the response to binaural stimuli: a 200ms noise stimulus (long black bar) was presented to the excitatory ear (E) and a 20ms noise stimulus (shorter black bar) was presented to the inhibitory ear (I). Note the persistent inhibition during and after the noise presentation to the inhibitory ear. Inset in the upper right corner shows the spike shapes. Lower panel shows the PSTH from the same neuron and with the same auditory stimulation as above but with an additional 150ms light pulse (yellow bar) triggered at millisecond 50. **B**. Shows an extracellular recording in the form of a PSTH from another *DNLL* neuron (EE). Upper panel shows the response to a monaural stimulus: a 200ms noise stimulus (long black bar) was presented to the excitatory ear (E). Inset in the upper right corner shows spike shapes. Lower panel shows the PSTH from the same neuron and with the same auditory stimulation as above but with an additional 200ms light pulse (yellow bar) triggered at millisecond 1. Black triangle indicates the timing of the first spikes in the control condition. Note that the onset of the response to the auditory stimulus is delayed in the light condition. **C.** Shows an extracellular recording in the form of a PSTH from an IC neuron (EE). Upper panel shows cell's response to binaural stimulation. Inset in the upper right corner shows spike shapes. A 200ms noise stimulus (long black bar) was presented to the contralateral ear (E) and a 20ms noise stimulus (short black bar) was presented to the ipsilateral ear (E). Lower panel shows the PSTH from the same neuron and with the same auditory stimulation but with an additional 200ms light pulse (yellow bar) triggered at millisecond 1. The neurons fires (black triangle) 40ms after the light pulse.

To test the feasibility of light delivery with optical fibres and the achievable extent of excitation and suppression in vivo, *rAAV8YF.hSyn.CatCH.mcherry.T2A.NpHR3.0* or *rAAV8YF.hSyn.NpHR3.0.EYFP* were injected into to *IC* or *DNLL* of >P28 animals. After the first trials, transduction area was maximized by three consecutive virus injections instead of only one. This had the disadvantages of increased off-target transduction but increased chances to transduce a larger volume of the *DNLL* as well. The off-target transduction would only affect the *IC*, the auditory nucleus directly downstream of the *DNLL*. Therefore extracellular recordings from the ipsi or contralateral DNLL would not be affected. As in previous experiments, both *rAAV2.1/8* vectors transduced cells
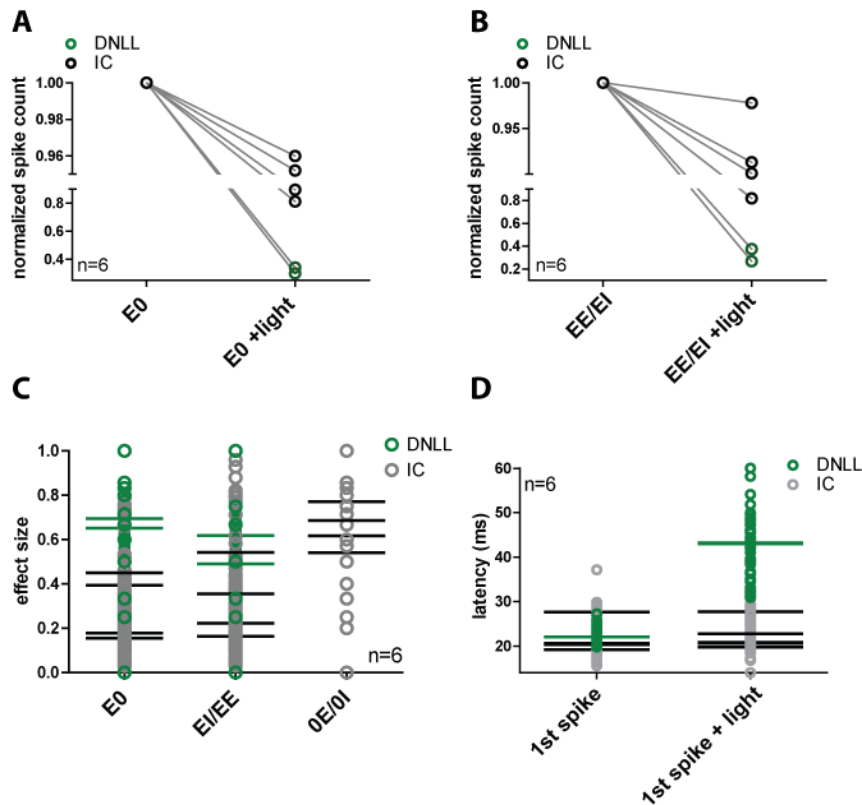
Figure 37: Normalized spike counts, effect sizes and first spike latencies in photosuppression in vivo experiments

A. Graphs show the number of spikes normalized to the control condition for monoaural auditory stimulation ("E0") on the first tick of the x-axis. Right tick ("E0+light") shows the number of spikes normalized to the control condition during the duration of the light pulse. Black circles indicate normalized spike counts for IC neurons and green circles indicate normalized spike counts for *DNLL* neurons. **B**. Graphs show the number of spikes normalized to the control condition for binaural auditory stimulation ("EE/EI") on the first tick of the x-axis. Right tick ("EE/EI+light") shows the number of spikes normalized to the control condition during the duration of the light pulse. Black circles indicate normalized spike counts for IC neurons and green circles indicate normalized spike counts for *DNLL* neurons. **C**. Shows the effect size for the whole duration (>200ms) of monoaural ("E0" and "0E/0I) and binaural evoked auditory responses. Black circles indicate effect sizes for IC neurons and green circles indicate effect sizes for *DNLL* neurons. Horizontal strokes indicate the mean value for each cell. **D.** Latencies for the first stimulus evoked spikes (1st spike) measured from the beginning of the recording. Left tick indicates first spike latencies of the control condition ("1st spike") and right tick indicate the first spike latencies of the light pulse condition ("1st spike+light"). Horizontal strokes indicate the mean value for each cell.

The y-axes in A. and B. are split into two regions for better visibility of the data points.

in the *DNLL* and *IC* and achieved neuron specific expression of the encoded transgene. The fluorescence of expressed *NpHR3.0-EYFP* was concentrated at the plasma membrane and could also be detected in axons and dendrites of transduced neurons (data not shown). After at least 1 month post injection, gerbils were anaesthetized and surgery and stereotactical alignment was performed. The sensory evoked spiking activity in transduced cells (n=6) in the

DNLL and *IC* could be suppressed with varying efficiency by *halorhodopsin*. In one case even the latencies of the first auditory evoked spikes were affected by the light pulse. Similar to the results from the *in vitro* patch-clamp experiments, the timing and duration of the light pulses also affected the efficiency of suppression. In one of the recorded *DNLL* cells (EI) near digital suppression could be achieved (Figure 36A). To measure the photosuppression level, the spike counts in the light condition were normalized to the condition without light. During the 150ms light pulse firing was reduced by 98% while auditory stimulation (mono- as well as binaural) was ongoing and even preceded the light pulse by 40ms. In another *DNLL* recording (EE) the light pulse preceded the auditory stimulation by 9ms and suppressed spiking activity by 63% (mono- as well as binaural) during the light pulse. After the light pulse, spiking activity increased to similar spike rates like recorded in the control condition without light (Figure 36B). Another effect of photosuppression with *halorhodopsin* was the increased latency for the first spikes compared to the control condition. An extracellular recording from an *IC* cell (EE) showed only a decrease in spiking of 4% in the monoaural stimulation (E0) and a decrease of 2% for the binaural stimulation (EE). But a postinhibitory rebound spike ~40ms after the light pulse led to spiking activity (Figure 36C). When neurons showed spontaneous activity (n=2), the spontaneous spiking could be suppressed stronger with light than stimulus evoked spiking.

The impact of *halorhodopsin* activation on spiking was quantified for six recorded cells by normalizing spike counts to the control condition without light presentation. Minor differences (<2%) were observed when comparing monoaural (E0) and binaural stimulation (EI/EE). The cell-to-cell variability of photosuppression on spiking was high and reached from 0.01 to 0.98 levels of control condition (Figure 37A&B). The two *DNLL* neurons were suppressed more effectively in comparison to the recorded *IC* neurons. The effect size was also calculated for the whole spiking activity in response to the 200ms auditory stimulation. Therefore effect sizes decreased for light pulses shorter than the auditory stimulation and the responses to it. Thereby, also the effect size for the only 150ms light pulse experiment was scaled down, since it only affected a 3/4 of the 200ms stimulus evoked responses. The effect size indicates the difference in spike number between control and light condition in relation to the spike number in the control condition (c.f. Methods section). The mean effect size was higher for monoaural (E0 and 0E) auditory stimulations: 0.42 (E0) and even 0.65 (0E/0I) respectively, whereas for binaural stimulation the mean effect size was 0.38 (EE/EI) (Figure 37C). As mentioned before the latencies of the first auditory evoked spike were affected in one of the *DNLL* recordings. Yet when comparing the latencies of the first spike in control and light pulse condition for all six recordings, none of the other five recorded cells showed a difference in spike latency (Figure 37D).

Summary

Photo suppression in the brain was successfully applied to *in vivo* experiments. Transduced cells were responsive to light and noise stimulus evoked firing could be successfully suppressed. As already indicate by the *in vitro* experiments, pulse duration and timing were most important factors for efficient stimulation. The cell-to-cell variability in expression levels of *halorhodopsin* and different distances to the light source most probably caused also differences in the amount of achievable suppression. An issue though, was the light transmission into the brain, which could only be achieved with high losses in light power.

5. Discussion

The discussion follows the order of the previous *Results* section. Firstly, the *rAAV* vector is discussed in regard to its suitability as a gene delivery vehicle in the *Mongolian Gerbil*. The measured specificity, efficiency, expression time and -levels of *rAAV* transduction are crucial issues. Secondly, the electrophysiological *in vitro* results are interpreted. The efficiency of the photostimulation, occurrence of the depolarization block, elicited AP timings, vector strength and jitter of evoked APs, as well as the design of the light stimulation are critical points for the use of the channelrhodopsin "*CatCH*". Important factors for the use of *NpHR3.0* are photocurrent amplitude, desensitization, timing and light stimulation regimes. Thirdly, the collected electrophysiological *in vivo* data is reviewed and combines crucial points from the first two points, efficiency in light stimulation, light regimes and delivery, and possible side effects from light stimulation and incomplete transduction of an entire auditory nucleus. At last, the conclusion sums up the data and observations.

5.1. A tool for neuronal specific transduction in the *Mongolian Gerbil*: *rAAV8YF*

As laid out from the five prerequisites formulated in the *Results* section (see chapter 4.2), *rAAV8YF* fulfills all five key issues. Neurons were successfully transduced (#1), expression of the transgenes was specific to neurons (#2), the transduction was efficient in affecting more than 50% of the neural population within the transduction area (#3), expression was detected as early as 7dpi and was persisting at all tested timepoints (#4) and last but not least the expression levels were sufficient to control the membrane potential with light (#5). From all performed virus injection experiments, it clearly follows that the constructed *rAAV8YF* vectors with *human synapsin I* promoter indeed drive neuron specific transgene expression in *MNTB*, *DNLL* and *IC*. No instance could be found where AAV mediated expression was not co-localized with neuronal markers, which indicates exclusive neuronal specificity. A bias towards increased or decreased transduction of certain neuronal subtypes was not apparent, but was also not studied in detail. In studies examining the tropism of *AAV8* serotype using ubiquitous promoters, a bias for the serotype 8 was found towards neurons (Broekman et al., 2006b; Masamizu et al., 2011a), but also a preference for certain neuronal subtypes can exist depending on the injected area (Cearley and Wolfe, 2006a), e.g. in the PNS: preference of large dorsal root ganglions over small dorsal root ganglions (Jacques et al., 2012).

In the CNS: only preference for neurons over glia (Aschauer et al., 2013; Broekman et al., 2006) and differences in neuronal transduction efficiency between brain areas were observed - no differentiation was made between neuronal subtypes though (Broekman et al., 2006a). An *AAV2/1* dilution series also revealed transduction bias towards inhibitory cortical neurons over excitatory ones for lower dilutions (Nathanson et al., 2009) but was not observed for *AAV2/8* (Aschauer et al., 2013). Since *AAV8YF* mediated expression emerges in about 50-60% of the neural population in the *IC* and has a similar efficiency for the *MNTB*, it can be assumed that there is probably no bias for a certain cell type. Furthermore, only by physiological (Aitkin et al., 1975; Sivaramakrishnan and Oliver, 2001) and morphological data (Oliver and Morest, 1984) functional distinct classes in the *IC* can be distinguished, but not on a molecular level. In order to drive cell type specific expression, the expression patterns which are exclusive to the cell type, have to be known. Therefore only a functional cell type discrimination could be conferred by immunostainings e.g. against potassium channels or with markers for GABAergic neurons (yet there are many populations of GABAergic neurons in the brain and the same holds true for neurons expressing potassium channels, hence exclusive cell type characterization is not possible). Co-localization of these markers with virally expressed fluorescent markers (e.g. *EYFP*) could reveal a possible bias towards a cell type in the *IC*. The measured transduction efficiency of 50-60% is also comparable to or above ratios found by other studies using *AAV2/8* for other brain areas, e.g. nigrostriatal system in the mouse: ~35% efficiency (McFarland et al., 2009), hippocampus in the mouse: ~30% efficiency (Cearley and Wolfe, 2006), or even close to 100% in the barrel cortex of a PV-Cre mouse (using transgenic cre-driver lines combined with "double-floxed" inverted open reading frame *rAAV*s) (Cardin et al., 2010). These studies use comparable virus titers but at least 4x larger injection volumes and the latter also a specific transgenic mouse driver line. Toxicity from overexpression of the transgene can affect cell health greatly (Klein et al., 2006). By altering the expressed transgene, the toxicity could not be abolished, and rather was correlated with AAV serotype (Howard et al., 2008). In studies with transgenic mouse lines and hence genomic expression of transgenes, toxic effects on cell health that render neurons fragile and nearly inaccessible for patch-clamp experiments were observed e.g. with neural expression of the monomeric *mcherry* (Asrican et al., 2013). In my experiments, transduced neurons show no apparent change in morphology or signs of apoptosis or necrosis. However, patch-clamp experiments turned out to be technically very demanding and inefficient due to high loss of transduced neurons right after slice preparation. Transduced neurons were very fragile upon formation of the giga seal with the patch pipette. In an *in vitro* study using r*AAV2/8* for expression of channelrhodopsins in the cerebellum and the hippocampus no technical difficulties were reported, but effects of the *AAV* serotype on synaptic transmission were observed that could be abolished when transgenes were

expressed genomically or diminished when expressed with *AAV2/9* (Jackman et al., 2014). Interestingly, all the *rAAV* vectors used in the study of Jackmann et al. are known to be axonally transported when injected into the hippocampus (Cearley and Wolfe, 2006; Cearley and Wolfe, 2007), which was neither reported nor discussed in the mentioned study (Jackman et al., 2014). However, all this evidence points towards unknown mechanisms due to *AAV* transduction slightly altering the transduced neuron. Maybe *AAV* transduction affects the level of the axonal transport and maybe also the overexpression of proteins like ChR2 that insert into the membrane could affect the viscosity of the plasma membrane. Nonetheless the side effects caused by *AAV* transduction are minor compared to *SLF* virus or *PRV* (Porres C., 2012).

Faulty trafficking of the channelrhodopsins can have cytotoxic effects and limit the magnitude of the photocurrent (Gradinaru et al., 2008; Gradinaru et al., 2010). In my experiments, the channelrhodopsin expression in transduced neurons seems to be exclusively localized to the membrane. Both *NpHR3.0* and *CatCH* show no clustering or aggregates in the cytoplasm. This is in contrast to the expressed soluble *EYFP*, where the fluorescence is apparently more homogenous spread throughout the soma. Although, to confirm correct membrane localization of channelrhodopsins, immunohistochemistry with membrane marker proteins and determining co-localization would be an additional proof. Yet, since light stimulation in electrophysiological experiments elicits photocurrents comparable to the according published data, it is safe to presume correct membrane trafficking. Also expression was only detected focally, and no anterograde or retrograde transport of the *rAAV*s could be observed in my injection experiments in *DNLL*, *IC* or *MNTB*. In studies using *rAAV*2/8, neuronal retrograde transport could be observed when injected into the *striatum* (Masamizu et al., 2011b; Taymans et al., 2007), muscles (Zheng et al., 2009), dentate gyrus and hippocampus (Castle et al., 2014). Anterograde transport was observed when injected into the entorhinal cortex (Castle et al., 2014). It can be considered an advantage, that *rAAV8YF* does not show axonal transport in my experiments, otherwise limiting the channelrhodopsin's effect to the target area would only be possible by spatially focusing the light. The diffusibility of *rAAV* due to its small particle size of only 20nm helps to transduce large areas with only small injection volumes and aids to cover the target area despite an imprecise injection. As a down side, the diffusibility causes areas adjacent to the injection site also to become partially transduced. This should be considered and when applied to *in vivo* experiments, the transduced areas should be analyzed post mortem. In the case of my *DNLL in vivo* experiments, the only auditory nucleus affected, would be the *IC* due to its vicinity 300-500µm dorsally. Nonetheless, the optical fibre focuses the light beam in ventral direction and therefore light transmission to the *IC* would be minimal. Hence, in the worst case responses to light in transduced *IC* neurons would be very weak and would fail to suppress action potential firing. Since the

IC is downstream in the signal path to the *DNLL*, responses recorded from the ipsilateral or contralateral *DNLL* should not be affected.

Expression times can be as low as 7 days for *in vitro* experiments, since transduced neurons with sufficient transgene expression can be visually identified by their fluorescence. Though, longer waiting times increase transgene expression levels and the number of cells having higher expression levels. Thereby the number of transduced cells that can be visually identified by their fluorescence is also increased. Thus application of channelrhodopsins in developmental studies would be also feasible, e.g. instead of irreversibly ablating the *cochlea* in a sensory deprivation paradigm, any station (*IHCs, OHCs, ANF, CN,...*) in the auditory signal path could be suppressed with *NpHR3.0.* In several *in vivo* studies, expression times > 3-4 weeks are employed (Adamantidis et al., 2011; Yizhar et al., 2011) but also waiting times of 7 days can be practiced (Cardin et al., 2010), depending on the purpose, necessary effect size and available light power. To maximize the number of transduced cells and for the sake of high expression levels given the limited available light power for my *in vivo* experiments, expression times of >4 weeks are reasonable. Expression levels are increasing with time, as can be inferred from the general higher SNR over time (see Results, chapter 4.4). Yet the dynamics of expression levels also increase, i.e. the differences between lowest detected and highest measured signal size are also increased. This means the individual differences in expression level are not compensated or equalized with expression time. This high variation in expression will hence also result in great variation of photo responses when *ChRs* or *NpHR3.0* are expressed.

5.2.1. *CatCH* enables optical control of the membrane potential in transduced *IC*, *MNTB* and *DNLL* neurons

In more than half of the *CatCH* expressing neurons, APs could be elicited with light pulses, whereas in the other neurons at least subthreshold depolarization was possible. For some of the transduced neurons even light pulses with decreasing pulse width (down to 40µs in one case) were sufficient for reliable spiking. Longer light pulses led to increased efficiency but beyond an individually determined pulse width, stimulation efficiency was not increasing anymore. When light pulses were too long, extra spikes or depolarization block occurred. The depolarization block could be seen by decreasing action potential amplitudes and incomplete repolarization. At higher stimulation frequencies though, also shorter light pulses were slightly more efficient in eliciting APs compared to lower stimulation frequencies. Especially light pulses following the first light pulse in a train had higher success in eliciting an AP.

This is probably due to the repeated depolarization of the membrane with each light pulse counteracting complete repolarization and moving the potential further towards AP threshold which facilitates subsequent firing. Albeit, according to the original study, photostimulation with *CatCH* should outperform other ChR2 variants in repolarisation of the plasma membrane due to enhanced activation of Ca^{2+} dependent BK channels (Kleinlogel et al., 2011). This means that there is a sweet spot in light pulse width for each cell individually. Usually though, pulse widths of 1- 5ms should result in reliable spiking. The light pulse widths also limit the achievable upper frequency of course. Although single cells could be efficiently driven with 100Hz optical stimulation without occurrence of extra spikes, in general most neurons were only able to follow a pulse train at 40-50Hz. This is due to the pulse width being the limiting factor at higher frequencies, because the periods are becoming shorter and therefore also the maximal possible duration of the pulse width. Shorter light pulses in turn also result in lower success at eliciting APs. Furthermore longer light pulses decreased the latencies of the elicited AP, making firing not only more efficient but also faster. The measured latencies in the course of my *in vitro* recordings are similar to published values (Kleinlogel et al., 2011). No difference in latencies between the first elicited AP and all subsequent APs could be determined. Even though previous firing and photocurrents might depolarize the membrane potential further, no speeding up occurred, which might be due to the depolarization block of the neuron and the desensitization of the channelrhodopsin at higher membrane potentials (Chater et al., 2010). No correlation between input resistance and latency was found. Jitter of light evoked APs also decreased with longer light pulse widths but again there was a sweet spot, beyond which jitter did not decrease anymore but increased. Increased phase locking to certain preferred stimulation frequencies was not encountered in *IC* neurons (Langner and Schreiner, 1988), rather pulse width was the determinant parameter for phase locking. The factor with the most impact on optical stimulation was the light pulse width. To some degree it might compensate the expression level of channelrhodopsin i.e. in neurons with lower levels of channelrhodopsin expression, longer light pulses should be as efficient as shorter light pulses in neurons with higher expression levels. Overall, it can be assumed that the expression levels and the available light seem to determine the efficiency of photostimulation and the latencies of elicited spikes.

On one hand, *CatCH* is functionally expressed in transduced neurons and optical stimulation of a transduced nucleus with *CatCH* would be possible on fast time scales (even allowing for slightly higher frequency stimulation than reported), with nearly instant reversibility exceeding activation kinetics by any drugs and with spatial precision exceeding activation by electrical stimulation.

On the other hand, since the individual illumination of each transduced neuron is not easily possible, the resulting response from the population of transduced neurons would include differences in efficiency of spiking and different spike latencies. Even stimulated with the most efficient light regime, latencies would vary too much per trial and thus jitter would be too high in transduced neurons to mimic auditory sensory input. Auditory neurons are precisely phase locking up to 600-800Hz, only then phase locking starts to decline (Grothe et al., 2010). Therefore the jitter from *CatCH* driven spikes even in the (sub)millisecond range is too high to simulate sensory input.

5.2.2. *NpHR3.0* suppresses spiking in transduced *IC*, *MNTB* and *DNLL* neurons

Utilization of *NpHR3.0* reliably conferred hyperpolarization upon optical stimulation in all transduced neurons in the *IC*, *MNTB* and *DNLL*. The measured photo currents were comparable to those published and also the kinetics match the published values (Gradinaru et al., 2010). An estimation of the light dependency is important for *halorhodopsin* because in contrast to ChRs, only one charge is transported across the membrane per absorbed photon, hence the available light determines the usefulness of *halorhodopsin* greatly. No dependency on light intensity was observed on the kinetics, but of course the photocurrent increased with higher light intensities. In all recorded neurons, photocurrents were already detected at the low light intensity ($0.7mW/mm^2$), which provided approximately ~25% of the maximal photocurrent (measured at $6.2mW/mm^2$). This lowest tested light intensity corresponds approximately the light intensity 250µm away from the optical fibre tip in my *in vivo* experiments. Under these light conditions the average photocurrent for all recorded neurons would approximate ~100pA. Steady state photocurrents were always lower than the peak photocurrent due to depletion of 11-cis-retinal by photoconversion, which could be observed in the decreasing photocurrents per each light pulse repetition as well. This photocurrent rundown could in principle be counteracted by flashes of blue light (Zhang et al., 2007) or longer dark periods (>45-90s), but was not tested though. In individual neurons even single APs in a spike train could be suppressed with light, yet these short light pulses did not always suffice to inhibit spiking. Suppression proved to be most efficient when the whole spike train was embedded within a light pulse of longer duration. Similar to *CatCH*, efficiency of *NpHR3.0* driven suppression is higher for longer light pulses. Long light pulses preceding and spanning the duration of the tested behavior or sensory stimulus are also used by other *in vivo* studies utilizing *halorhodopsin* (Felix-Ortiz et al., 2015). Effects that need to be carefully considered were the frequently observed postinhibitory rebound

spikes after cessation of the light pulse. Most likely I_h channels are activated during the hyperpolarization with *halorhodopsin* and those depolarize the neuron after the light. Postinhibitory rebound spikes following *halorhodopsin* activation always occurred in patch-clamp experiments when neurons (n=5) also displayed the typical I_h sag in the voltage response to hyperpolarizing currents (Halder et al., 2015). To test the causal relationship between the I_h currents and the postinhibitory rebound spikes, HCN channel blockers ZD7288 (Harris and Constanti, 1995) and DK–AH 269 (Raes et al., 1998) could be used in patch-clamp experiments. Consistently with the patch-clamp data, postinhibitory rebound spikes after *halorhodopsin* activation also occurred in *in vivo* experiments. Experimental conditions should account for these and limit the occurrence of these spikes to a time frame that lies beyond the actual tested paradigm. This is another reason to span the light pulse over the whole duration of the actual stimulation (e.g. electrical stimulation). Yet the interstimulus intervals should be long enough to counteract any changes in chloride reversal potentials, that occur when *NpHR* is continuously stimulated or activated at high repetition rates (Raimondo et al., 2012). The chloride reversal potential is maintained by the transporter *KCC2* which is widely expressed and shows high expression levels in the auditory brainstem (Friauf et al., 2011). Therefore equilibrium should probably be reached fast after *NpHR3.0* activation.

In sum, *NpHR3.0* is functionally expressed in transduced neurons. The suppression of a transduced nucleus would also be possible, with the same up- and downsides compared to *CatCH*: the activation and reversibility of the effect is nearly instantaneous and beats electrical stimulation in spatial precision and the ability to silence neurons.

5.3. Suppression of sensory evoked firing in the *DNLL* and *IC*

As a further proof of principle, *NpHR3.0* expressing *DNLL* and *IC* neurons could be suppressed and even completely silenced in vivo, as shown by extra cellular recordings. In the first trials a strong photoelectrochemical effect was observed causing voltage artifacts in response to light pulses. The artifact scaled with light intensity and light duration and could be traced to a phenomenon called *Becquerel effect.* In 1839, Becquerel observed that exposure to light induces small currents in metals when they are placed in an electrolyte (Becquerel, 1839). Especially strongly heterogeneous illumination and light with short wavelengths enhance the current's magnitude. The observed *in vivo* artifacts can easily be mistaken for smaller action potentials caused by light stimulation. The effect is most prominent when using metal electrodes and can only be avoided by using materials (e.g. indium tin oxide) that are resistant to this

phenomenon or by optically shielding the electrode and the light source from each other (Han, 2012). In my experiments, insertion of the fibre into a steel cannula completely eliminated the artifact.

The impact of photosuppression varied from cell to cell, since distances to the tip of the optical fibre and expression levels of *NpHR3.0* also varied. Two cells were strongly suppressed (98% and 65% reduction in spikes with light) and four cells were mildly suppressed (5-20% reduced number of spikes with light). Spontaneous acitivity (n=2) without auditory stimulation could be suppressed stronger than stimulus evoked activity. To enhance the level of suppression, it would be important to reach saturating light levels, since *halorhodopsin* is rate limited by only transporting one charge per photon. Saturating light power could be observed in my *in vitro* recordings at around 50% light intensity (=3-4mW/mm^2), which is a value that in my experiments could have only been reached within <100µm distance from the fibre. Usually the fibre was 250-600µm away from the recording electrode and the output of the fibre was usually only between 0.5-4.5mW/mm^2, resulting in much lower light levels at the recording site. As mentioned before, similar to the observations from *in vitro* patch-clamp recordings, postinhibitory rebound spiking (see results section, chapter 4.6.1) could be observed after cessation of the light pulse. These side effects cannot be avoided but influenced by the timing of the light pulse. Postinhibitory rebound spiking can be moved away from the actual tested firing behavior by setting the light pulse to a duration preceding and outlasting the actual tested paradigm. Hence, again light pulses including an earlier onset and later offset and spanning the whole duration of the sensory input, proved to be most efficient in suppressing activity. Despite the variation in the amount of suppression, the sum of global photo suppression nonetheless should impact on the duration of *GABAergic* PI to the contralateral *DNLL*. Since the activity of the *DNLL* neurons is the first stage for the translation into PI via subsequent synaptic and postsynaptic mechanisms (Ammer et al., 2015). Also hyperpolarization by *NpHR3.0* should aid to keep *NMDA* receptors in the transduced neurons blocked or to slow down activation and shorten activation times. This reduced activation of *NMDA* receptors would also result in a shortening of PI (Brungart and Rabinowitz, 1999; Porres et al., 2011). Probably the photosuppression would mimic a prepulse or sounds of lower amplitude from the contralateral ear at the stage of the *DNLL*, since a prepulse or sound amplitude determines the activity of the *DNLL* neurons and thereby the duration of the PI (Burger and Pollak, 2001; Pecka et al., 2007; Yang and Pollak, 1994). In turn, this gives rise to conflicts with other auditory areas, where the rate code is not manipulated - therefore any perceptional interpretation is very difficult. In an ideal setting, the complete inactivation of the contralateral *DNLL* would render the glycinergic input coming from the ipsilateral LSO the sole source of inhibition when stimulated at the ipsilateral ear. In an elaborate study, *DNLL* neurons in the bat were silenced by blocking excitation in and around the *DNLL*

with iontophoretic application of kynurenic acid (Burger and Pollak, 2001). This created a relief from inhibition in the contralateral *IC*, resulting in higher response rates for binaural stimulation since spatial selectivity in a portion of *IC* neurons was suspended. Suppression of the contralateral *DNLL* mimicked PI from the ipsilateral *DNLL* triggered by a prepulse. Therefore a similar experiment in the *Mongolian Gerbil* with the spatial and temporal precision conveyed by *NpHR3.0* would help to confirm the *DNLL's* impact on PI and would allow to the discriminate between the *DNLL's* and the *LSO's* contribution to PI in timing and duration. Issues arising from transduction of only a portion of the *DNLL* should not matter in recording the extracellular potentials from single transduced neurons in the ipsilateral *DNLL*. Since the transduced portion of neurons would show effects upon light stimulation, the only drawback from incomplete transduction would be the lower number of available neurons to record from. Unfortunately, there is no study quantifying the exact number of *DNLL* projections to their targets in the *DNLL* or *IC*. Therefore it remains speculative how many and how strongly transduced *DNLL* neurons have to be suppressed with light in order to see an effect in neurons of the contralateral *DNLL* or *IC*. Lesions (Kelly et al., 1996) and injections with kynurenic acid (Burger and Pollak, 2001) were successfully used by previous studies to inactivate the *DNLL*. The number of affected *DNLL* neurons in these approaches was probably higher than with *rAAV* transduction and light in my experiments because usually around 55-60% of the neurons could be transduced at the injection sites and these transduced neurons were not illuminated with saturating light levels. Maximizing transduction volume with injecting *rAAV* multiple times into different sites in the *DNLL* and reaching saturating light levels in the transduced *DNLL* should be very helpful to affect the firing pattern of contralateral *DNLL* and *IC*. Also when behavior should be affected, saturating light levels, high transduction efficiency and high expression levels are recommendable. By far the most of the optogenetic studies successfully manipulating the animal's behavior with light rely largely on transgenic model organisms (Grosenick et al., 2015; Gunaydin et al., 2014; Hernandez-Nunez et al., 2015; Husson et al., 2013). In transgenic animals expression of *channelrhodopsins* can be precisely directed to a defined population of neurons. Light manipulation therefore affects a complete and defined population of neurons. In the case of our model system, the *Mongolian Gerbil* incomplete transduction of a nucleus comes from either imprecise stereotactical vector injection or failure of vector docking and subsequent DNA uptake/release into the host cell. A study in *macaque* monkeys successfully used *AAV* vectors expressing *channelrhodospin* widely and unspecifically (under *CMV* promoter control) in the frontal eye field. Stimulation with very high laser power (up to 1100mW/mm^2) of the axons and terminals of transduced neurons influenced the behavior measurably (Inoue et al., 2015). Accordingly, future optogenetic experiments aiming to affect the *Mongolian Gerbil's* behavior in listening tasks while manipulating the *DNLL* should apply a similar strategy.

As mentioned before, high light power and high transduction efficiency are key elements for successful experiments. To establish a causal link between the precedence effect and the *DNLL-IC* circuit it is clear that the circuit has to be optogenetically manipulated. It is also clear that a relevant listening behavior has to be measured (e.g. amount of fusion, amount of lateralization or discrimination suppression) before, during and after the acute manipulation. Though the interpretation of the data from such acute manipulation experiments is still difficult as downstream circuits might cloud or influence the behavior (Otchy et al., 2015). Only if results from chronic manipulation experiments (lesions, ablations…) are similar to the results from acute manipulation studies, a possible causal link can be drawn.

5.4. Conclusion

In the course of my PhD study, I could successfully establish reliable gene delivery with neuronal specificity in the brainstem (*MNTB* and *DNLL*) and midbrain (*IC*) of the *Mongolian Gerbil* by utilizing the viral vector *rAAV8YF*. A versatile tool that can extend its usefulness far beyond optogenetics e.g. permitting expression of nearly any transgene (<4.7kb), knockdown of target genes or even specific knock-out of genes, knock-in and genome editing with the help of the CRISPR/Cas9 system. Genome editing of neurons in the *Mongolian Gerbil* would thereby be feasible. Furthermore, I also successfully established optogenetics in the *Mongolian Gerbil* and confirmed the functionality and usefulness of the channelrhodopsin *CatCH* and *halorhodopsin NpHR3.0* in *in vitro* and *in vivo* applications. Sensory evoked spiking activity could be strongly suppressed *in vivo* in *IC* and *DNLL* neurons by light activation of *halorhodopsin*. The parameterization of *NpHR3.0* and *CatCH* molecules in optical stimulation experiments allows for more efficient use and paves the way for further and improved *in vivo* experiments; even experiments with freely behaving animals would now be feasible with the *Mongolian Gerbil*.

6. Glossary

°C	degree Celsius
µA	micro Ampere
µg	micro gram
µl	micro liter
µm	micro meter
µs	micro second
0E	monoaural excitatory stimulation at the right ear
0I	monoaural inhibitory stimulation at the right ear
AAV	Adeno Associated Virus
AFN	Atipamezole, Flumazenile, Naloxon
Amp	Ampicilin
ANF	Auditory Nerve Fibre
AP	Action Potential
AP-5	amino-5-phosphonovaleric acid
ArchT	archaerhodopsin Halorubrum strain TP009
AU	Arbitrary Units
AVCN	Anteroventral Cochlear Nucleus
bp	base pairs
CAP	Capsid
CatCH	Calcium translocating Channelrhodopsin
CCP	Clathrin Coated Pits
CF	Characteristic Frequency
ChEF	ChR2/ChR2 chimera with crossover site at loop E-F
ChETA	Channelrhodopsin 2 mutants :E123T/A
ChIEF	ChEF mutant I170V

ChloC	Chloride-conducting Channelrhodopsin
ChR	Channelrhodopsin
cm	centi meters
CN	Cochlear Nucleus
DAPI	4',6-diamidino-2-phenylindole
dB	dezibel
ddH$_2$O	double distilled water
DNA	deoxy-ribonucleic acid
DNLL	Dorsal Nucleus of the Lateral Lemniskus
DNQX	6,7-dinitroquinoxaline-2,3-dione
dNTP	deoxy Nucleotide Triphosphate
dpi	days post injection
DSMO	Dimethylsulfoxide
E0	monoaural excitatory stimulation at the left ear
ECL	Extacellular Loop
EDTA	ethylenediaminetetraacetic acid
EE	binaural excitatory stimulation
EI	binaural excitatory(left ear) and inhibitory (right ear) stimulation
EYFP	Enhanced Yellow Fluorescent Protein
FIR	Finite Impulse Response
g	local gravitational constant
GABA	γ-Aminobutyric acid
GBC	Globular Bushy cells
GC	Guanine-Cytosine
GFP	Green Fluorescent Protein
GPCR	G-Protein Coupled Receptor

GPI	Glycosylphosphatidylinositol
HEK cells	Human Embryonic Kidney cells
HEPES	Hydroxyethyl-1-Piperazineethanesulfonic acid
hGh	human Growthhormone
HRTF	Head Related Transferfunction
hSyn	human Synapsin
Hz	Hertz
i.p.	intraperitoneal
IC	Inferior Colliculus
ICL	Intracellular Loop
IE	binaural inhibitory (left ear) and excitatory (right ear) stimulation
I_h	hyperpolarization-activated current
IHC	Inner Haircell
ILD	Interaural Level Difference
IPD	Interaural Phase Disparity
ITD	Interaural Time Difference
ITR	Inverted Terminal Repeats
JND	Just-Noticable Difference
kB	kilo Bases
kHz	kilo Hertz
K_{LVA}	low voltage-activated K channel
kPa	kilo Pascal
LASER	Light Amplification by Stimulated Emission of Radiation
LE	Late Endosome
LED	Light Emitting Diode
LNTB	Lateral Nucleus of the Trapezoid Body

LSO	Lateral Superior Olive
LY	Lysing Endosome
m	meter
M	Molar
MAA	Minimal Audible Angle
Map2	Microtubule-Associated Protein 2
mcherry	monomeric cherry flourescent protein
mg	milli gram
min	minutes
ml	milli liter
mm	milli meter
mM	milli Molar
MMF	Medetomidin, Midazolam, Fentanyl
MNTB	Medial Nucleus of the Trapezoid Body
ms	milli seconds
mS	milli Siemens
MSO	Medial Superior Olive
mW	milli Watt
MΩ	Mega Ohm
N	Newton
nA	nano Ampere
NeuN	Neuronal Nuclei antigen
nl	nano liter
nm	nano meter
NPC	Nuclear Pore Complex
NpHR	Natronomonas pharaonis Halorhodopsin

nt	nucleotides
OHC	Outer Haircell
P	Postnatal
pA	pico Ampere
Pa	Pascal
pAAV	plasmid based AAV
PBS	Phosphate Buffered Saline
PCR	Polymerase Chain Reaction
PFA	Paraformaldehyde
PI	Persistent Inhibition
poly A	Polyadenylation tail
pS	pico Siemens
PSTH	Peristimulus Time Histogram
qPCR	quantitative Polymerase Chain Reaction
rAAV	recombinant AAV
REP	Replication
RNA	Ribonucleic acid
rpm	rounds per minute
s	seconds
s.c.	subcutaneous
S100ß	S100 calcium-binding protein beta
SBC	Sperical Bushy Cell
scAAV	selfcomplementary AAV
SOC	Superior Olivary Complex
SPL	Sound Pressure Level
SPN	Superior Paraolivary Nucleus

ss	single straded
T2A	Thoseaasigna virus 2A peptide
TBE	Tris/Borate/EDTA buffer
TGN	Trans Golgi Network
TM	Transmembrane
U	Unit
UV	Ultra-violet
v/v	volume/volume
VCN	Ventral Cochlear Nucleus
W	Watt
wpi	weeks post injection
WPRE	Woodchuck Hepatitis Virus Posttranscriptional Regulatory Element

7. Bibliography

Adamantidis, A.R., Tsai, H.-C., Boutrel, B., Zhang, F., Stuber, G.D., Budygin, E.A., Touriño, C., Bonci, A., Deisseroth, K., and de Lecea, L. (2011). Optogenetic interrogation of dopaminergic modulation of the multiple phases of reward-seeking behavior. The Journal of Neuroscience 31, 10829-10835.

Ågren, G. (1984). Pair formation in the Mongolian gerbil. Animal behaviour 32, 528-535.

Aibara, R., Welsh, J.T., Puria, S., and Goode, R.L. (2001). Human middle-ear sound transfer function and cochlear input impedance. Hearing research 152, 100-109.

Aitkin, L., Webster, W., Veale, J., and Crosby, D. (1975). Inferior colliculus. I. Comparison of response properties of neurons in central, pericentral, and external nuclei of adult cat. Journal of Neurophysiology 38, 1196-1207.

Akache, B., Grimm, D., Pandey, K., Yant, S.R., Xu, H., and Kay, M.A. (2006). The 37/67-kilodalton laminin receptor is a receptor for adeno-associated virus serotypes 8, 2, 3, and 9. Journal of virology 80, 9831-9836.

Algazi, V.R., Duda, R.O., Thompson, D.M., and Avendano, C. (2001). The cipic hrtf database. In Applications of Signal Processing to Audio and Acoustics, 2001 IEEE Workshop on the (IEEE), pp. 99-102.

Ammer, J.J., Siveke, I., and Felmy, F. (2015). Activity-Dependent Transmission and Integration Control the Timescales of Auditory Processing at an Inhibitory Synapse. Current Biology 25, 1562-1572.

Aschauer, D.F., Kreuz, S., and Rumpel, S. (2013b). Analysis of transduction efficiency, tropism and axonal transport of AAV serotypes 1, 2, 5, 6, 8 and 9 in the mouse brain. PloS one 8, e76310.

Asrican, B., Augustine, G.J., Berglund, K., Chen, S., Chow, N., Deisseroth, K., Feng, G., Gloss, B., Hira, R., Hoffmann, C., et al. (2013). Next-generation transgenic mice for optogenetic analysis of neural circuits. Frontiers in neural circuits 7, 160.

Atchison, R.W., Casto, B.C., and Hammon, W.M. (1965). Adenovirus-associated defective virus particles. Science 149, 754-755.

Bamann, C., Kirsch, T., Nagel, G., and Bamberg, E. (2008). Spectral characteristics of the photocycle of channelrhodopsin-2 and its implication for channel function. Journal of molecular biology 375, 686-694.

Baumann, V.J., Lehnert, S., Leibold, C., and Koch, U. (2013). Tonotopic organization of the hyperpolarization-activated current (I(h)) in the mammalian medial superior olive. Frontiers in neural circuits 7, 117.

Becquerel, A.E. (1839). Recherches sur les effets de la radiation chimique de la lumiere solaire au moyen des courants electriques. Comptes Rendus de L´Academie des Sciences 9.

Berndt, A., Schoenenberger, P., Mattis, J., Tye, K.M., Deisseroth, K., Hegemann, P., and Oertner, T.G. (2011). High-efficiency channelrhodopsins for fast neuronal stimulation at low light levels. Proceedings of the National Academy of Sciences of the United States of America 108, 7595-7600.

Berns, K., and Giraud, C. (1996). Biology of adeno-associated virus. In Adeno-Associated Virus (AAV) Vectors in Gene Therapy (Springer), pp. 1-23.

Bianchi, D., Marasco, A., Limongiello, A., Marchetti, C., Marie, H., Tirozzi, B., and Migliore, M. (2012). On the mechanisms underlying the depolarization block in the spiking dynamics of CA1 pyramidal neurons. Journal of computational neuroscience 33, 207-225.

Bianchi, F., Verhulst, S., and Dau, T. (2013). Experimental evidence for a cochlear source of the precedence effect. Journal of the Association for Research in Otolaryngology : JARO 14, 767-779.

Blackstock, D.T. (2000). Fundamentals of Physical Acoustics (Wiley).

Blauert, J. (1997a). Spatial hearing. (Cambridge, MA: MIT Press).

Blauert, J. (1997b). Spatial hearing: the psychophysics of human sound localization (MIT press).

Boyden, E.S., Zhang, F., Bamberg, E., Nagel, G., and Deisseroth, K. (2005). Millisecond-timescale, genetically targeted optical control of neural activity. Nat Neurosci 8, 1263-1268.

Bradley, J.S., Sato, H., and Picard, M. (2003). On the importance of early reflections for speech in rooms. The Journal of the Acoustical Society of America 113, 3233-3244.

Broekman, M.L., Comer, L.A., Hyman, B.T., and Sena-Esteves, M. (2006). Adeno-associated virus vectors serotyped with AAV8 capsid are more efficient than AAV-1 or -2 serotypes for widespread gene delivery to the neonatal mouse brain. Neuroscience 138, 501-510.

Brown, A.D., Jones, H.G., Kan, A., Thakkar, T., Stecker, G.C., Goupell, M.J., and Litovsky, R.Y. (2015a). Evidence for a neural source of the precedence effect in sound localization. Journal of neurophysiology 114, 2991-3001.

Brown, A.D., Stecker, G.C., and Tollin, D.J. (2015b). The precedence effect in sound localization. Journal of the Association for Research in Otolaryngology : JARO 16, 1-28.

Brughera, A., Dunai, L., and Hartmann, W.M. (2013). Human interaural time difference thresholds for sine tones: the high-frequency limit. The Journal of the Acoustical Society of America 133, 2839-2855.

Brungart, D.S., and Rabinowitz, W.M. (1999). Auditory localization of nearby sources. Head-related transfer functions. The Journal of the Acoustical Society of America 106, 1465-1479.

Burger, C., Gorbatyuk, O.S., Velardo, M.J., Peden, C.S., Williams, P., Zolotukhin, S., Reier, P.J., Mandel, R.J., and Muzyczka, N. (2004). Recombinant AAV viral vectors pseudotyped with viral capsids from serotypes 1, 2, and 5 display differential efficiency and cell tropism after delivery to different regions of the central nervous system. Molecular Therapy 10, 302-317.

Burger, R.M., and Pollak, G.D. (2001). Reversible inactivation of the dorsal nucleus of the lateral lemniscus reveals its role in the processing of multiple sound sources in the inferior colliculus of bats. The Journal of neuroscience : the official journal of the Society for Neuroscience 21, 4830-4843.

Calcedo, R., Vandenberghe, L.H., Gao, G., Lin, J., and Wilson, J.M. (2009). Worldwide Epidemiology of Neutralizing Antibodies to Adeno-Associated Viruses. Journal of Infectious Diseases 199, 381-390.

Cardin, J.A., Carlen, M., Meletis, K., Knoblich, U., Zhang, F., Deisseroth, K., Tsai, L.-H., and Moore, C.I. (2010). Targeted optogenetic stimulation and recording of neurons *in vivo* using cell-type-specific expression of Channelrhodopsin-2. Nat Protocols 5, 247-254.

Carlile, S., Delaney, S., and Corderoy, A. (1999). The localisation of spectrally restricted sounds by human listeners. Hearing research 128, 175-189.

Carlile, S., Leong, P., and Hyams, S. (1997). The nature and distribution of errors in sound localization by human listeners. Hearing research 114, 179-196.

Carr, C.E., and Konishi, M. (1990). A circuit for detection of interaural time differences in the brain stem of the barn owl. The Journal of neuroscience : the official journal of the Society for Neuroscience 10, 3227-3246.

Castle, M.J., Gershenson, Z.T., Giles, A.R., Holzbaur, E.L.F., and Wolfe, J.H. (2014). Adeno-Associated Virus Serotypes 1, 8, and 9 Share Conserved Mechanisms for Anterograde and Retrograde Axonal Transport. Human gene therapy 25, 705-720.

Cearley, C.N., and Wolfe, J.H. (2006). Transduction characteristics of adeno-associated virus vectors expressing cap serotypes 7, 8, 9, and Rh10 in the mouse brain. Molecular therapy : the journal of the American Society of Gene Therapy 13, 528-537.

Cearley, C.N., and Wolfe, J.H. (2007). A Single Injection of an Adeno-Associated Virus Vector into Nuclei with Divergent Connections Results in Widespread Vector Distribution in the Brain and Global Correction of a Neurogenetic Disease. The Journal of Neuroscience 27, 9928-9940.

Chater, T.E., Henley, J.M., Brown, J.T., and Randall, A.D. (2010). Voltage- and temperature-dependent gating of heterologously expressed channelrhodopsin-2. Journal of Neuroscience Methods 193, 7-13.

Clifton, R.K. (1987). Breakdown of echo suppression in the precedence effect. The Journal of the Acoustical Society of America 82, 1834-1835.

Clifton, R.K., Freyman, R.L., Litovsky, R.Y., and McCall, D. (1994). Listeners' expectations about echoes can raise or lower echo threshold. The Journal of the Acoustical Society of America 95, 1525-1533.

Cremer, L. (1948). Geometrische raumakustik (Hirzel).

Crick, F.H. (1979). Thinking about the brain. Scientific American.

Dahmen, J.C., Keating, P., Nodal, F.R., Schulz, A.L., and King, A.J. (2010). Adaptation to Stimulus Statistics in the Perception and Neural Representation of Auditory Space. Neuron 66, 937-948.

Dean, I., Harper, N.S., and McAlpine, D. (2005). Neural population coding of sound level adapts to stimulus statistics. Nat Neurosci 8, 1684-1689.

Deisseroth, K., Feng, G., Majewska, A.K., Miesenbock, G., Ting, A., and Schnitzer, M.J. (2006). Next-generation optical technologies for illuminating genetically targeted brain circuits. The Journal of neuroscience : the official journal of the Society for Neuroscience 26, 10380-10386.

Dent, M.L., Tollin, D.J., and Yin, T.C.T. (2009). Influence of Sound Source Location on the Behavior and Physiology of the Precedence Effect in Cats. Journal of Neurophysiology 102, 724-734.

Dolan, T.R., Hirsh, I.R., and Yost, W.A. (1981). Detection of binaural signals partially masked by a reproducible noise maker: the influence of the phase angle alpha. The Journal of the Acoustical Society of America 70, 886-888.

Domnitz, R.H., and Colburn, H.S. (1977). Lateral position and interaural discrimination. The Journal of the Acoustical Society of America 61, 1586-1598.

Duan, D., Sharma, P., Yang, J., Yue, Y., Dudus, L., Zhang, Y., Fisher, K.J., and Engelhardt, J.F. (1998). Circular intermediates of recombinant adeno-associated virus have defined structural characteristics responsible for long-term episomal persistence in muscle tissue. Journal of virology 72, 8568-8577.

Dufour, S., and De Koninck, Y. (2015). Optrodes for combined optogenetics and electrophysiology in live animals. Neurophotonics 2, 031205.

Dutheil, N., Shi, F., Dupressoir, T., and Linden, R.M. (2000). Adeno-associated virus site-specifically integrates into a muscle-specific DNA region. Proceedings of the National Academy of Sciences 97, 4862-4866.

Englitz, B., Tolnai, S., Typlt, M., Jost, J., and Rübsamen, R. (2009). Reliability of Synaptic Transmission at the Synapses of Held *In Vivo* under Acoustic Stimulation. PloS one 4, e7014.

Faingold, C.L., Anderson, C.A., and Randall, M.E. (1993). Stimulation or blockade of the dorsal nucleus of the lateral lemniscus alters binaural and tonic inhibition in contralateral inferior colliculus neurons. Hearing research 69, 98-106.

Faingold, C.L., Boersma Anderson, C.A., and Caspary, D.M. (1991). Involvement of GABA in acoustically-evoked inhibition in inferior colliculus neurons. Hearing research 52, 201-216.

Feddersen, W., Sandel, T., Teas, D., and Jeffress, L. (1957). Localization of high-frequency tones. The Journal of the Acoustical Society of America 29, 988-991.

Felix-Ortiz, A.C., Burgos-Robles, A., Bhagat, N.D., Leppla, C.A., and Tye, K.M. (2015). Bidirectional modulation of anxiety-related and social behaviors by amygdala projections to the medial prefrontal cortex. Neuroscience.

Fenno, L., Yizhar, O., and Deisseroth, K. (2011). The development and application of optogenetics. Annual review of neuroscience 34, 389-412.

Fettiplace, R., and Kim, K.X. (2014). The physiology of mechanoelectrical transduction channels in hearing. Physiological reviews 94, 951-986.

Ford, M.C., Alexandrova, O., Cossell, L., Stange-Marten, A., Sinclair, J., Kopp-Scheinpflug, C., Pecka, M., Attwell, D., and Grothe, B. (2015). Tuning of Ranvier node and internode properties in myelinated axons to adjust action potential timing. Nature communications 6.

Freyman, R.L., Clifton, R.K., and Litovsky, R.Y. (1991). Dynamic processes in the precedence effect. The Journal of the Acoustical Society of America 90, 874-884.

Friauf, E., Rust, M.B., Schulenborg, T., and Hirtz, J.J. (2011). Chloride cotransporters, chloride homeostasis, and synaptic inhibition in the developing auditory system. Hearing research 279, 96-110.

Gaiko, O., and Dempski, R.E. (2013). Transmembrane domain three contributes to the ion conductance pathway of channelrhodopsin-2. Biophysical journal 104, 1230-1237.

Glendenning, K.K., Brusno-Bechtold, J.K., Thompson, G.C., and Masterton, R.B. (1981). Ascending auditory afferents to the nuclei of the lateral leminscus. The Journal of Comparative Neurology 197, 673-703.

Glowatzki, E., Grant, L., and Fuchs, P. (2008). Hair cell afferent synapses. Current Opinion in Neurobiology 18, 389-395.

Goldberg, J.M., and Brown, P.B. (1969). Response of binaural neurons of dog superior olivary complex to dichotic tonal stimuli: some physiological mechanisms of sound localization. Journal of neurophysiology 32, 613-636.

Goodman, D.F., Benichoux, V., and Brette, R. (2013). Decoding neural responses to temporal cues for sound localization. eLife 2, e01312.

Gradinaru, V., Thompson, K.R., and Deisseroth, K. (2008). eNpHR: a Natronomonas halorhodopsin enhanced for optogenetic applications. Brain cell biology 36, 129-139.

Gradinaru, V., Zhang, F., Ramakrishnan, C., Mattis, J., Prakash, R., Diester, I., Goshen, I., Thompson, K.R., and Deisseroth, K. (2010). Molecular and cellular approaches for diversifying and extending optogenetics. Cell 141, 154-165.

Grantham, D.W. (1995). Spatial Hearing and. Hearing, 297.

Griffin, S.J., Bernstein, L.R., Ingham, N.J., and McAlpine, D. (2005). Neural sensitivity to interaural envelope delays in the inferior colliculus of the guinea pig. Journal of neurophysiology 93, 3463-3478.

Grosenick, L., Marshel, J.H., and Deisseroth, K. (2015). Closed-loop and activity-guided optogenetic control. Neuron 86, 106-139.

Grothe, B., and Pecka, M. (2014). The natural history of sound localization in mammals – a story of neuronal inhibition. Frontiers in neural circuits 8, 116.

Grothe, B., Pecka, M., and McAlpine, D. (2010). Mechanisms of sound localization in mammals. Physiological reviews 90, 983-1012.

Grothe, B., and Sanes, D.H. (1994). Synaptic inhibition influences the temporal coding properties of medial superior olivary neurons: an *in vitro* study. The Journal of neuroscience 14, 1701-1709.

Gunaydin, Lisa A., Grosenick, L., Finkelstein, Joel C., Kauvar, Isaac V., Fenno, Lief E., Adhikari, A., Lammel, S., Mirzabekov, Julie J., Airan, Raag D., Zalocusky, Kelly A.*, et al.* (2014). Natural Neural Projection Dynamics Underlying Social Behavior. Cell 157, 1535-1551.

Gunaydin, L.A., Yizhar, O., Berndt, A., Sohal, V.S., Deisseroth, K., and Hegemann, P. (2010). Ultrafast optogenetic control. Nat Neurosci 13, 387-392.

Haas, H. (1951). Über den Einfluβ eines Einfachechos auf die Hörsamkeit von Sprache. Acta Acustica united with Acustica 1, 49-58.

Hafter, E.R., and Buell, T.N. (1990). Restarting the adapted binaural system. The Journal of the Acoustical Society of America 88, 806-812.

Halder, S., Van Vliet, K., Smith, J.K., Duong, T.T.P., McKenna, R., Wilson, J.M., and Agbandje-McKenna, M. (2015). Structure of neurotropic adeno-associated virus AAVrh.8. Journal of Structural Biology 192, 21-36.

Han, X. (2012). *In vivo* Application of Optogenetics for Neural Circuit Analysis. ACS Chemical Neuroscience 3, 577-584.

Han, X., and Boyden, E.S. (2007). Multiple-color optical activation, silencing, and desynchronization of neural activity, with single-spike temporal resolution. PloS one 2, e299.

Han, X., Chow, B.Y., Zhou, H., Klapoetke, N.C., Chuong, A., Rajimehr, R., Yang, A., Baratta, M.V., Winkle, J., Desimone, R., and Boyden, E.S. (2011). A high-light sensitivity optical neural silencer: development and application to optogenetic control of non-human primate cortex. Frontiers in systems neuroscience 5, 18.

Harper, N.S., Scott, B.H., Semple, M.N., and McAlpine, D. (2014). The neural code for auditory space depends on sound frequency and head size in an optimal manner. PloS one 9, e108154.

Harris, N.C., and Constanti, A. (1995). Mechanism of block by ZD 7288 of the hyperpolarization-activated inward rectifying current in guinea pig substantia nigra neurons in vitro. Journal of neurophysiology 74, 2366-2378.

Hartmann, W.M., and Rakerd, B. (1989). Localization of sound in rooms IV: The Franssen effect. The Journal of the Acoustical Society of America 86, 1366-1373.

Hawley, M.L., Litovsky, R.Y., and Culling, J.F. (2004). The benefit of binaural hearing in a cocktail party: Effect of location and type of interferer. The Journal of the Acoustical Society of America 115, 833-843.

Herman, A.M., Huang, L., Murphey, D.K., Garcia, I., and Arenkiel, B.R. (2014). Cell type-specific and time-dependent light exposure contribute to silencing in neurons expressing Channelrhodopsin-2. eLife 3, e01481.

Hermonat, P.L., and Muzyczka, N. (1984). Use of adeno-associated virus as a mammalian DNA cloning vector: transduction of neomycin resistance into mammalian tissue culture cells. Proceedings of the National Academy of Sciences 81, 6466-6470.

Hernandez-Nunez, L., Belina, J., Klein, M., Si, G., Claus, L., Carlson, J.R., and Samuel, A.D. (2015). Reverse-correlation analysis of navigation dynamics in Drosophila larva using optogenetics. eLife 4.

Howard, D.B., Powers, K., Wang, Y., and Harvey, B.K. (2008). Tropism and toxicity of adeno-associated viral vector serotypes 1, 2, 5, 6, 7, 8, and 9 in rat neurons and glia in vitro. Virology 372, 24-34.

Hudspeth, A.J. (1989). How the ear's works work. Nature 341, 397-404.

Husson, S.J., Gottschalk, A., and Leifer, A.M. (2013). Optogenetic manipulation of neural activity in C. elegans: from synapse to circuits and behaviour. Biology of the cell / under the auspices of the European Cell Biology Organization 105, 235-250.

Inoue, K., Takada, M., and Matsumoto, M. (2015). Neuronal and behavioural modulations by pathway-selective optogenetic stimulation of the primate oculomotor system. Nature communications 6, 8378.

Ito, M., van Adel, B., and Kelly, J.B. (1996). Sound localization after transection of the commissure of Probst in the albino rat. Journal of Neurophysiology 76, 3493-3502.

Jackman, S.L., Beneduce, B.M., Drew, I.R., and Regehr, W.G. (2014). Achieving high-frequency optical control of synaptic transmission. The Journal of Neuroscience 34, 7704-7714.

Jacques, S.J., Ahmed, Z., Forbes, A., Douglas, M.R., Vigenswara, V., Berry, M., and Logan, A. (2012). AAV8(gfp) preferentially targets large diameter dorsal root ganglion neurones after both intra-dorsal root ganglion and intrathecal injection. Molecular and cellular neurosciences 49, 464-474.

Jeffress, L.A. (1948). A place theory of sound localization. Journal of comparative and physiological psychology 41, 35.

Johnson, D.H. (1980). The relationship between spike rate and synchrony in responses of auditory-nerve fibres to single tones. The Journal of the Acoustical Society of America 68, 1115-1122.

Joris, P.X, Carney, L.H., Smith, P.H., and Yin, T.C. (1994). Enhancement of neural synchronization in the anteroventral cochlear nucleus. I. Responses to tones at the characteristic frequency. Journal of neurophysiology 71, 1022-1036.

Joris, P.X, Schreiner, C.E., and Rees, A. (2004). Neural Processing of Amplitude-Modulated Sounds. Physiological reviews 84, 541-577.

Joseph, A.W., and Hyson, R.L. (1993). Coincidence detection by binaural neurons in the chick brain stem. Journal of Neurophysiology 69, 1197-1211.

Kashiwakura, Y., Tamayose, K., Iwabuchi, K., Hirai, Y., Shimada, T., Matsumoto, K., Nakamura, T., Watanabe, M., Oshimi, K., and Daida, H. (2005). Hepatocyte growth factor receptor is a coreceptor for adeno-associated virus type 2 infection. Journal of virology 79, 609-614.

Kato, H.E., Zhang, F., Yizhar, O., Ramakrishnan, C., Nishizawa, T., Hirata, K., Ito, J., Aita, Y., Tsukazaki, T., Hayashi, S., *et al.* (2012). Crystal structure of the channelrhodopsin light-gated cation channel. Nature 482, 369-374.

Kelly, J.B., Buckthought, A.D., and Kidd, S.A. (1998). Monaural and binaural response properties of single neurons in the rat's dorsal nucleus of the lateral lemniscus. Hearing research 122, 25-40.

Kelly, J.B., Li, L., and van Adel, B. (1996). Sound localization after kainic acid lesions of the dorsal nucleus of the lateral lemniscus in the albino rat. Behav Neurosci 110, 1445-1455.

Khurana, S., Remme, M.W., Rinzel, J., and Golding, N.L. (2011). Dynamic interaction of Ih and IK-LVA during trains of synaptic potentials in principal neurons of the medial superior olive. The Journal of neuroscience : the official journal of the Society for Neuroscience 31, 8936-8947.

Kimberley, B.P., Brown, D.K., and Eggermont, J.J. (1993). Measuring human cochlear traveling wave delay using distortion product emission phase responses. The Journal of the Acoustical Society of America 94, 1343-1350.

Klapoetke, N.C., Murata, Y., Kim, S.S., Pulver, S.R., Birdsey-Benson, A., Cho, Y.K., Morimoto, T.K., Chuong, A.S., Carpenter, E.J., Tian, Z., et al. (2014). Independent optical excitation of distinct neural populations. Nat Meth 11, 338-346.

Klein, R.L., Dayton, R.D., Leidenheimer, N.J., Jansen, K., Golde, T.E., and Zweig, R.M. (2006). Efficient Neuronal Gene Transfer with AAV8 Leads to Neurotoxic Levels of Tau or Green Fluorescent Proteins. Molecular therapy : the journal of the American Society of Gene Therapy 13, 517-527.

Kleinlogel, S., Feldbauer, K., Dempski, R.E., Fotis, H., Wood, P.G., Bamann, C., and Bamberg, E. (2011). Ultra light-sensitive and fast neuronal activation with the Ca(2)+-permeable channelrhodopsin CatCh. Nat Neurosci 14, 513-518.

Klumpp, R.G., and Eady, H.R. (1956). Some Measurements of Interaural Time Difference Thresholds. The Journal of the Acoustical Society of America 28, 859-860.

Koch, S., Sothilingam, V., Garcia Garrido, M., Tanimoto, N., Becirovic, E., Koch, F., Seide, C., Beck, S.C., Seeliger, M.W., Biel, M., et al. (2012). Gene therapy restores vision and delays degeneration in the CNGB1(-/-) mouse model of retinitis pigmentosa. Human molecular genetics 21, 4486-4496.

Kopp-Scheinpflug, C., Dehmel, S., Dörrscheidt, G.J., and Rübsamen, R. (2002). Interaction of excitation and inhibition in anteroventral cochlear nucleus neurons that receive large endbulb synaptic endings. The Journal of neuroscience 22, 11004-11018.

Kuttruff, H. (2009). Room acoustics (CRC Press).

Kuwabara, N., and Zook, J.M. (1992). Projections to the medial superior olive from the medial and lateral nuclei of the trapezoid body in rodents and bats. The Journal of Comparative Neurology 324, 522-538.

Kwan, K.Y., Allchorne, A.J., Vollrath, M.A., Christensen, A.P., Zhang, D.-S., Woolf, C.J., and Corey, D.P. (2006). TRPA1 contributes to cold, mechanical, and chemical nociception but is not essential for hair-cell transduction. Neuron 50, 277-289.

Langner, G., and Schreiner, C.E. (1988). Periodicity coding in the inferior colliculus of the cat. I. Neuronal mechanisms. Journal of Neurophysiology 60, 1799-1822.

Lin, J.Y., Lin, M.Z., Steinbach, P., and Tsien, R.Y. (2009). Characterization of engineered channelrhodopsin variants with improved properties and kinetics. Biophysical journal 96, 1803-1814.

Linden, R.M., and Berns, K.I. (2000). Molecular biology of adeno-associated viruses.

Lingner, A., Wiegrebe, L., and Grothe, B. (2012). Sound Localization in Noise by Gerbils and Humans. JARO: Journal of the Association for Research in Otolaryngology 13, 237-248.

Litovsky, R.Y., Colburn, H.S., Yost, W.A., and Guzman, S.J. (1999). The precedence effect. The Journal of the Acoustical Society of America 106, 1633-1654.

Litovsky, R.Y., McAlpine, D., Rees, A., and Palmer, A. (2010). Physiological correlates of the precedence effect and binaural masking level differences. The Oxford handbook of auditory science: The auditory brain 2, 333-357.

Magnusson, A.K., Park, T.J., Pecka, M., Grothe, B., and Koch, U. (2008). Retrograde GABA signaling adjusts sound localization by balancing excitation and inhibition in the brainstem. Neuron 59, 125-137.

Maier, J.K., Hehrmann, P., Harper, N.S., Klump, G.M., Pressnitzer, D., and McAlpine, D. (2012). Adaptive coding is constrained to midline locations in a spatial listening task. Journal of Neurophysiology 108, 1856-1868.

Maki, K., and Furukawa, S. (2005). Acoustical cues for sound localization by the Mongolian gerbil, Meriones unguiculatus. The Journal of the Acoustical Society of America 118, 872-886.

Mallet, N., Le Moine, C., Charpier, S., and Gonon, F. (2005). Feedforward inhibition of projection neurons by fast-spiking GABA interneurons in the rat striatum in vivo. The Journal of neuroscience 25, 3857-3869.

Masamizu, Y., Okada, T., Kawasaki, K., Ishibashi, H., Yuasa, S., Takeda, S., Hasegawa, I., and Nakahara, K. (2011a). Local and retrograde gene transfer into primate neuronal pathways via adeno-associated virus serotype 8 and 9. Neuroscience 193, 249-258.

Masamizu, Y., Okada, T., Kawasaki, K., Ishibashi, H., Yuasa, S., Takeda, S., Hasegawa, I., and Nakahara, K. (2011b). Local and retrograde gene transfer into primate neuronal pathways via adeno-associated virus serotype 8 and 9. Neuroscience 193, 249-258.

McAlpine, D., Jiang, D., and Palmer, A.R. (2001). A neural code for low-frequency sound localization in mammals. Nature neuroscience 4, 396-401.

McCarty, D.M. (2008). Self-complementary AAV Vectors; Advances and Applications. Molecular therapy : the journal of the American Society of Gene Therapy 16, 1648-1656.

McFadden, D., and Pasanen, E.G. (1976). Lateralization at high frequencies based on interaural time differences. The Journal of the Acoustical Society of America 59, 634-639.

McFarland, N.R., Lee, J.-S., Hyman, B.T., and McLean, P.J. (2009). Comparison of transduction efficiency of recombinant AAV serotypes 1, 2, 5, and 8 in the rat nigrostriatal system. Journal of Neurochemistry 109, 838-845.

Meffin, H., and Grothe, B. (2009). Selective filtering to spurious localization cues in the mammalian auditory brainstem. The Journal of the Acoustical Society of America 126, 2437-2454.

Mills, A.W. (1960). Lateralization of High-Frequency Tones. The Journal of the Acoustical Society of America 32, 132-134.

Mills, J.H., Schmiedt, R.A., and Kulish, L.F. (1990). Age-related changes in auditory potentials of mongolian gerbil. Hearing research 46, 201-210.

Moore, M.J., and Caspary, D.M. (1983). Strychnine blocks binaural inhibition in lateral superior olivary neurons. The Journal of neuroscience : the official journal of the Society for Neuroscience 3, 237-242.

Moser, T., Neef, A., and Khimich, D. (2006). Mechanisms underlying the temporal precision of sound coding at the inner hair cell ribbon synapse. The Journal of Physiology 576, 55-62.

Myoga, M.H., Lehnert, S., Leibold, C., Felmy, F., and Grothe, B. (2014). Glycinergic inhibition tunes coincidence detection in the auditory brainstem. Nature communications 5, 3790.

Nagel, G., Brauner, M., Liewald, J.F., Adeishvili, N., Bamberg, E., and Gottschalk, A. (2005). Light Activation of Channelrhodopsin-2 in Excitable Cells of Caenorhabditis elegans Triggers Rapid Behavioral Responses. Current Biology 15, 2279-2284.

Nagel, G., Ollig, D., Fuhrmann, M., Kateriya, S., Musti, A.M., Bamberg, E., and Hegemann, P. (2002). Channelrhodopsin-1: a light-gated proton channel in green algae. Science 296, 2395-2398.

Nagel, G., Szellas, T., Huhn, W., Kateriya, S., Adeishvili, N., Berthold, P., Ollig, D., Hegemann, P., and Bamberg, E. (2003). Channelrhodopsin-2, a directly light-gated cation-selective membrane channel. Proceedings of the National Academy of Sciences 100, 13940-13945.

Nathanson, J.L., Yanagawa, Y., Obata, K., and Callaway, E.M. (2009). Preferential labeling of inhibitory and excitatory cortical neurons by endogenous tropism of adeno-associated virus and lentivirus vectors. Neuroscience 161, 441-450.

Nonnenmacher, M., and Weber, T. (2012). Intracellular transport of recombinant adeno-associated virus vectors. Gene therapy 19, 649-658.

Oesterhelt, D., and Stoeckenius, W. (1971). Rhodopsin-like protein from the purple membrane of Halobacterium halobium. Nature 233, 149-152.

Oliver, D., and Shneiderman, A. (1989). An EM study of the dorsal nucleus of the lateral lemniscus: inhibitory, commissural, synaptic connections between ascending auditory pathways. The Journal of Neuroscience 9, 967-982.

Oliver, D.L., and Morest, D.K. (1984). The central nucleus of the inferior colliculus in the cat. Journal of Comparative Neurology 222, 237-264.

Otchy, T.M., Wolff, S.B.E., Rhee, J.Y., Pehlevan, C., Kawai, R., Kempf, A., Gobes, S.M.H., and Ölveczky, B.P. (2015). Acute off-target effects of neural circuit manipulations. Nature 528, 358-363.

Palmer, A.R., and Russell, I.J. (1986). Phase-locking in the cochlear nerve of the guinea-pig and its relation to the receptor potential of inner hair-cells. Hearing research 24, 1-15.

Park, T.J., Monsivais, P., and Pollak, G.D. (1997). Processing of Interaural Intensity Differences in the LSO: Role of Interaural Threshold Differences. Journal of Neurophysiology 77, 2863-2878.

Paterna, J., Moccetti, T., Mura, A., Feldon, J., and Büeler, H. (2000). Influence of promoter and WHV post-transcriptional regulatory element on AAV-mediated transgene expression in the rat brain. Gene therapy 7, 1304-1311.

Pecka, M., Brand, A., Behrend, O., and Grothe, B. (2008). Interaural time difference processing in the mammalian medial superior olive: the role of glycinergic inhibition. The Journal of neuroscience : the official journal of the Society for Neuroscience 28, 6914-6925.

Pecka, M., Siveke, I., Grothe, B., and Lesica, N.A. (2010). Enhancement of ITD Coding Within the Initial Stages of the Auditory Pathway. Journal of Neurophysiology 103, 38-46.

Pecka, M., Zahn, T.P., Saunier-Rebori, B., Siveke, I., Felmy, F., Wiegrebe, L., Klug, A., Pollak, G.D., and Grothe, B. (2007). Inhibiting the inhibition: a neuronal network for sound localization in reverberant environments. The Journal of neuroscience : the official journal of the Society for Neuroscience 27, 1782-1790.

Pettei, M.J., Yudd, A.P., Nakanishi, K., Henselman, R., and Stoeckenius, W. (1977). Identification of retinal isomers isolated from bacteriorhodopsin. Biochemistry 16, 1955-1959.

Phillips, D.P., and Hall, S.E. (2005). Psychophysical evidence for adaptation of central auditory processors for interaural differences in time and level. Hearing research 202, 188-199.

Pollak, G.D., Burger, R.M., and Klug, A. (2003). Dissecting the circuitry of the auditory system. Trends in Neurosciences 26, 33-39.

Porres, C.P., Meyer, E.M., Grothe, B., and Felmy, F. (2011). NMDA currents modulate the synaptic input-output functions of neurons in the dorsal nucleus of the lateral lemniscus in Mongolian gerbils. The Journal of neuroscience : the official journal of the Society for Neuroscience 31, 4511-4523.

Qing, K., Mah, C., Hansen, J., Zhou, S., Dwarki, V., and Srivastava, A. (1999). Human fibroblast growth factor receptor 1 is a co-receptor for infection by adeno-associated virus 2. Nature medicine 5, 71-77.

Raes, A., Van de Vijver, G., Goethals, M., and van Bogaert, P.P. (1998). Use-dependent block of I(h) in mouse dorsal root ganglion neurons by sinus node inhibitors. British Journal of Pharmacology 125, 741-750.

Raimondo, J.V., Kay, L., Ellender, T.J., and Akerman, C.J. (2012). Optogenetic silencing strategies differ in their effects on inhibitory synaptic transmission. Nat Neurosci 15, 1102-1104.

Rayleigh, L. (1907). XII. On our perception of sound direction. The London, Edinburgh, and Dublin Philosophical Magazine and Journal of Science 13, 214-232.

Roberts, M.T., Seeman, S.C., and Golding, N.L. (2013). A mechanistic understanding of the role of feedforward inhibition in the mammalian sound localization circuitry. Neuron 78, 923-935.

Robinson, D.W., and Dadson, R.S. (1956). A re-determination of the equal-loudness relations for pure tones. British Journal of Applied Physics 7, 166.

Ryan, A. (1976). Hearing sensitivity of the mongolian gerbil, Merionesunguiculatis. The Journal of the Acoustical Society of America 59, 1222-1226.

Sabin, A.T., Macpherson, E.A., and Middlebrooks, J.C. (2005). Human sound localization at near-threshold levels. Hearing research 199, 124-134.

Sabine, W.C. (1922). Collected papers on acoustics (Harvard university press).

Salo, A.L., and French, J.A. (1989). Early experience, reproductive success, and development of parental behaviour in Mongolian gerbils. Animal behaviour 38, 693-702.

Schuller, G., Radtke-Schuller, S., and Betz, M. (1986). A stereotaxic method for small animals using experimentally determined reference profiles. Journal of Neuroscience Methods 18, 339-350.

Seidl, A.H., and Grothe, B. (2005). Development of Sound Localization Mechanisms in the Mongolian Gerbil Is Shaped by Early Acoustic Experience. Journal of Neurophysiology 94, 1028-1036.

Shinn-Cunningham, B.G., Kopco, N., and Martin, T.J. (2005). Localizing nearby sound sources in a classroom: Binaural room impulse responses. The Journal of the Acoustical Society of America 117, 3100-3115.

Shinn-Cunningham, B.G., Santarelli, S., and Kopco, N. (2000). Tori of confusion: binaural localization cues for sources within reach of a listener. The Journal of the Acoustical Society of America 107, 1627-1636.

Shneiderman, A., Oliver, D.L., and Henkel, C.K. (1988). Connections of the dorsal nucleus of the lateral lemniscus: an inhibitory parallel pathway in the ascending auditory system? Journal of Comparative Neurology 276, 188-208.

Sivaramakrishnan, S., and Oliver, D.L. (2001). Distinct K currents result in physiologically distinct cell types in the inferior colliculus of the rat. The Journal of Neuroscience 21, 2861-2877.

Siveke, I., Pecka, M., Seidl, A.H., Baudoux, S., and Grothe, B. (2006). Binaural Response Properties of Low-Frequency Neurons in the Gerbil Dorsal Nucleus of the Lateral Lemniscus. Journal of Neurophysiology 96, 1425-1440.

Spirou, G.A., Rager, J., and Manis, P.B. (2005). Convergence of auditory-nerve fibre projections onto globular bushy cells. Neuroscience 136, 843-863.

Stange, A., Myoga, M.H., Lingner, A., Ford, M.C., Alexandrova, O., Felmy, F., Pecka, M., Siveke, I., and Grothe, B. (2013). Adaptation in sound localization: from GABAB receptor-mediated synaptic modulation to perception. Nat Neurosci 16, 1840-1847.

Sterbing, S.J., Hartung, K., and Hoffmann, K.P. (2002). Representation of sound source direction in the superior colliculus of the guinea pig in a virtual auditory environment. Experimental brain research 142, 570-577.

Stinson, M.R., and Lawton, B. (1989). Specification of the geometry of the human ear canal for the prediction of sound-pressure level distribution. The Journal of the Acoustical Society of America 85, 2492-2503.

Summerford, C., Bartlett, J.S., and Samulski, R.J. (1999). αVβ5 integrin: a co-receptor for adeno-associated virus type 2 infection. Nature medicine 5, 78-82.

Summerford, C., and Samulski, R.J. (1998). Membrane-associated heparan sulfate proteoglycan is a receptor for adeno-associated virus type 2 virions. Journal of virology 72, 1438-1445.

Suzuki, Y., and Takeshima, H. (2004). Equal-loudness-level contours for pure tones. The Journal of the Acoustical Society of America 116, 918-933.

Taymans, J.-M., Vandenberghe, L.H., Haute, C.V.D., Thiry, I., Deroose, C.M., Mortelmans, L., Wilson, J.M., Debyser, Z., and Baekelandt, V. (2007). Comparative Analysis of Adeno-Associated Viral Vector Serotypes 1, 2, 5, 7, And 8 in Mouse Brain. Human gene therapy 18, 195-206.

Thompson, S.P. (1882). Ll. On the function of the two ears in the perception of space. Philosophical Magazine Series 5 13, 406-416.

Tollin, D.J. (2003). The lateral superior olive: a functional role in sound source localization. The Neuroscientist : a review journal bringing neurobiology, neurology and psychiatry 9, 127-143.

Tollin, D.J., and Yin, T.C. (2002). The coding of spatial location by single units in the lateral superior olive of the cat. I. Spatial receptive fields in azimuth. The Journal of neuroscience : the official journal of the Society for Neuroscience 22, 1454-1467.

van der Heijden, M., and Trahiotis, C. (1999). Masking with interaurally delayed stimuli: The use of "internal" delays in binaural detection. The Journal of the Acoustical Society of America 105, 388-399.

Vo-Dinh, T. (2014). Biomedical Photonics Handbook: Biomedical Diagnostics, Vol 2 (CRC press).

Von Békésy, G., and Wever, E.G. (1960). Experiments in hearing, Vol 8 (McGraw-Hill New York).

Wallach, H., Newman, E.B., and Rosenzweig, M.R. (1949). The Precedence Effect in Sound Localization. The American Journal of Psychology 62, 315-336.

Wiener, F.M., and Ross, D.A. (1946). The Pressure Distribution in the Auditory Canal in a Progressive Sound Field. The Journal of the Acoustical Society of America 18, 401-408.

Wietek, J., Wiegert, J.S., Adeishvili, N., Schneider, F., Watanabe, H., Tsunoda, S.P., Vogt, A., Elstner, M., Oertner, T.G., and Hegemann, P. (2014). Conversion of channelrhodopsin into a light-gated chloride channel. Science 344, 409-412.

Bibliography

Wightman, F.L., and Kistler, D.J. (1992). The dominant role of low-frequency interaural time differences in sound localization. The Journal of the Acoustical Society of America 91, 1648-1661.

Wu, Z., Yang, H., and Colosi, P. (2009). Effect of Genome Size on AAV Vector Packaging. Molecular therapy : the journal of the American Society of Gene Therapy 18, 80-86.

Xu-Friedman, M.A., and Regehr, W.G. (2005). Dynamic-clamp analysis of the effects of convergence on spike timing. I. Many synaptic inputs. Journal of neurophysiology 94, 2512-2525.

Yang, L., and Pollak, G.D. (1994). The roles of GABAergic and glycinergic inhibition on binaural processing in the dorsal nucleus of the lateral lemniscus of the mustache bat. Journal of neurophysiology 71, 1999-2013.

Yizhar, O., Fenno, Lief E., Davidson, Thomas J., Mogri, M., and Deisseroth, K. Optogenetics in Neural Systems. Neuron 71, 9-34.

Yizhar, O., Fenno, L.E., Prigge, M., Schneider, F., Davidson, T.J., O/'Shea, D.J., Sohal, V.S., Goshen, I., Finkelstein, J., Paz, J.T*., et al.* (2011). Neocortical excitation/inhibition balance in information processing and social dysfunction. Nature 477, 171-178.

Yost, W.A., and Dye, R.H., Jr. (1988). Discrimination of interaural differences of level as a function of frequency. The Journal of the Acoustical Society of America 83, 1846-1851.

Yost, W.A., and Hafter, E.R. (1987). Lateralization. In Directional hearing (Springer), pp. 49-84.

Yost, W.A., Wightman, F.L., and Green, D.M. (1971). Lateralization of filtered clicks. The Journal of the Acoustical Society of America 50, 1526-1531.

Young, E.D., Rice, J.J., and Tong, S.C. (1996). Effects of pinna position on head-related transfer functions in the cat. The Journal of the Acoustical Society of America 99, 3064-3076.

Zhang, F., Gradinaru, V., Adamantidis, A.R., Durand, R., Airan, R.D., de Lecea, L., and Deisseroth, K. (2010). Optogenetic interrogation of neural circuits: technology for probing mammalian brain structures. Nature protocols 5, 439-456.

Zhang, F., Wang, L.P., Boyden, E.S., and Deisseroth, K. (2006). Channelrhodopsin-2 and optical control of excitable cells. Nature methods 3, 785-792.

Zhang, F., Wang, L.P., Brauner, M., Liewald, J.F., Kay, K., Watzke, N., Wood, P.G., Bamberg, E., Nagel, G., Gottschalk, A., and Deisseroth, K. (2007). Multimodal fast optical interrogation of neural circuitry. Nature 446, 633-639.

Zhang, P.X.H., William M, and Hartmann, W.M. (2006). Lateralization of sine tones-interaural time vs phase. Journal of the Acoustical Society of America 120, 3471-3474.

Zheng, H., Qiao, C., Wang, C.-H., Li, J., Li, J., Yuan, Z., Zhang, C., and Xiao, X. (2009). Efficient Retrograde Transport of Adeno-Associated Virus Type 8 to Spinal Cord and Dorsal Root Ganglion After Vector Delivery in Muscle. Human gene therapy 21, 87-97.

Zincarelli, C., Soltys, S., Rengo, G., and Rabinowitz, J.E. (2008). Analysis of AAV serotypes 1–9 mediated gene expression and tropism in mice after systemic injection. Molecular Therapy 16, 1073-1080.

Zurek, P.M. (1980). The precedence effect and its possible role in the avoidance of interaural ambiguities. The Journal of the Acoustical Society of America 67, 952-964.

Acknowledgements

Eidesstattliche Erklärung

Ich versichere hiermit an Eides statt, dass die vorgelegte Dissertation von mir selbständig und ohne unerlaubte Hilfe angefertigt ist. Die vorliegende Dissertation wurde weder ganz, noch teilweise bei einer anderen Prüfungskommission vorgelegt. Ich habe noch zu keinem früheren Zeitpunkt versucht, eine Dissertation einzureichen oder an einer Doktorprüfung teilzunehmen.

München, den 17.02.2016 ....

(Stefan Keplinger)